Title
Molecular Modeling of Cardiac Proteins and Their Interactions with Beta Blockers

Author
Dawson, John Randolph Dillon

Publication Date
2022

Peer reviewed|Thesis/dissertation

Molecular Modeling of Cardiac Proteins and Their Interactions with Beta Blockers

By

JOHN RANDOLPH DILLON DAWSON
DISSERTATION

Submitted in partial satisfaction of the requirements for the degree of

DOCTOR OF PHILOSOPHY

in

Biophysics

in the

OFFICE OF GRADUATE STUDIES

of the

UNIVERSITY OF CALIFORNIA

DAVIS

Approved:

Igor Vorobyov, Chair

Vladimir Yarov-Yarovoy

Colleen E. Clancy

Committee in Charge

2022

Table of Contents

List of Figures

List of Tables

List of Abbreviations

βAR .....beta adrenergic receptor

BCL .....basic cycle length

CHARMM .....chemistry at Harvard macromolecular mechanics

CiPA ..... comprehensive in vitro proarrhythmia assay

CryoEM .....cryogenic electron microscopy

EAD ..... early afterdepolarization

ECG .....electrocardiogram

ECL2 .....extracellular loop two

EPI .....epinephrine

Gs.....stimulatory G-protein

$G_s\alpha$..... alpha subunit of the stimulatory G-protein

HREUS-MD .....Hamiltonian replica exchange umbrella sampling molecular dynamics

HEK ..... human embryonic kidney

hERG ..... human *Ether-à-go-go*-related gene

HPLC .....high performance liquid chromatography

IC_{50} ..... the half maximal inhibitory concentration

ICL3 ..... intracellular loop three

IE ..... interface energy

ISO ..... isoproterenol

K^+ ..... potassium cation

K_V ..... voltage-gated potassium channel

MD ..... molecular dynamics

NAMD ..... nanoscale molecular dynamics

NE ..... norepinephrine

NMR ..... nuclear magnetic resonance

PNS ..... parasympathetic nervous system

PD ..... pore domain

PDB ..... protein data bank

PKA ..... protein kinase A

POPC 1-palmitoyl-2-oleoylphosphatidylcholine

POPS 1-palmitoyl-oleoyl-phosphatidylserine

REU ..... Rosetta energy units

RMSD ..... root-mean-square deviation

SEM ..... standard error of means

SF ..... selectivity filter

SNS ..... sympathetic nervous system

TdP ..... torsades de pointes

US-MD ..... umbrella sampling molecular dynamics

VMD ..... visual molecular dynamics

VSD ..... voltage sensing domain

WT ..... wild-type

Acknowledgments

I am indebted to my PI Igor Vorobyov for accepting me as his first graduate student into his lab, which now grows exponentially in vibrancy and number; for his earnest counsel during my most challenging times, and for his unwavering support despite them. I express gratitude for Vladimir Yarov-Yarovoy, who has been an inspirational educator and a bedrock of guidance since we first met in Spring of 2017. I thank Colleen Clancy for her advocacy and her no-nonsense professionalism. I pray that I may one day exude competence as she. Thank you, Kevin DeMarco for your tutelage, friendship, and for the pure life. I would have undoubtedly not survived graduate school without your daily presence, let alone expertise. I extend the same appreciation to Gonzalo Hernandez-Hernandez: no word is sufficient to convey the impact of your companionship these past five years. Thank you, family: Mom & Dana, for the blood, sweat, and tears; Nick, for your relentless support; Karlee, for setting me on this path and keeping me to it; Andrew, for your loving ear and our common struggle; Dad, for your faith and admiration; Mingming, for your persistence and sacrifice; and my cadre of timeless family friends who have seen me through. Our love is infinite. Lastly, thank you Baba for showing me what matters most -- this is for you. Memory Eternal!

Funding Sources

We would like to acknowledge to following sources of funding and computational resources: National Institutes of Health (NIH) Common Fund SPARC grant OT2OD026580 (Colleen E. Clancy & Igor Vorobyov), NIH NHLBI grants R01HL128537 (Colleen E. Clancy, Igor Vorobyov, Vladimir Yarov-Yarovoy), R01HL152681 (Colleen E. Clancy & Igor Vorobyov) and U01HL126273 (Colleen E. Clancy & Vladimir Yarov-Yarovoy); UC Davis Pharmacology NIH T32GM099608 (John R. D. Dawson), ; American Heart Association (AHA) career development award 19CDA34770101 (Igor Vorobyov); UC Davis Department of Physiology and Membrane Research Partnership Fund (Colleen E. Clancy & Igor Vorobyov). Computational resources: UC Davis, Extreme Science and Engineering Discovery Environment (XSEDE) research allocation MCB170095 (Colleen E. Clancy & Igor Vorobyov & Kevin R. DeMarco), Oracle cloud for research credits award (Colleen E. Clancy & Igor Vorobyov), Texas Advanced Computing Center (TACC) Leadership Resource and Pathways Allocation MCB20010 (Igor Vorobyov & Colleen E. Clancy), National Center for Supercomputing Applications (NCSA) Blue Waters Broadening Participation Allocation (Colleen E. Clancy & Igor Vorobyov & Kevin R. DeMarco), Pittsburgh Supercomputing Center (PSC) Anton 2 allocations MCB160089P, PSCA18077P, PSCA17085P, PSCA16108P (Igor Vorobyov & Colleen E. Clancy & Kevin R. DeMarco). Anton 2 computer time was provided by the PSC through Grant R01GM116961 from the National Institutes of Health. The Anton 2 machine at PSC was generously made available by D.E. Shaw Research.

Abstract

Cardiotoxicity risks in the form cardiac arrhythmias prevent new drug candidates to advance from pre-clinical development. One measure of this risk is the prolongation of the QT interval on the electrocardiogram (ECG) - a surrogate marker for abnormal electrical activity and a potential precursor for fatal ventricular arrhythmias. A number of high-profile drug failures due to their cardiotoxicity have been attributed to drug interactions with the voltage-gated potassium channel Kv11.1, also known as the human Ether-a-go-go Related Gene Encoded Protein (or "hERG"), a cardiac ion transport protein largely responsible for the repolarization of the cardiac action potential and thus QT interval duration. Drugs from multiple classes block hERG channel and can cause QT interval prolongation and possibly arrhythmias. In this work we will focus on beta-blockers, which are used to treat cardiovascular disorders including some arrhythmias but inadvertently can be arrhythmogenic as well. One such drug molecule is d-sotalol, the dextrorotary stereoisomer of the beta-blocking anti-arrhythmic drug dl-sotalol, which proved to induce fatal arrhythmias due to hERG blockade in the "Survival with Oral D-Sotalol" clinical study. Sotalol is otherwise is formulated as a racemic beta blocker indicated for the treatment of arrhythmias like atrial fibrillation by blocking the activation of beta-adrenergic receptors, a target blocked only by the l-stereoisomer. Yet l-sotalol is as effective at blocking hERG as its dextrorotary counterpart. It seems that beta-blocking activity may attenuate arrhythmogenic risks posed by sotalol-induced QT prolongation, and experimental evidence supports this conclusion. However, the molecular mechanism that governs this selectivity on

the beta-adrenergic receptor remains unknown. Here we examine stereospecific interactions of the stereoisomers of sotalol with the beta-adrenergic receptor subtypes β_1 and β_2, but not before examining hERG conduction and the nature of hERG channel blockade by sotalol. In pursuing this line of inquiry, we find that the while molecular dynamics simulations can support experimental evidence regarding hERG-blockade, assessing beta-blockade in the orthosteric ligand binding pocket of the beta-receptors using molecular docking approach, as opposed to molecular dynamics, falls short of recapitulating this physiological phenomenon.

Chapter 1. Introduction

One of the most significant obstacles preventing new drugs from reaching the market is their potential to cause arrhythmia, which is a leading cause of drug termination during pre-clinical development[1, 2]. One measure for cardiotoxic arrhythmia risk is the prolongation of the QT interval on the ECG - a marker for abnormal electrical activity and a potential progenitor of fatal ventricular arrhythmias[3]. A number of high-profile drug failures due to their cardiotoxicity have been attributed to promiscuous drug interactions with the voltage-gated potassium channel Kv11.1, also known as the human Ether-a-go-go Related Gene Encoded Protein (or "hERG"), a cardiac ion transport protein primarily responsible for the repolarization of the cardiac action potential and thus QT interval duration[3, 4]. hERG blockade and QT prolongation serve as surrogate markers of pro-arrhythmia risk and are used by the FDA for assessing drug safety[5]. However, these criteria alone do not adequately differentiate safe from unsafe drugs, as there are multiple examples of cardiac-safe drugs on the market that fail those tests[6, 7].

In this work we focused on beta-blockers, drugs, which are commonly used treat anxiety, hypertension, congestive heart failure, arrhythmias, and other cardiovascular and neurological disorders[8-10]. Yet, many of them are known to block hERG channel, with some leading to arrhythmia risks but others being cardiac-safe at clinical doses[6, 11-13]. There is currently no established way to distinguish safe and unsafe hERG blockers from their chemical structures, while there are numerous efforts to do so through coordinated efforts by academia, industry, and regulatory agencies such as e.g., Comprehensive in vitro Pro-arrhythmia Assay (CiPA) initiative[14].

We have recently developed a multiscale modeling pipeline that successfully distinguished between safe and unsafe hERG blockers *in silico* by simulating state-specific hERG channel – drug interactions at the atomistic scale and using computed rates and affinities as parameters for functional models, which subsequently predicted emergent pro-arrhythmia markers at the cell and tissue scale[15, 16]. However, this framework does not account for possible drug interactions with other protein targets that may affect cardiac electrical activity and influence drug cardiotoxicities.

As a first step in including these multi-target effects, we propose studying the drug interactions with beta adrenergic receptors (βAR), since many beta blockers have hERG-blocking activity but divergent cardiac safety profiles: for instance, carvedilol blocks hERG at clinically relevant concentrations, while propranolol can induce long QT when overdosed[12]. In fact, carvedilol's off-target hERG block may account for its superior performance over the cardioselective beta blocker metoprolol in preventing sudden cardiac death in the COMET Trial (Carvedilol Or Metoprolol European Trial[12, 13]. Perhaps most consequential of the hERG-blocking beta blockers is sotalol, or dl-sotalol.

Sotalol is a racemic drug with stereospecific beta-adrenergic blockade, but likely non-stereospecific hERG blockade: d-sotalol can block hERG currents yet cannot competitively antagonize beta adrenergic receptors at clinical concentrations, whereas l-sotalol can block both[6, 11]. This distinction proved tragic when the "Survival with Oral D-sotalol" (SWORD) clinical trial terminated early upon finding that mortality for patients taking d-sotalol

doubled on over placebo[4, 17, 18]. Alone, d-sotalol is highly arrhythmogenic, and yet racemic dl-sotalol remains a marketed drug with better cardiac safety profile[11]. At the same time, the prescribed beta-blocker propranolol has been shown to block hERG channel at clinically relevant concentrations, yet it is also regarded as cardiac-safe[19-21].While a functional model may simulate the electrophysiological consequences of estimated net affinities for drug blockade of either target, a multi-scale model using MD simulations to quantify multiple protein target – drug interactions should recapitulate protein conformational state specificities at the atomistic scale and thus can be used to develop safer pharmaceuticals.

Understanding the diverse target specificities exhibited by beta-blockers is particularly vital when modeling disease conditions for the role of beta-adrenergic receptors changes dramatically. During disease, sympathetic activity can affect cardiac nerve remodeling, induce hypertrophy, and cause fibrosis[22]. During heart failure (HF), for example, adrenergic stimulation significantly increases to compensate for lost cardiac output[23]. Additional stimulation counteracts reduced inotropy, and beta agonists may be prescribed to enhance cardiac output further. However, this increases energy expenditure, stressing the heart and encouraging a host of genetic changes that worsen the condition[24]. Excessive adrenergic stimulation may also lead to hyper-innervation in some instances, and hypo-innervation in others; both scenarios may induce ectopic activity, exacerbating arrhythmia risk[22]. At the cellular level, heart failure leads to a downregulation of β_1AR by approximately 60% and an upregulation of β_2AR by 40% from basal expression levels; while β_1AR outnumbers β_2AR by four to one in normal conditions, HF shifts this ratio towards two

to one[22, 25]. Thus, discerning the interactions favored by different beta blockers with different subtypes of adrenergic receptors and their different conformational states has utility for functional models replicating adrenergic stimulation in health and disease. Understanding which drugs favor specific beta-receptor conformational states and their G protein complexes at the atomistic scale is a vital first step towards anticipating their effect during disease progression.

This work will discuss how we came to determine that the hERG model published in Yang etal[16] was in the open state and the structural protein properties affecting ion conduction using all-atom molecular dynamics simulations. Then it will discuss our recent contributions to understanding dl-sotalol interactions with hERG potassium channel as can be assessed using atomistic molecular dynamics simulations in our published work [15]. Lastly, it will discuss the development of models of beta-adrenergic receptors β_1AR and β_2AR in multiple conformational states, with and without bound stimulatory G protein. Having docked endogenous ligand norepinephrine and stereoisomeric beta blockers sotalol and propranolol to these receptor models, we assess the capability for molecular docking to attest to the known stereospecific selectivity against βARs that may contribute to their differential cardiotoxic effects and will also allow us to test alternative hypotheses.

Chapter 2. Characterizing the Conducting State of the Cardiac Potassium Channel $K_v11.1$

Acknowledgments:

The development of a model of the wild-type cardiac potassium channel hERG, its S641A mutant and their molecular dynamics simulation setup were performed by Dr. Kevin DeMarco and published in part in Yang et al "A Computational Pipeline to Predict Cardiotoxicity. Circulation Research. 2020;126(8):947-64.".

2.1 Introduction

Many high-profile drug failures due to cardiotoxicity have been attributed to promiscuous drug interactions with the voltage-gated potassium channel Kv11.1, also known as the human *Ether-a-go-go Related Gene* (or hERG) channel [26, 27]. The hERG channel is responsible for the delayed rectifying K^+ current of cardiomyocytes known as I_{Kr} and contributes to repolarization phase of the cardiac action potential and thus the QT interval duration of the electrocardiogram (QT), a surface level reading of cardiac electrical activity corresponding to ventricular contraction and relaxation [27]. hERG blockade and subsequent QT prolongation serve as surrogate markers of pro-arrhythmia risk and are used by the FDA for assessing drug safety[5], but have been found not selective to provide accurate predictions. There are multiple drugs, which block hERG channel and prolong QT interval, but are cardiac-safe: for instance, carvedilol blocks hERG at clinically relevant concentrations, while propranolol can induce long QT when overdosed[12]. In fact, carvedilol's off-target hERG block may account for its superior performance over the

cardioselective beta blocker metoprolol in preventing sudden cardiac death in the COMET Trial (Carvedilol Or Metoprolol European Trial)([12, 13]. This can lead to withdrawal of safe and efficacious medications[14]. Consequently, elucidating the molecular determinants of drug - hERG interactions is highly desirable.

Central to the contribution by hERG channel in cardiac repolarization are the channel's distinct kinetic properties. The hERG channel is an inward rectifier that transitions from a closed state to an open state upon membrane depolarization, but then undergoes rapid inactivation: a state in which the channel is unable to conduct potassium ions despite the pore domain remaining open and voltage sensing domains activated [28, 29]. Though many channels possess inactivated states, the rapidity of this transition is essential to its function for inactivation reduces I_{kr} to govern cardiac action potential duration [28, 29]. Consequently, hERG blocking drugs that pose pro-arrhythmic risk preferentially bind and hold the channel in the inactivated state, attenuating I_{kr} to ultimately prolong the QT interval [30, 31]. However, the potentially life-threatening consequences of drug-induced Long QT-Syndrome are not easily anticipated without widescale clinical testing in humans, and many drugs have notoriously escaped scrutiny. Furthermore, the criterion of hERG blockade as a predictor for arrhythmia risk does not necessarily capture this pernicious state-specificity. Therefore, the molecular modeling community has sought an atomistic-scale understanding of hERG channel structure, kinetics, and state-specific drug interactions since the early 2000s building its structural models using homologous channel structures (see Durdagi et al., 2012[32]). However, the publishing of the cryo-EM structure of the channel by Wang et al[26]. (ref) has been insightful for structural biologists and crucial for molecular modelers.

Recently we contributed to a multi-scale computer modeling pipeline for predicting drug-induced arrhythmia from drug chemistry starting from atomic-level interactions of drugs with hERG channel to assess their different pro-arrhythmia outcomes[16]. Using the umbrella sampling molecular dynamics methodology to determine the potentials of mean force and diffusion coefficient profiles for drug-pore access, we computed free energies of binding, dissociation constants, K_d, and diffusion coefficients in the channel pore for the hERG blockers moxifloxacin and dofetilide in different ionization states. These data were used to calculate "on" and "off" rates, k_{on} andk_{off}. These values, after being shown to agree with equivalent experimental values where applicable (such as e.g., computed K_d and experimental IC_{50} comparison) , were in turn used to parameterize functional kinetic Markov state models for ion-channel gating that simulated time and state-dependent channel-drug interactions for either drug, considering fractions of ionized and neutral drug states at the physiological pH. When integrated into well-established cell and tissue scale functional models of cardiac action potential propagation, these MD-derived channel – drug interaction kinetic parameters recapitulated these drugs' divergent risk profiles for induced arrhythmia vulnerability as measured by by action potential durations, beat-to-beat variabilities, action potential triangulation as well as appearance of electric potential abnormalities such as early afterdepolarizations[16].

hERG is a homotetrameric voltage-gated potassium channel composed of six transmembrane helices denoted S1 through S6. Transmembrane segments S1-S4 comprise the voltage-sensing domain (VSD), while S5-S6 comprise the pore domain (PD). The VSD and

the PD associate in a non-domain swapped manner, meaning the VSD is adjacent to a PD segment of the same protein chain when forming the homotetrameric protein[33]. The VSDs reside within the lipid bilayer, waiting to undergo a conformational change in response to changes in local transmembrane electrical potential, thus conveying voltage sensitivity to channel gating. This voltage sensitivity is mediated by five positively charged amino acids located on the S4 helix: K1, R2, R3, R4, and R5. However, only K1, R2, and R3, which are located towards the extracellular side of the VSD, participate in channel gating [34]. A helical-screw model may be used to describe activation of a VSD helical screw mechanism: when the transmembrane electrical potential about the VSD changes, the S4 helix slides the length of a few turns, about 7 Å, along the S1, S2, and S3 segments, whilst rotating 30° and pivoting about a hydrophobic core. This transition is coupled to a lateral movement of the S4-S5 linker, which is hypothesized to induce a rearrangement of the PD helices S5 and S6 to result in channel opening. For this to occur, all four VSDs need to be activated[35-37].

Ion conduction occurs through the selectivity filter (SF), an interface of four demi-helical structures formed by a part of a sequence between S5 and S6 of the pore domain. The selectivity filter conveys 100-fold selectivity for permeating potassium over sodium ions, thus enabling the coordinated flux of potassium ions and water through the channel[26]. The potassium selectivity is achieved through the tight K^+ coordination by backbone carbonyl groups of the SF residues to provide its optimal solvation, while also permitting multiple ions to occupy the SF simultaneously at ordered positions called occupancy sites[26]. This chemical mechanism, which is conserved across many potassium channels, was first determined in the crystal structure of the pH-gated bacterial potassium channel KcsA[38].

To achieve sufficient fidelity in this intricate protocol, it is fundamental that the models are physiologically relevant. When modeling state-dependent drug block, this means ensuring published protein models are in the conformational state they are declared to occupy. Molecular dynamics enables validating ion channel states by challenging model to a simulated voltage[39]. By simulating the recent hERG ion channel structural model under voltage, we can elucidate the state of the channel and identify atomic-level mechanisms it uses to conduct K^+ ions.

We used a putative open-state model of hERG channel that was developed using the cryoEM structure of hERG (PDB ID: 5VA2[26] and Rosetta computational modeling [40-42] and later published in Yang et al[16]. We applied all-atom molecular dynamics (MD) simulations to characterize the hERG channel model stability and ion conduction at multi-microsecond timescales to access structural determinants of ion conduction and channel inactivation. MD simulations of the wild-type hERG with applied 750mV in 0.15M KCl resulted in several K^+ ion conduction events that preceded substantial selectivity filter (SF) distortions and pore closure. These results were validated through simulations of $K_V1.2/2.1$ Paddle Chimera channel (PDB ID: 2R9R[43]) under identical conditions, which yielded multiple fast K^+ permeation events along with an initially more stable SF. The same conditions yielded no conduction when applied to a model of the fast-inactivating S641A hERG mutant.

2.2 Methods

2.2.1. General MD simulation setup

The CHARMM-GUI online toolkit[44], CHARMM[45, 46], NAMD[47], and Anton 2 software programs were used in order to build and simulate the molecular systems. Each system contained a 1-palmitoyl-2-oleoylphosphatidylcholine (POPC) lipid bilayer hydrated by a 0.15 M aqueous KCl solution. The membrane normal axis was aligned along the *z*-axis in all cases. Either the hERG or K_v1.2/2.1 channel were placed in the bilayer center with its aqueous pore aligned with the membrane normal. For the S641A mutant, CHARMM-GUI was used to add the mutation. All NAMD simulations apart from ion conduction simulations under applied voltage, were carried out in an *NPT* ensemble with 1 atm pressure maintained by Langevin piston barostat[48], and 310K, controlled by Nosé-Hoover thermostat[49, 50]. MD simulations with an applied voltage to study ion conduction were carried out in the *NVT* ensemble. Tetragonal cells with periodic boundary conditions (PBC) were used in all the simulations, and the SHAKE algorithm[51] was employed to fix the bonds to all hydrogen atoms, allowing for the use of a 2 fs time step. Electrostatic interactions were computed via Particle Mesh Ewald[52], with a mesh grid of 1 Å.

2.2.2. Refinement of cryo-EM hERG structure

The 3D coordinates of hERG channel structure (PDB ID: 5VA2) obtained via cryogenic electron microscopy (cryo-EM) were used as a template[26]. This structure has several unresolved extracellular loop regions: residues 434-451 (between helices S1 and S2), 512-519 (between helices S3 and S4), and 578-582, 598-602 (in the pore loop region). The

template was truncated beyond S668 on the S6 helix, eliminating intracellular PAS and C-terminal domains, leaving only the voltage-sensing domain (VSD) and pore domain (PD) portions for our study (1,004 residues in total for the homotetramer). To model the missing loop regions, we used ROSETTA symmetry [53] and *de novo* loop modeling protocols[40, 41, 53]. In this process, 3- and 9-mer protein fragments from structures in the PDB were first obtained using the Robetta fragment server for the target hERG amino acid sequence[54]. A conformational search using those structural fragments was performed according to cyclic coordinate descent (CCD) and kinematic loop closure (KLC) algorithms[42, 55]. 20,000 initial poses were generated and the top 10% were filtered according to total energy score. This subset of poses were clustered[56] with a 2.0 Å root-mean-square deviation (RMSD) cutoff, and a low scoring structure (-984.884 Rosetta Energy Units (REU)) was selected from the most frequently sampled ensemble of models to undergo side chain relaxation[41, 57], in which protein backbone atoms are fixed while side chains are repacked using rotamer libraries. In this phase, simulated annealing followed by gradient minimization of the protein side chain torsional space was performed, and resultant poses were accepted or rejected based on the Metropolis criterion. 20,000 poses were again generated in this relaxation phase, the top 10% filtered and clustered, and from this subset a low scoring (-1961.173 REU or -1.95 REU/residue) structure was selected for use in the remainder of this study using Molecular Dynamics (MD) simulations. An initial structure of S641A hERG mutant for MD simulations was obtained using the wild-type channel model described above via side chain alteration of Ser 641 residues of four protein chains using UCSF Chimera.[58]

2.2.3. hERG Model equilibration and stability

The refined hERG model was embedded in a POPC lipid bilayer and solvated with a 150 mM aqueous KCl solution using CHARMM36 all-atom force fields[59-61] and TIP3P water model[62] using CHARMM-GUI web toolkit[44]. Assembled systems consisted of ~128,000 atoms and were simulated with NAMD 2.12[47] at a constant pressure of 1 atm and at a physiological temperature of 310 K. The systems were equilibrated for 90 ns using staged, extended equilibration methodology outlined in **Table 2.1** that we determined to be essential maintaining protein stability. After 90 ns initial equilibration, which is a typical simulation time necessary to test membrane protein model structural stability and relieve steric clashes based on previous ion channel simulations[63], the system was further simulated for 1 μs using Anton 2 software version 1.27.0 (i.e. achieving ~1.1 μs total simulation time). The channel pore remained well hydrated and open during this simulation time, with the pore domain RMSD drifting up to ~3 Å and the SF RMSD remaining mostly within ~1 Å as can be seen in **Fig. .2.4**. The HOLE program[64] was used to compute pore radius profiles.

2.2.4. Voltage application protocol

After 90 ns equilibration MD simulation described above, the equilibrated hERG channel model in the hydrated POPC bilayer was subsequently used for testing potassium ion permeation by applying transmembrane voltage during multi-microsecond simulations on Anton 2.[65] To do so, a uniform electric field was applied in *z* direction, and it can be computed as:

$$E_z = \frac{V}{L_z \cdot 43.5} \qquad \text{(Eq. 1)}.$$

Where V is the voltage in mV, E_z is the z component of the electric field vector in kcal/(mol·Å·e), and L_z is the length of the unit cell in z direction in Å. A factor of 43.5 was used to convert from mV/Å to kcal/(mol·Å·e). To prevent changes in applied voltage due to fluctuations in L_z, the system was simulated in the *NVT* ensemble. A voltage of +750 millivolts (mV) was selected as it was demonstrated to evoke fast ion permeation in models of K_V1.2/2.1 paddle chimera in a previous study[66]. hERG channel simulations under applied +750 mV voltage were run for 5 μs with multiple K^+ conduction evens detected (see **Fig. 2.3A**). Similar simulations were run for S641A hERG mutant, where no conduction events were observed during the ~2 μs simulation (**Figs. 2.6 & 2.7**). Lipid membrane electroporation was not observed during these simulations. A smaller applied voltage of +500 mV resulted in only a single conduction event during our multi-microsecond hERG simulations (data not shown).

2.2.5. K_V1.2/2.1 chimera ion conduction simulations

The K_V1.2/2.1 chimera model was similarly evaluated for K^+ conduction through application of +750 mV voltage in MD simulation on Anton 2 using the *NVT* ensemble and the same voltage application protocol as defined above. We selected the K_V1.2/2.1 paddle chimera channel (Protein Data Bank ID: 2R9R;[43]) as our initial structure, as it has been successfully used in assessing K^+ ion conduction previously[66]. The β subunit and tetramerization domains were removed, as in that study. The residue numbering from the K_V1.2/2.1 chimera structure, which if offset by 4 from that in the K_V1.2 sequence, was used throughout. This

truncated structure, henceforth referred to as the "K_V1.2/2.1 chimera" model, was then used to build an initial system with the CHARMM-GUI Membrane builder web toolkit [67]. This system was then equilibrated for 50 ns in the *NPT* ensemble using NAMD and the same parameters and conditions as specified above in the *General MD Simulation Setup* section. In total, the system contained ~127,000 atoms, including 72 potassium ions, 64 chloride ions for charge neutralization and providing a physiological 0.15 M salt concentration, and a lipid bilayer of 281 POPC lipids. The system was subsequently run in the *NVT* ensemble on Anton 2 for 5 μs. Voltage was applied using the protocol described above, but with the different electric field strength E_z scaled to account for a new unit cell height L_z and ensure the same transmembrane voltage of +750 mV.

2.2.6. Counting permeating K^+ ions during channel conduction simulations

Conduction for both the hERG and Kv1.2/2.1 chimera models was evaluated using the same protocol, wherein ion *z*-coordinate positions with respect to channel selectivity filter (SF) backbone center of mass (COM) were recorded and flagged for their presence within the ion channel pore, and filtered for ion *z*-coordinate positions for plotting. In this protocol, the whole system was re-centered with respect to the COM of the channel. Then, for every ion and frame of the simulation, the *xy* component of the position vector of a particular ion was recorded as a radial distance from the *z*-axis. These radii along with ion *z*-positions were then used to determine individual ion localization with respect to the channel pore, per ion and per frame: when this *xy* component was less than 10 Å, a distance inclusive to the entirety of the channel's conductive pathway, and the *z*-coordinate of the ion resided within *z* bounds encompassing the entire channel, then the particular ion *z*-coordinate position was flagged

as residing in the pore. The bounds used were as follows: hERG channel: -35≤ z ≤ 30 Å; for K_V1.2/2.1 chimera channel: -16 ≤ z ≤ 20 Å. Only flagged z-positions were plotted in K^+ conduction time series (**Figs. 2.1, 2.3A, & 2.7**), and permeation events were counted from the resultant plots.

2.2.7. Pore hydration measurements

To measure pore hydration, a VMD script was used to record the number of water molecules occupying the ion channel pore cavity at a given simulation time. The pore cavity was defined as the region of the ion channel from the bottom of the S6 helix to the base of the selectivity filter, incorporating the "cavity" ("S5") ion position formed by the hydroxyls of Ser624 of hERG or Thr370 for K_V1.2/2.1 chimera. Water molecules were counted if they were within a cylindrical selection defined to include the whole pore cavity. This cylinder had a radius of 10 Å, a base parallel to the membrane, and a height equal to the distance between the selectivity filter and the bottom of the S6 helix. Prior to measuring pore hydration, the entire system was re-centered about the center of mass of the selectivity filter.

2.2.8. Selectivity filter residue φ and ψ measurements

Protein backbone torsional angles (φ and ψ) were measured for the selectivity filter residues ^{624}SVGFG (hERG) or ^{370}TVGYG (K_V1.2/2.1 chimera) using VMD's Timeline plugin.

2.3 RESULTS

2.3.1. Equilibration and validation

We sought to develop an open, conducting model of the hERG based on the published cryo-EM structure[26]. This was achieved by rebuilding missing loop residues using Rosetta (see *Methods*) thus constructing a complete model of the hERG pore domain (PD) and voltage sensing domains (VSD) and tested the ability of this channel model to conduct K^+ ions in MD simulations. After an extended stage system equilibration (see **Table 2.1**), we performed a ~1 μs-long unbiased MD simulation, which revealed that the PD remained open with a pore radius of ~4 Å near intracellular activation gate, well hydrated and deviating from the initial structure by less than 3 Å (**Fig. 2.2**). As expected, we did not observe ion conduction events in this simulation running at zero voltage.

2.3.2. hERG channel model K^+ conduction under applied voltage

We observed multiple K^+ ion conduction events during an unrestrained, multi-μs MD simulation with an electric potential of 750 mV (positive inside) continuously applied along the *z*-axis of the system, corresponding to the membrane normal, as shown in **Fig. 2.1A.** The representative molecular snapshot of this open conducting hERG channel model in **Fig. 2.1A** demonstrates an open and solvent-accessible pore, while ions within the selectivity filter (SF) have adopted the canonical positions in an alternating "water-ion-water" orientation with ions at sites S1, S3 and cavity. Several frames from a representative conduction event of a K^+ ion (brown ball) across the SF are shown in **Fig. *2.1B*,** with other ions also colored to

match ion *z*-position traces from **Fig. 2.1C**. Ten conduction events through the channel were observed in ~5 μs total simulation time (**Fig. 2.3**), seven of which occurred within a 0.3 μs timespan, shown in **Fig. 2.3C.** The ion SF transitions that facilitate conduction depicted by the brown ion are mediated by both water-mediated or "soft" (t = 0.478 μs) and direct or "hard" (t = 0.490 μs) knock-on events shown in **Fig. 2.3B.** K^+ conduction ceases after 1.75 μs, coinciding with a marked reduction in the channel pore diameter and consequently pore dehydration (**Figs. 2.3 & 2.4**).

Seven conduction events occurred between t = 0.3 μs to and 0.7 μs and are shown in more detail in **Fig. 2.1** K^+ ions having a z-coordinate (with respect to the SF backbone center of mass) in the range $-25 \leq z \leq 4$ Å were defined as residing in the pore cavity. K^+ ions within the SF predominately occupied the [S1 S3] state, corresponding to z = –4 Å and z = +4 Å coordinates respectively. The [S2 S4] K^+ occupancy state occurred transiently and only coincidentally with the escape of an ion from S1. Both direct ("hard") and water-mediated ("soft") knock-on conduction events were observed.

The cessation of conduction after t = 0.7 μs coincides with the elimination of the S1 occupancy site and SF pinching at the S2 site, which was measured as the respective increase in opposing chain $C\alpha$ distances for Gly628 and decrease in $C\alpha$ distances for Gly626 (see green and blue traces in **Fig. 2.4B**). The three remaining conduction events occurred from t = 1.4 μs to 1.7 μs during closure of the pore at the intracellular gate, coinciding with a marked reduction in the channel pore diameter and consequently pore dehydration (**Fig. *2.4C*).**

2.3.3. Selectivity filter conformation and its effect on ion conduction

Conduction events were preceded and accompanied by marked changes in the SF conformation as shown in **Fig. 2.4A&B**. During the 0.300 μs conduction interval, the Gly628 and Phe627 residues of the SF adopted a flipped confirmation in which their carbonyl oxygens coordinated with water molecules located behind the SF, as opposed to those in the S1 and/or S0 sites. This consequently widened the top of selectivity filter, preventing ion occupancy of the S0 site, potentially facilitating escape of K^+ from S1. As a result, the arrangement of ion occupancy states transitioned predominantly from the "cavity, S3, and S1 state" to "cavity and S3 state" throughout the ion permeation simulations.

During the two periods of conduction, the φ and ψ backbone dihedral angles of Gly628, the top-most SF residue, exhibited 60 to 120-degree fluctuations and adopted asymmetrical conformations (**Fig. 2.4C**). In contrast, the non-conducting period of the simulation was associated with a 120-degree mostly systematic shift in Gly628 φ and ψ angles from the initial values (**Fig. 2.4A**) corresponding to elimination of the S1 site.

2.3.4. K_V1.2/2.1 chimera model K^+ conduction under applied voltage

The K_V1.2/2.1 paddle chimera channel (**Fig. 2.1D**) is a well-studied model that has been shown to conduct K^+ ions in MD simulations under applied voltage [66, 68]. Our K_V1.2/2.1 model was similarly induced to conduct by applying +750mV with 0.15M KCl. **Fig. 2.3B** is the entire 5.05 μs trajectory demonstrating multiple ion conduction events. K_V1.2/2.1

model conducts early on: 9 K^+ ions were observed to permeate from 0.050 μs to 0.350 μs, adopting either an [S1 S3] or [S2 S3] ion occupancy arrangement in the SF.

The pore of the $K_V1.2/2.1$ model remained open for a longer duration than the hERG model pore and avoided hydrophobic collapse, as indicated by their respective pore radii profiles produced by HOLE program (**cf. right panels in Fig. 2.3A&B**). However, there was substantial disordering of the K^+ ion SF sites S0-S4 by the end of the simulation corresponding to SF collapse, which occurred by 4.3 μs, resulting in a ~0.8 μs of ultra-rapid uncontrolled conduction. This period is visually apparent in the backbone torsional angles φ and ψ plots of the SF residues in **Fig. 2.5A**. This collapsed state was preceded by an asymmetrical increase in SF Thr370 $C\alpha \cdots C\alpha$ by 1 to 3 Å and pronounced SF pinching at Gly372 position, i.e., the SF center (**Fig. 2.5B**). These factors define the non-conducting, locked state in which ions are located solely at S4 site from 3.2 – 4.3 μs (**Fig. 2.3B**). One factor to consider is what role the rapid dehydration of the pore cavity at *t*=2.9 μs (**Fig. 2.5C**) has in establishing the conditions that facilitated pore collapse during the last portion of the simulation.

Prior to this collapse, there was a longer period of non-conductivity. This period began with SF dehydration and pinching at Gly374 starting at about 0.4 μs (**green traces in Fig. 2.5B**). After this time, K^+ ions were locked in the [S2 S3] occupancy arrangement that was favorable to conduction earlier in the simulation (**Fig. 2.3B***)*. However, there was also a reduction in pore hydration (**Fig. 2.5C**) after 0.4 μs in comparison to the initial conducting phase that may contribute to non-conduction. Interestingly, the $K_V1.2/2.1$ model had fewer fluctuations in

SF φ and ψ angles and Cα ··· Cα distances than in hERG channel model during their respective periods of conduction, suggesting that non-conduction in the K_V1.2/2.1 model is predominantly due to the pore temporarily and partially closing, as opposed to SF rearrangement observed in the hERG model. However, whether the structural rearrangements of different partially dehydrated pore conformations, and changes in a SF geometry we observed represent a particular ion channel state remain unclear and would require a separate study beyond the scope of this work.

2.2.5. The S641A mutant of hERG does not conduct

The S641A mutation is located behind the selectivity filter (**Fig. 2.6**) and is known to be associated with hERG channel facilitated inactivation [69]. Water-separated K^+ ions were placed in the selectivity filter according to their presentation in the original WT hERG channel model (see above), thus they occupy a soft knock-on conformation. The potassium ions trapped within the selectivity filter at [S2 S3] undergo significant position adjustments during equilibration voltage-free MD simulation but are exceptionally stable during the applied-voltage portion of the simulation (**Fig. 2.7A**). The selectivity filter's backbone torsional angles are remarkably static (**Fig. 2.7B**). in comparison to periods of conduction from the wild-type system (**Fig. 2.4A**). The mutant channel's Cα ··· Cα distances are similarly stable. Lastly, this channel undergoes a gradual decline in pore water coordination, indicating dehydration and potential collapse.

2.4 Discussion

We observed 70% more conduction events per unit time in the $K_V1.2/2.1$ runs than in hERG channel conduction runs. Interestingly, this difference is in line with hERG and $K_V1.2$ single-channel conductance observed experimentally (12.1-13.5 pS for hERG[68, 70] and 14-18 pS for $K_V1.2$[71]), although the small number of such events was not sufficient to draw any quantitative conclusions.

Moreover, we also observed long refractory periods in both hERG and the $K_V1.2/2.1$ channel simulations (**Fig. 2.1E and Fig. 2.3**). They are correlated with pinching of the middle or top of the SF for hERG and $K_V1.2/2.1$, respectively, which is evident by examining time series of distances between corresponding Gly residues (626 for hERG and 374 for $K_V1.2/2.1$), depicted in **Figs 2.4 & 2.5**. Interestingly, we observed top of the SF pinching and no ion conduction events in ~2 μs long simulations of S641A mutant of hERG under 750 mV applied voltage (**see Figs. 2.6 & 2.7**). This mutant is known to facilitate channel inactivation[69], and thus such pinching could potentially be related to C-type inactivation, although simulation time scales are drastically smaller. It is worth exploring the interaction networks and the role of water around the SF region, as an alanine mutation may affect the ability of water to coordinate behind the selectivity filter. Importantly, the absence of conduction events for this hERG mutant indicates that even at high voltages used in our simulations we can distinguish between conducting and non-conducting channel states.

The manner in which conduction ceases and resumes prior to pore collapse is of note. Restoration of the conductive selectivity filter state at t = 1.400 μs was mediated by subsequent knock-on events, the first of which results in an [S3 S4] ion arrangement (**Fig. 2.3A**). This arrangement widened the S2 site to make it accessible to water. Once the S2 site was solvated from the extracellular side, a subsequent knock-on attempt induced the blocking K^+ ion at S3 site to transition to S1. This allowed for the S2 position to be filled with an extracellular water.

The movement of the selectivity-filter-blocking ion across collapsed region of the hERG SF, and the reintroduction of water to S2 induced rotations in Gly626 and Phe627, resulting in a state that resembles the original conducting orientation, and conduction resumed briefly. However, the pore cavity narrowed substantially by 1.4 μs, and coincided with reduced pore solvation, and further conduction ceased (**Fig. 2.4C**). The pore radius at the intracellular gate was substantially reduced beyond this point (**Fig. 2.3A**) indicating channel pore hydrophobic collapse. The S641A mutant similarly undergoes hydrophobic collapse within two microseconds. This contrasts to the multiple microseconds wherein the $K_V1.2/2.1$ pore is open and solvent accessible. Further analysis is warranted to understand this behavior in the hERG channel models, and additional conduction simulations using restraints exclusively within the hERG channel pore should be considered when trying to access maximal conductance.

2.4.1. Future Directions

As hERG channel inactivation is crucial to its physiological function, and many drugs prefer inactivated-state binding, a molecular model of inactivated hERG channel is essential for advancing the field of predictive computational safety pharmacology. A recent work by Asai et al. presents two new cryo-EM models of hERG channel: one in a possibly non-conducting inactivated conformation (PDB ID: 7CN0) and another bound to the hERG blocker astemizole(PDB ID: 7CN1)[72].The authors allude to a reorientation of the F627 residue of the selectivity filter as affecting conduction. It is a curious proposition; our findings here suggest that F627 residues on opposing domains adopt the same φ angles which are different those of the adjacent domains. When examining the first few hundred microseconds, it seems that φ angles do not fluctuate during periods of conduction but adopt similar orientations during nonconduction (**Fig. 2.4A**). During conduction ψ fluctuates minimally. Given these findings, the next step will be to simulate this new model under identical conditions, with a particular focus on the role of F627 to assess whether this model similarly conducts. The importance of this residue has been previously demonstrated by others[73, 74]. Ultimately, F627 backbone orientations should inform restraints, and may aid in replicating maximal conductance of hERG in future simulations and inducing inactivation in both cryo-EM models should be the first step in future investigations.

Time, Ns	Restraint, Kcal/mol/ Å^2	Protein Domain
1-5	1.0	Backbone
5-10	1.0	Pore Domain
10-15	0.5	Pore Domain
15-20	0.25	Pore Domain
20-30	0.1	Pore Domain
30-40	0.1	Selectivity Filter

Table 2.1. Restraint regime for hERG MD equilibration simulations.

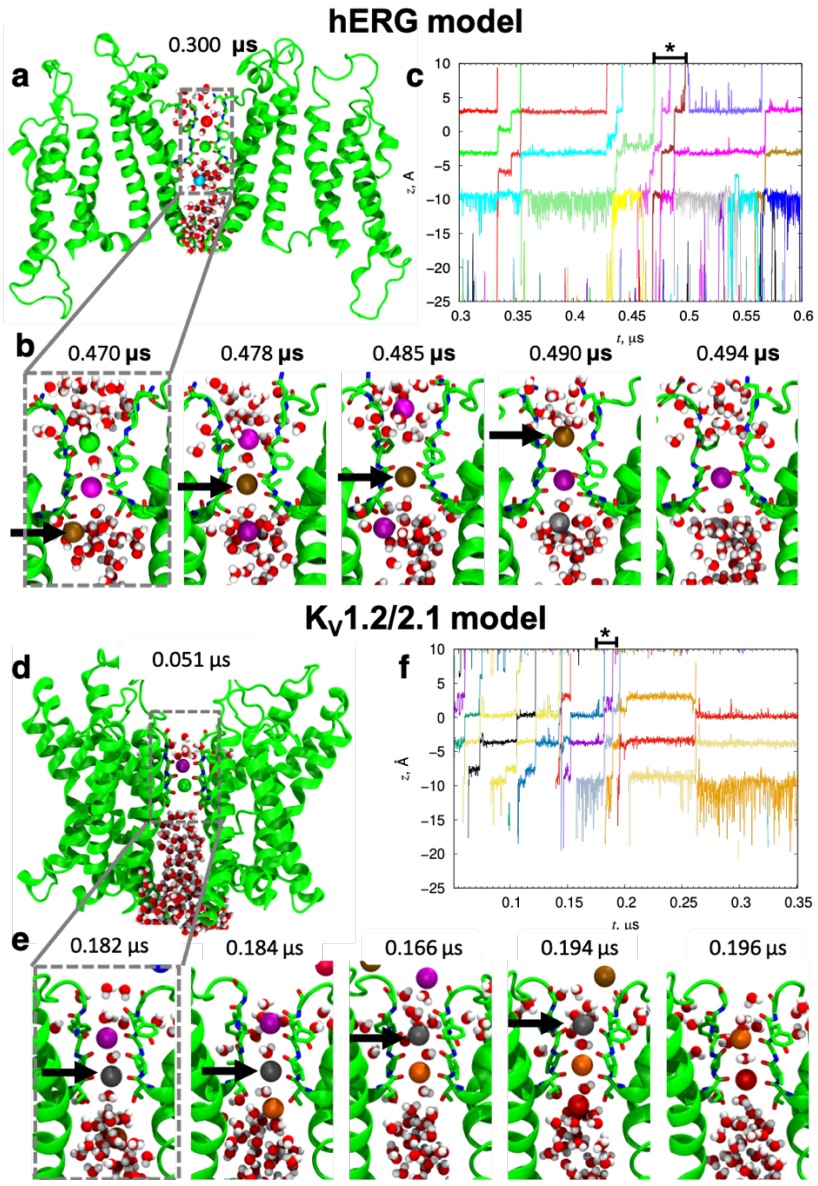

Figure 2.1. K^+ conduction of open-state hERG and K_V1.2/2.1 chimera channel models under an applied 750 mV voltage. 0.3 μs fragments of 5 μs trajectories, where most conduction events took place, are shown. (**a**, **d**) Initial frames in these fragments (t = 0.300 and 0.051 μs, respectively) showing two opposite protein chains (green ribbons with SF S624-G628, S6 helix Y652 and F656 residues for hERG and SF T370-G374 residues for K_V1.2/2.1 shown as sticks with red O and blue N), pore ions (colored balls) and waters (red/white). (**b**, **e**) Close-up views of the channel SF in the same representation at different time points, showing a complete translocation of one ion (brown or gray ball, respectively), indicated by an arrow. (**c, f**) Time series of ion z-positions (with respect to the SF backbone center of mass). Colors of the z profiles match those of the ions in panels **a**, **b** and **d**, **e**. Portions of the profiles corresponding to snapshots in panels **b** and **e** are indicated with an asterisk.

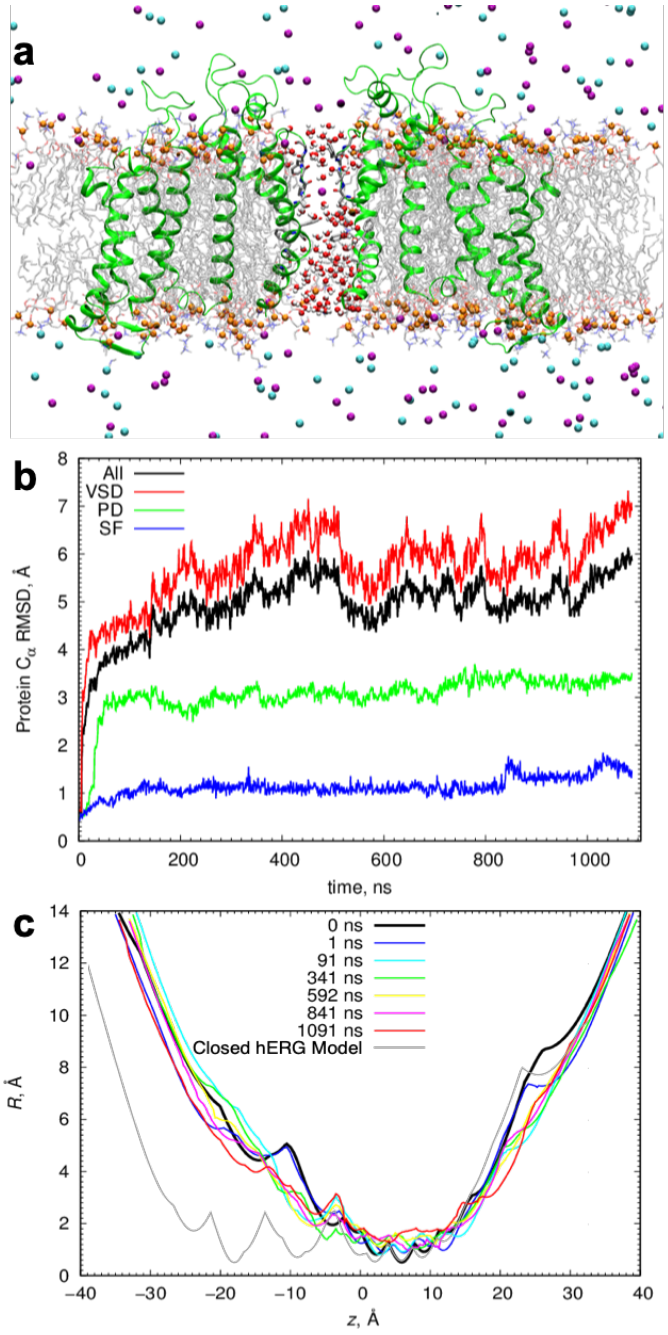

Figure 2.2. Stability of open state hERG model. (**a**) Molecular system snapshot at the end of 1 μs unbiased MD simulation. Two opposing hERG subunits are shown. Protein backbone is shown as green ribbons (with SF S624-G628, S6 helix Y652 and F656 residues shown as sticks), lipid headgroups as orange balls, lipid tails as grey thick sticks, SF atoms shown as colored sticks, K^+ ions as purple and Cl^- ions as cyan balls, pore waters as red/white spheres. Bulk water is not shown for clarity. (**b**) Protein C_α root-mean-square deviation (RMSD) time series broken down by domain. (**c**) pore radius profiles at selected time points**.**

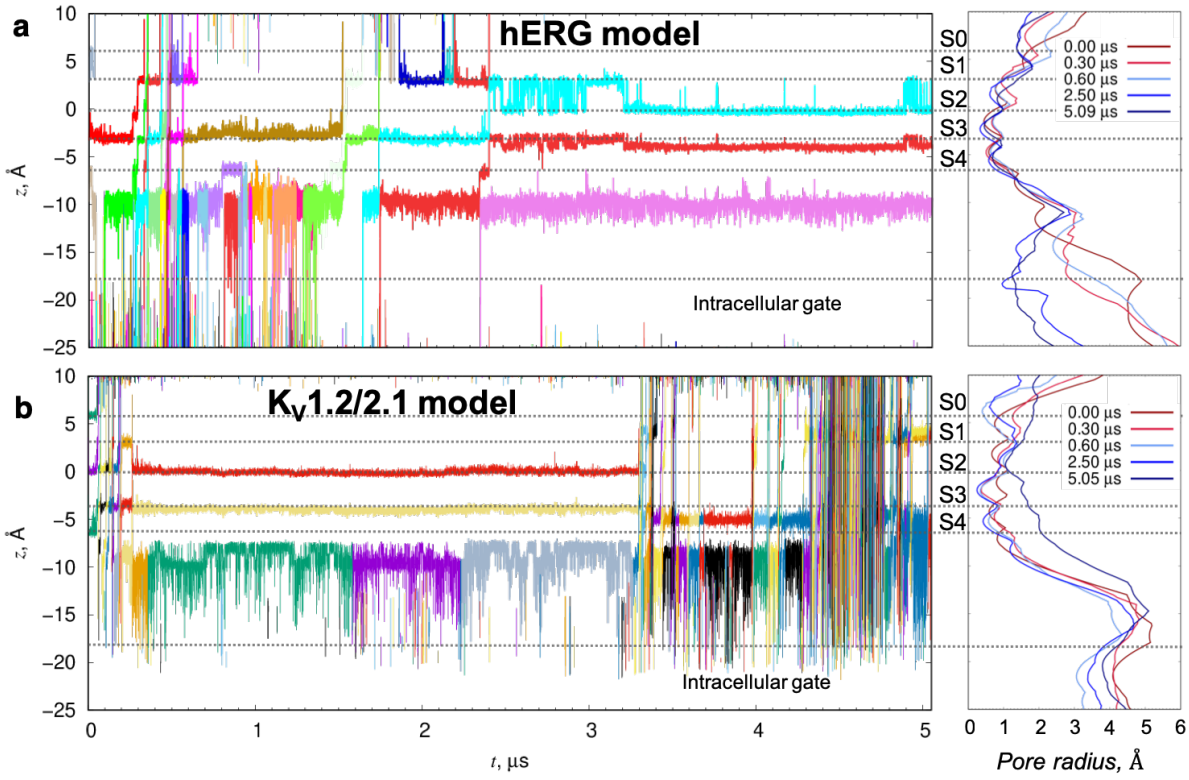

<u>Figure 2.3.</u> Complete time series of K^+ pore positions in hERG (a) and K_V1.2/2.1 chimera (b) channel models under an applied 750 mV voltage and corresponding pore radius profiles. *Left*: Individual K^+ *z*-coordinate positions (colored traces) for the full duration of the ~5 μs MD simulations. *z*-coordinate positions of SF K^+ ion occupancy sites are denoted with canonical S0-S4 notation, as is the location of the intracellular gate. *Right:* pore radii of the channel models measured at 5 timepoints to reflect pore narrowing and/or elimination of SF ion occupancy sites.

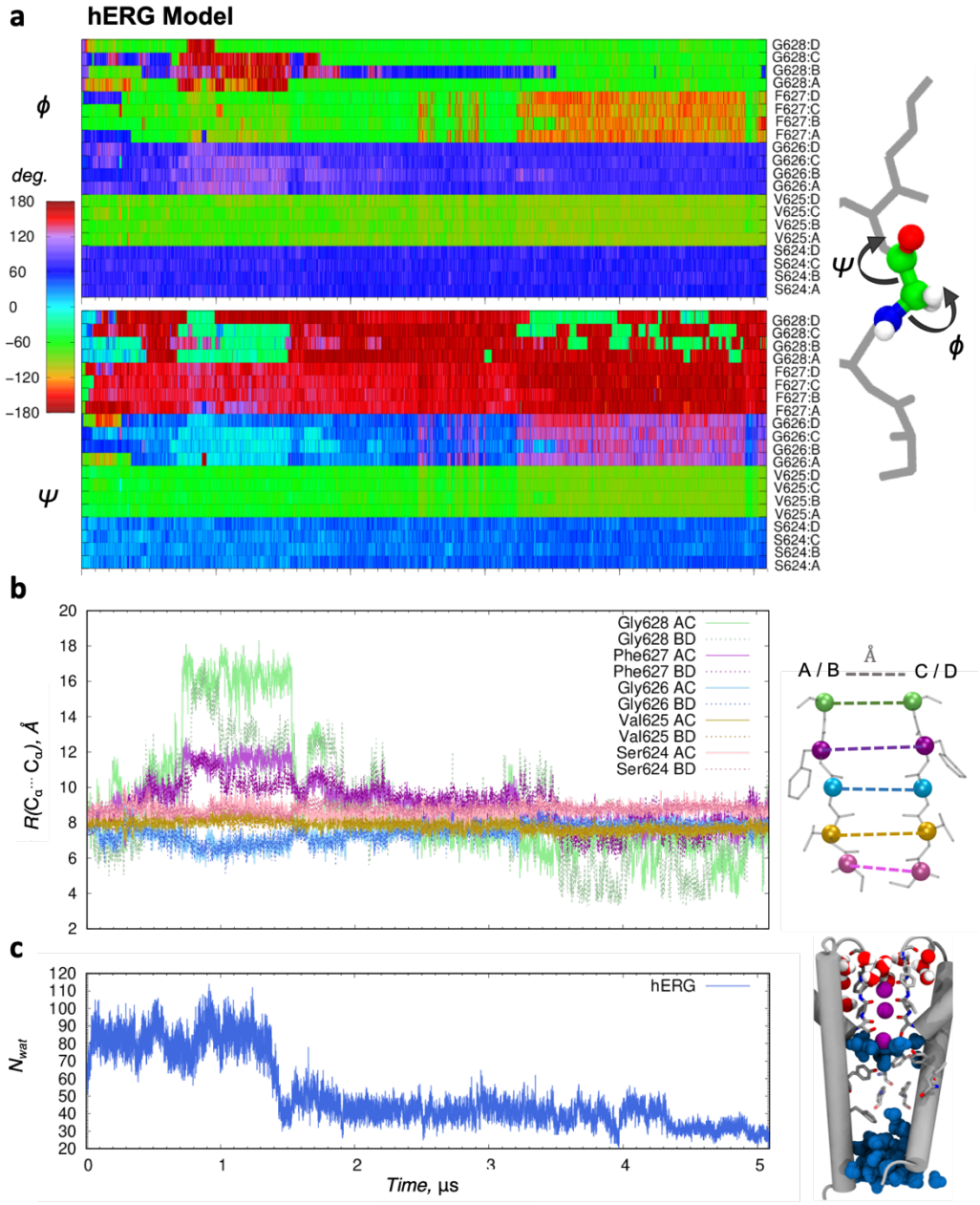

<u>Figure 2.4.</u> Structural analysis of hERG from MD simulations under applied 750 mV voltage. (**a**) *Left:* Time series of φ and ψ protein backbone dihedral angles of SF residues SVGFG. *Right:* Graphical representation of φ and ψ dihedral angles in the SF. (**b**) *Left*: Time series of distances between protein backbone C_α atoms between SF residues in the opposing chains. *Right:* Depiction of the distances being measured, with protein chains "A" and "B" opposite to "C" and "D", respectively. (**c**) *Left:* Time series of pore hydration as measured by number of water molecules within the pore. *Right:* Snapshot of pore hydration at the final simulation frame (t = 5.090 μs). Relevant water molecules occupying pore are colored blue and correspond to the plotted quantity on the left. Water molecules behind SF are red/white.

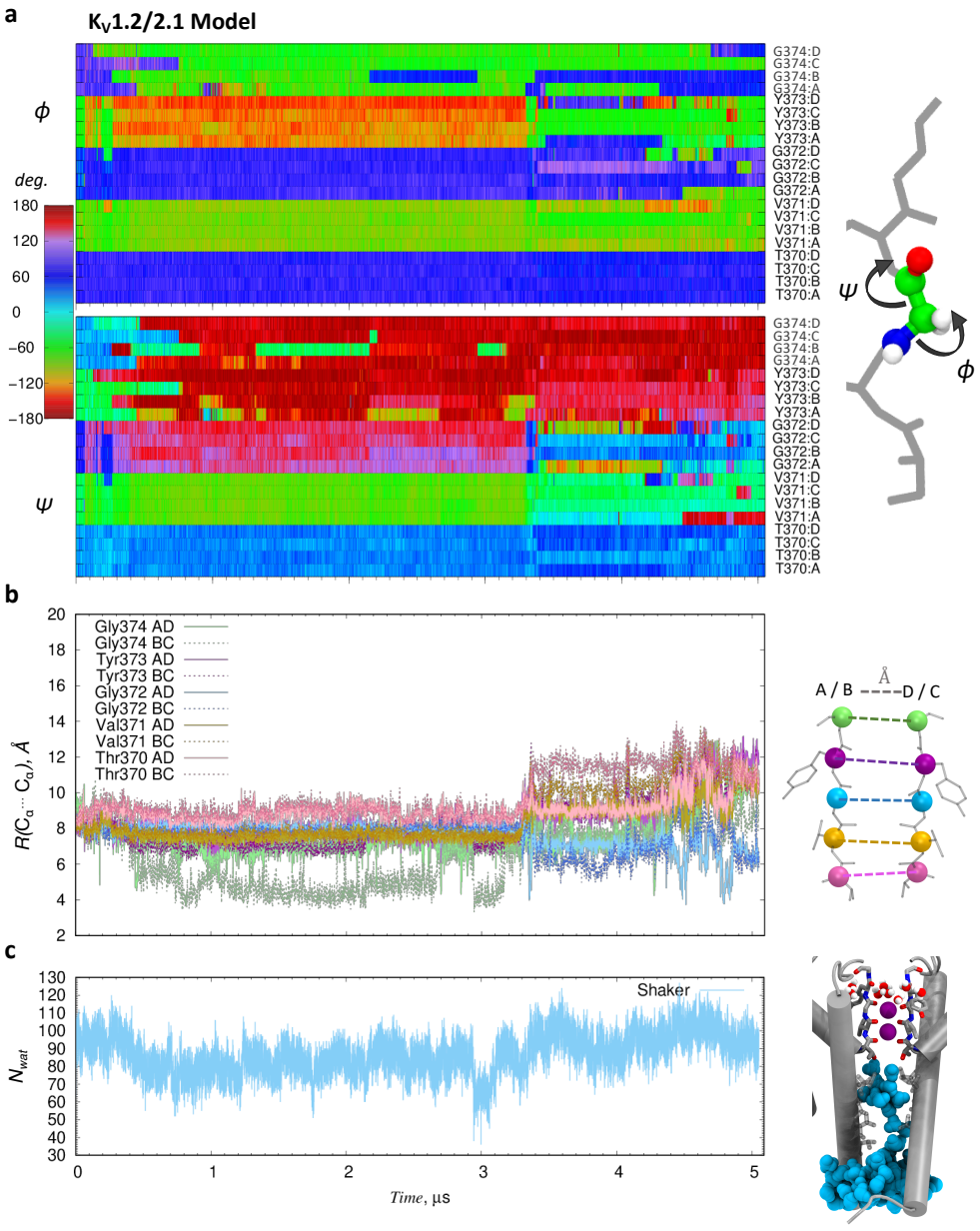

Figure 2.5. Structural analysis of K$_V$1.2/2.1 chimera from MD simulations under applied 750 mV voltage. (**a**) *Left:* Time series of φ and ψ protein backbone dihedral angles of SF residues TVGYG. *Right:* Graphical representation of φ and ψ dihedral angles in the SF. (**b**) *Left*: Time series of distances between protein backbone C_α atoms between SF residues in the opposing chains. *Right:* Depiction of the distances being measured, with protein chains "A" and "B" opposite to "D" and "C", respectively. (**c**) *Left:* Time series of pore hydration as measured by number of water molecules within the pore. *Right:* Snapshot the lowest degree of pore hydration (t = 2.998 μs) as measured by water molecules within the pore. Relevant water molecules occupying pore are colored light-blue and correspond to the plotted quantity on the left. Water molecules behind SF are red/white.

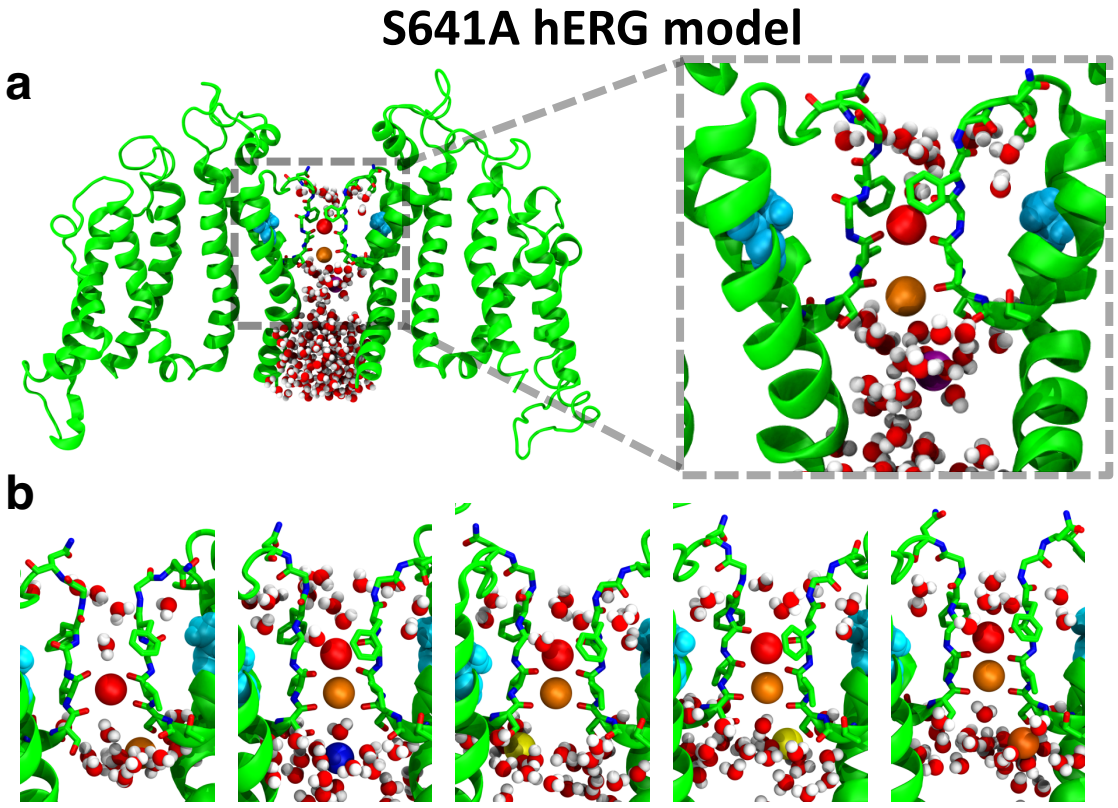

<u>Figure 2.6.</u> K^+ pore positions for S641A hERG mutant channel model under an applied 750 mV voltage. A) Representative frame showing two opposite protein chains (green ribbons with SF S624-G628, S6 helix Y652 and F656 residues shown as sticks with red O and blue N, mutated Ala 641 residue shown as cyan in a space-filling representation),pore ions (colored spheres) and waters (red/white). Inset on the right shows closed-up view with SF pinched at the top clearly visible. **B**) Close-up views of the channel SF in the same representation at different time points, showing no K^+ ion translocation for this hERG channel mutant during a 2 μs simulation with applied 750 mV voltage.

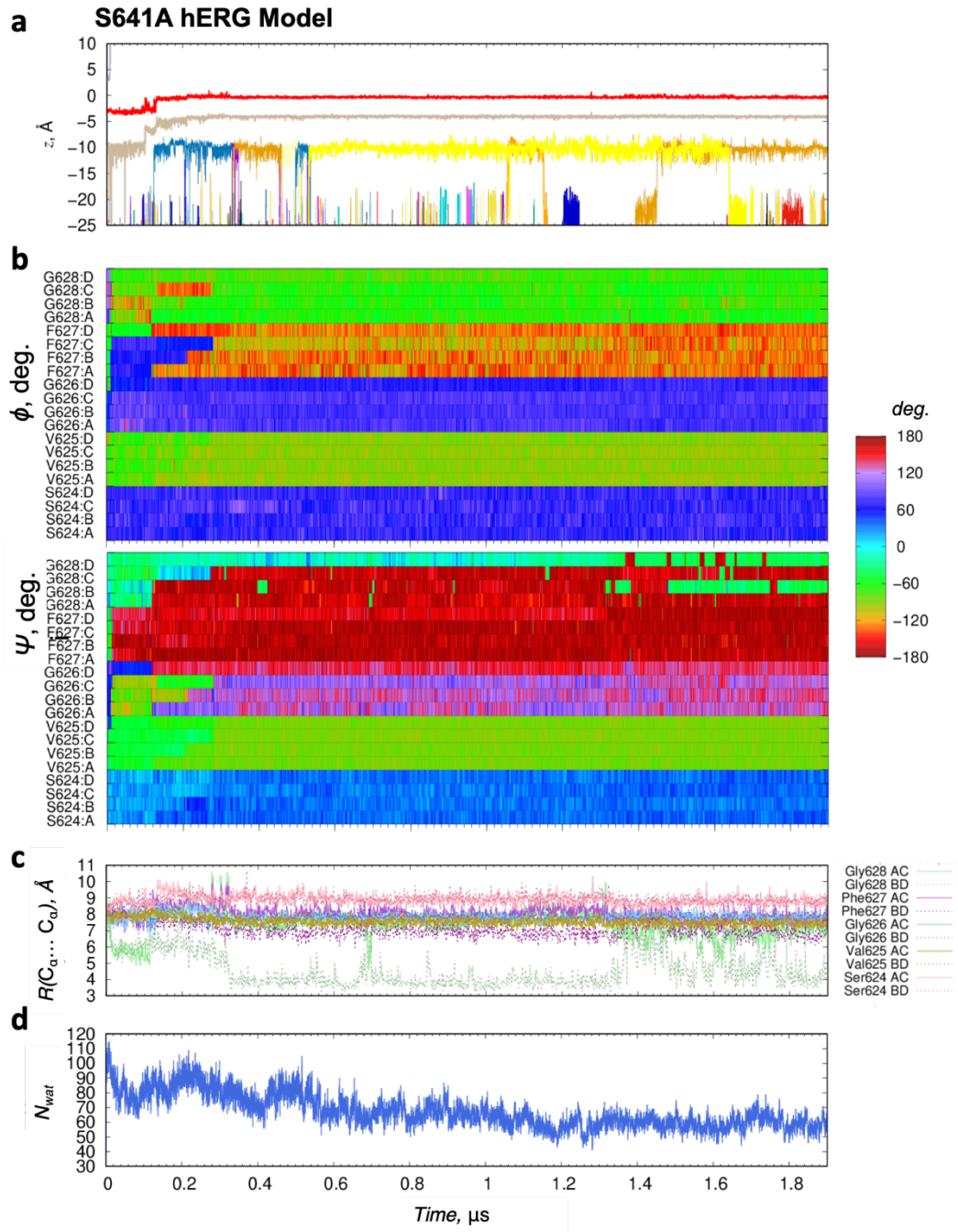

Figure 2.7. Structural analysis of S641A hERG channel mutant model from MD simulations under applied 750 mV voltage. (**a**) Time series depicting *z*-positions of K^+ ions (with respect to SF backbone center of mass) in the channel pore indicates no ion conduction in ~2 μs. (**b**) Time series of φ and ψ protein backbone dihedral angles of SF residues SVGFG for each chain. (**c**) Time series of distances between protein backbone C_α atoms between SF residues in the opposing chains ("AC" or "BD"). (**d**) Time series of pore hydration as measured by a number of water molecules within the pore.

Chapter 3. Molecular Determinants of Pro-Arrhythmia Proclivity of d- and l-Sotalol via a Multi-Scale Modeling Pipeline

Acknowledgements: This chapter is comprised of the following published paper: DeMarco et al., Molecular determinants of pro-arrhythmia proclivity of d- and l-sotalol via a multi-scale modeling pipeline, *Journal of Molecular and Cellular Cardiology*, Volume 158, Sept. 2021, Pages 163-177, ISSN 0022-2828, doi: 10.1016/j.yjmcc.2021.05.015. It is freely available on PubMed central, PMCID: PMC8906354.

My contributions to this immense work are confined to the characterization of hERG channel interactions with d- and l-sotalol in unbiased drug flooding and enhanced sampling molecular dynamics (MD) simulations. I performed analyses of drug flooding MD simulations, assessed the effectiveness of drug orientation and conformation sampling for umbrella sampling MD (US-MD) and Hamiltonian replica exchange US-MD (HREUS-MD) simulations, examined residue-level protein – drug interactions within the hERG channel pore, and produced figures of these findings. This includes making figures 3.2, 3.3B, and 3.4D. I did not however setup or run those simulations, nor did I calculate kinetic parameters used in the functional scale modeling, which is the work of the first author, Dr. Kevin DeMarco. My other contributions are available within the Supplemental Materials 1 and include figures S7-S11, and S15. Supplementary materials can be found with the publication on Science Direct:

https://www.sciencedirect.com/science/article/pii/S0022282821001097

Molecular determinants of pro-arrhythmia proclivity of d- and l-sotalol via a multi-scale modeling pipeline

Kevin R. DeMarco[1], Pei-Chi Yang[1], Vikrant Singh[2], Kazuharu Furutani[1,3], John R. D. Dawson[1,4], Mao-Tsuen Jeng[1], James Fettinger[5], Slava Bekker[1,6], Van A. Ngo[7], Sergei Y. Noskov[7], Vladimir Yarov-Yarovoy[1,8], Jon T. Sack[1,8], Heike Wulff[2], Colleen E. Clancy, [1,2] and Igor Vorobyov[1,2*]

[1] Department of Physiology and Membrane Biology
University of California Davis, Davis, CA 95616, USA

[2] Department of Pharmacology
University of California Davis, Davis, CA 95616, USA

[3] Department of Pharmacology, Faculty of Pharmaceutical Sciences, Tokushima Bunri University, Tokushima, Tokushima 770-8514, Japan

[4] Biophysics Graduate Group
University of California Davis, Davis, CA 95616, USA

[5] Department of Chemistry
University of California Davis, Davis, CA 95616, USA

[6] Department of Science and Engineering, American River College, Sacramento, CA 95841

[7] Centre for Molecular Simulation and Biochemistry Research Cluster,
Department of Biological Sciences,
University of Calgary, 2500 University Drive, Calgary, AL T2N1N4, Canada

[8]Department of Anesthesiology and Pain Medicine
University of California Davis, Davis, CA 95616, USA

[*] Correspondence: Igor Vorobyov, Ph.D.
University of California, Davis,
Department of Physiology and Membrane Biology
4303 Tupper Hall, One Shields Ave, Davis, CA 95616-8636
E-mail: ivorobyov@ucdavis.edu

3.1. Introduction

Drug stereoisomers are increasingly viewed as potentially useful means to develop and test pharmacological agents [75, 76] due to potentially more potent and/or selective action on their intended protein targets. Stereoisomerism also plays a crucial role in drug toxicity profiles with enantiomers possessing different, on- and off-target effects and capacities for metabolic degradation [77]. This phenomenon is well-described in the drug-induced cardiac toxicity [78] for commonly used drugs including an opioid methadone [79, 80], an anti-malarial drug quinine and its diastereomer quinidine [81, 82], the local anesthetics bupivacaine and ropivacaine [83-87] as well as for the calcium channel blocker verapamil used in the context of cancer chemotherapy [88, 89].

A fascinating and puzzling example of isomerism to impact cardiac safety is the antiarrhythmic sulfonamide drug sotalol. The d-isomer was infamously shown in the SWORD (Survival With ORal D-sotalol) clinical trial [17] to increase mortality and risk of sudden cardiac death in patients, leading to its withdrawal [4]. The racemic mixture comprising d- and l-sotalol, however, is widely used as an effective antiarrhythmic – although not entirely without risk [11, 90-100]. For instance, a prevalence of torsades de pointes (TdP) arrhythmia was estimated to be 0.1–7% depending on therapeutic doses, sex (significantly larger for women) and co-morbidities [99, 101-106]. The apparent disparity in cardiac risks of the racemic mixture compared to a pure d-enantiomer could be attributed to differences in interactions between sotalol stereoisomers and cardiac K^+ channel proteins, or from the higher efficacy of l-sotalol to act as a beta-blocker [107-111]. Here, we developed a multiscale approach combining cellular and tissue functional kinetic modeling with

atomistic simulations and experiments to reveal the specific ion channel interactions with d- and l-sotalol and unveil elusive molecular mechanisms underlying stereospecificity of arrhythmia provoking drug-induced cardiotoxicity.

Cardiotoxicity in the form of abnormal heart rhythm is one of the most critical regulatory concerns for drugs and has resulted in withdrawal of a number of therapeutic agents. Drug-induced arrhythmia has been estimated to affect pharmaceuticals from multiple drug classes [112], with an estimated 3% of all prescription drugs worldwide harboring pro-arrhythmic side effects [113]. Indeed, cardiotoxicity is one of the leading causes of drug attrition [1], and accounts for 22-28% of US post-marketing drug withdrawal [2]. The problem of cardiotoxicity has even plagued drugs intended to treat arrhythmias like sotalol [4, 114]. Such deleterious drug side effects have been linked to blockade of the potassium current through the cardiac ion channel protein $K_V11.1$, encoded by the human *Ether-à-go-go*-Related Gene (hERG) [27, 28, 115]. Block of cardiac hERG current (I_{Kr}), causes prolongation of the QT interval on the surface electrocardiogram (ECG), sometimes causing potentially deadly arrhythmias [3, 27, 116]. While not all hERG block and QT prolongation leads to increased risk of arrhythmia, there is no reliable method to distinguish unsafe hERG blockers from safe drugs [117, 118], which hinders the pharmacological assessment of cardiotoxicity and may lead to attrition of safe and effective pharmaceuticals.

A recently proposed Comprehensive in Vitro Proarrhythmia Assay (CiPA) initiative is intended to address this need by improving predictions of drug pro-arrhythmia proclivities through the combination of multi-scale modeling and *in vitro* experimental assays [14, 119].

However, the CiPA platform does not yet provide a ready-to-go recipe on how to predict drug arrhythmogenicity. The example of sotalol discussed in this study, where two stereoisomers have different pro-arrhythmia proclivities, is especially challenging. Atomistic molecular dynamics (MD) simulations of hERG – drug interactions, which we employed here, can be used to help identify stereoselective protein – drug interactions [120, 121] and thus molecular determinants of drug-induced arrhythmogenesis. However, since cardiac arrhythmia is an emergent phenomenon, manifesting at the cardiac tissue and whole heart scales [122-125], we set out to create a link between atomistic-scale protein and drug structure-based MD simulations and functional kinetic simulations of cardiac cells and tissue. Recently, we developed such an integrative computational modeling approach that spans scales from the atom to the cardiac rhythm and were able to accurately predict pro-arrhythmia proclivities for dofetilide and moxifloxacin, hERG blockers with different cardiac safety profiles and directly link them to clinical data [16].

Here, we set out to investigate and reveal the stereospecific molecular mechanisms of d- and l-sotalol causing ventricular arrhythmogenesis by applying a multi-scale modeling pipeline from the atomistic to the tissue scale. We have previously developed and validated atomistic force field parameters for cationic and neutral states of sotalol [126], and validated open conducting atomistic models of the hERG channel [16, 73, 127] based on a high-resolution cryo-EM structure (PDB ID: 5VA2) [26]. Sotalol is known to access the hERG channel pore via an open state, with subsequent hERG inactivation stabilizing the drug – channel interaction [128]. In this work, we used multi-microsecond long unbiased MD simulations with saturating sotalol concentrations to reveal key binding modalities for cationic and

neutral d- and l-sotalol. Then, we used enhanced sampling MD simulations [16, 127] to compute state-dependent affinities and "on"/"off" rates for open hERG channel – sotalol interactions, which we used as parameters for our functional kinetic model. We optimized the model for inactivated state block to reconcile and predict emergent pro-arrhythmia risks at cardiac cell and tissue scales [16]. To test model predictions, we obtained d- and l-sotalol through enantiomeric separation and conducted electrophysiological recordings of their hERG channel block. We found the affinities of both enantiomers to hERG channel to be comparable. Our MD simulation informed functional cardiac cell and tissue models predicted sotalol induced QT interval prolongation due to a combined effect of hERG channel block and stereoselective beta-adrenergic receptor (βAR) inhibition to be in good agreement with clinical data.

3.2. Methods

A brief overview is provided below. See *Appendix A Supplementary Materials* for a more detailed description.

3.2.1 Atomistic simulations

We used our atomistic structural model of open hERG channel [16], based on the cryo-EM structure (PDB ID: 5VA2) [26] and generated using Rosetta molecular modeling software [40, 41, 53] as well as all-atom force field parameters of cationic and neutral sotalol [126]. Standard CHARMM36 all-atom force fields for protein, lipid, ions [59-61] and TIP3P water model [62] were used as well. Our hERG channel model was embedded in a 1-Palmitoyl-2-oleoylphosphatidylcholine (POPC) bilayer and solvated by 0.15 M aqueous KCl solution and

sotalol molecules using CHARMM-GUI [129] and equilibrated using a staged protocol by gradually reducing restraints [127] using NAMD program [130]. 8 μs long unbiased MD simulations with 23 sotalol molecules in aqueous solution corresponding to an initial 0.05 M concentration were run on Anton 2 [65]. Steered MD simulations with a sotalol molecule pulled from an intracellular aqueous into the hERG channel pore in five restrained 90 ns runs were used to seed umbrella sampling MD (US-MD) simulations [131]. Positional harmonic restraints for pore domain C_α and SF backbone non-H atoms to preserve an open hERG channel conformational state were reduced from 1.0 kcal·mol^{-1}·Å^{-2} in steered MD runs to 0.2 kcal·mol^{-1}·Å^{-2} during first 5 ns of US-MD runs and kept for the remainder of those and for the entire Hamiltonian replica exchange US-MD (HREUS-MD) [132] simulations. hERG channel residue sidechains and sotalol conformations were not restrained. US-MD simulations ran for 50 ns (including 10 ns equilibration) per each US-MD window, located at $-50 \le z \le -5.5$ Å in 0.5 Å intervals using 10 kcal·mol^{-1}·Å^{-2} harmonic restraints. $z = 0$ is the center of mass of hERG selectivity filter (SF) C_α atoms. HREUS-MD simulations followed US-MD runs after 20 ns and continued for 60 ns per each window. Free energy profiles and diffusion coefficients were computed from those simulations and used to calculate dissociation constants ($\boldsymbol{K_D}$) as well as drug "on" ($\boldsymbol{k_{on}}$) and "off" ($\boldsymbol{k_{off}}$) rates [16] used as our functional model parameters.

3.2.2. Functional simulations

We used a previously published approach [16] to develop functional kinetic models of hERG channel – sotalol interactions based on the wild-type drug-free hERG Markov model [16]. MD-derived $\boldsymbol{K_D}$, $\boldsymbol{k_{on}}$ and $\boldsymbol{k_{off}}$ values were used to simulate open-state hERG channel block,

whereas for the inactivated state block $\boldsymbol{K_{Di}}$ was assumed to be 4.3-fold less in the model 1 based on ref. [133] and 63-fold less than $\boldsymbol{K_{Do}}$ in the model 2 using a top-down optimization approach and ref. [134]. Rates for the inactivated state block were optimized using experimental dose response curves from this work and ref. [134] for models 1 and 2, respectively, and expression $\boldsymbol{k_{off} = k_{on} \cdot K_D}$. These hERG – sotalol models were implemented into the O'Hara-Rudy human ventricular cardiac myocyte model [135] to simulate QT interval in pseudo-ECG recordings from a 1-dimensional strand of O'Hara-Rudy cells paced at 1000 ms basic cycle length (BCL) as was done previously [16]. Beta-adrenergic stimulation by isoproterenol (ISO) was implemented through setting protein kinase A (PKA) phosphorylation effect to maximum, and its inhibition by sotalol, i.e. beta-blockade, was modeled as $1/(1+[\text{sotalol}]/K_i)$ where [sotalol] is drug's plasma concentration and K_i is its inhibition constant, which is 38,000 ng/ml for d-sotalol and 650 ng/ml for l-sotalol (35). Sotalol-induced QT prolongation was compared with clinical data at the matching BCL (RR interval) [136].

3.2.3. Experimental methods

Free sotalol base was prepared from sotalol hydrochloride salt through dissolving it in methanol and KOH solution, separation of supernatant, dissolving it in ethyl acetate, filtering and evaporating. High performance liquid chromatography (HPLC) resolution of the two sotalol enantiomers from free base sotalol was performed with an Agilent 1100 HPLC equipped with a Chiralpak IA 4.6 X 250 mm column, heated at 25°C. An isocratic solvent system consisting of 20% mobile phase A (ethanol with 0.1% diethyl amine) and 80% mobile phase B (hexane with 0.1% diethyl amine) was used for 15 min for each run. Sotalol was

detected by its absorption at 220 nm using an Agilent 1100 diode array detector (DAD). Under these conditions (*S*) sotalol enantiomer has t_R = 7.99 min. while (*R*) sotalol enantiomer has t_R = 11.88 min. Multiple runs using this method furnished about 25 mg of each enantiomer with almost 100% enantiomeric excess. The separated enantiomers were characterized by ^{1}H-NMR and proton decoupled ^{13}C-NMR (^{13}C-NMR^{1}H) spectra as well as X-ray crystallography using established methodology [137]. Please see details in the *Appendix B Data Supplement* and linked spectra files therein.

For electrophysiological recordings we used a human embryonic kidney (HEK) 293 cell line stably expressing hERG maintained in minimum essential medium supplemented with 10% fetal bovine serum and 400 μg/ml G418 as previously described [138]. HEK cells were continuously superfused with HEPES-buffered Tyrode solution. Membrane currents were recorded in the whole-cell configuration established using pipette suction [139]. Leak compensation was not used. Experiments were performed at room temperature (22-25°C). The data were stored on a computer hard disk and analyzed using PatchMaster and Igor Pro 7 (WaveMetrics, Portland, OR). The IC_{50} for hERG block by sotalol were measured by fitting the data to Hill's equation as follows:

$$f(D) = \frac{1}{1 + (D/IC_{50})^{h}}$$

Where $f(D)$ is the current ratio in the presence of the drug at a given concentration (D) and h is the Hill coefficient.

The data and datasets generated and analyzed in the current study can be accessed upon request sent to the corresponding author of the manuscript.

3. Results

3.3.1. hERG channel binding sites and pathways from sotalol flooding simulations

We previously developed atomistic force field parameters for cationic (+) and neutral (0) forms of sotalol and used MD simulations of their lipid membrane partitioning to validate those models showing water - membrane interface accumulation of sotalol(0) as well as significant free energy barrier and membrane perturbation for sotalol(+) [126]. This indicates ionization state-dependent energetics and kinetics of sotalol – lipid membrane interactions and may affect how the drug gains access to the hERG channel pore.

Here, we explicitly explored this using 8 μs long unbiased MD simulations of our open-state hERG channel model embedded in a POPC lipid bilayer and soaked by an aqueous solution with 0.15 M KCl and an initial 0.05 M concentration of sotalol in water, corresponding to 23 molecules in the simulation box. Utilizing these so-called drug flooding MD simulations, we were able to elucidate potential entry pathways and binding sites for d- and l- sotalol(+) and sotalol(0) interacting with the hERG channel. The distributions for cationic and neutral forms of each enantiomer were notably different (**Fig. 3.1** and *Appendix A* **Figs. S6-S7)**. d- and l-sotalol(0) (**Fig 3.1B, left panels**) were found to embed into the membrane and interact with hERG channel, whereas d- and l-sotalol(+) (**Fig. 3.1B, right panels**) remains predominantly in aqueous solution, sampling much more of the solvent space over the duration of the simulation (see drug aqueous concentration time series and atomic density distribution plots, *Appendix A* **Figs S6 and S7**).

Dominant binding poses of cationic and neutral d- and l-sotalol are shown in **Fig. 3.2**, whereas time series of drug binding *z* positions in the hERG pore are shown in *Appendix A* **Fig. S8**. Interestingly, one d-sotalol(0) or l-sotalol(+) molecule were observed to bind deep into the hERG pore, just below the selectivity filter (SF) region and interacting with the canonical drug binding F656 and Y652 hERG residues [33, 140-143] in the pore lining S6 helices (drug molecule M2 in **Figs 3.2A and D**) for most of 8 μs long MD runs, while another drug molecule was observed to transiently bind below, interacting with F656 and/or Y652 from another domain as well as S660 and other residues at the bottom of S6 helices (M1 in **Figs 3.2A and D**). Interestingly, for l-sotalol(0) and d-sotalol(+) systems, we observed only transient binding of one or two drug molecules at the bottom of hERG channel pore interacting with S660 and other S6 helix residues there (**Figs 3.2B and C** and *Appendix A* **Fig. S8B and C**) Hence up to two sotalol molecules were able to bind to the hERG pore, in agreement with our electrophysiological data (as described below). Sotalol flooding MD simulations demonstrated that d- and l-sotalol are likely to enter the hERG channel pore through the aqueous intracellular gate and did not reveal any drug entry through lipid facing fenestrations as in the case of Na_V channels [63, 144-146] and also suggested for some hERG binding drugs such as ivabradine [147, 148]. Thus, sotalol hERG pore binding pathways closely resemble those for dofetilide [16, 127, 147, 148], which also has methanesulfonanilide moieties and fairly similar polarity [149].

These qualitative observations do not exclude other possibilities since even very long simulation times of 8 μs might not be sufficient to fully sample other potential drug binding poses and pathways, which can be related to distortions of the hERG pore domain (*Appendix*

A **Fig. S9**) including partial asymmetric pore closure as evidenced by decrease in interchain $C_\alpha \cdots C_\alpha$ distances for S6 segment F656 and/or S660 residues (*Appendix A* **Fig. S10**) as well as selectivity filter (SF) distortions revealed by interchain $C_\alpha \cdots C_\alpha$ distances of S624 to G628 SF residues (see *Appendix A* **Fig. S11**). These structural changes are similar to those observed for a non-conducting state of the hERG channel during a multi-microsecond long MD simulation under an applied transmembrane voltage [127] and may be indicative of a channel transition to a different conformational state, possibly inactivated. Moreover, sotalol contacts with hERG residues during drug flooding MD simulations were asymmetric and highly variable among MD runs (See *Appendix A* **Figs. S12-S13**) due to long-lasting interactions (*Appendix A* **Fig. S14**).

3.3.2. Energetics of sotalol – hERG channel binding from enhanced sampling simulations

Our multi-microsecond long drug flooding simulations indicated that enhanced sampling MD runs of a drug entry into the channel pore through an intracellular gate are needed to obtain quantitative information about hERG – sotalol interactions. Therefore, we applied umbrella sampling MD (US-MD) [131], and Hamiltonian replica exchange umbrella sampling MD (HREUS-MD) [132] techniques to compute drug binding affinities and rates. Weak harmonic restraints were applied to hERG pore domain backbone atoms to preserve open hERG conformational state.

First, we investigated binding poses of different sotalol forms, corresponding to free energy minima from US-MD runs as shown in **Figure 3.3**. Both d- and l-sotalol occupy similar positions within the hERG pore (**Fig 3.3A**) and interact with the canonical binding residues

F656 and Y652 (see **Fig 3.3B**). Sotalol molecules along with interacting protein side chains, which are not restrained during the simulations, adopt different orientations and conformations (see **Fig 3.3B** and *Appendix A* **Figs. S15-S20**) to optimize those interactions. d- and l-sotalol(0) were bound slightly deeper into the pore than their cationic counterparts. Interestingly, all sotalol forms were found to bind just below a ring of Y652 residues interacting with them, as long as other S6 segment residues from multiple chains (see **Fig. 3B**) in general agreement with previous studies [150, 151]. Use of HREUS-MD methodology allowed us to facilitate sampling of multiple drug orientations and conformations in the hERG channel pore (*Appendix A* **Figs. S16-S20**).

US-MD and HREUS-MD simulations allowed us to estimate the free energies of drug binding, ΔG_{pore}, and to compute dissociation constants (K_D) [16, 127] of cationic and neutral d- or l-sotalol binding to the hERG channel in the open state (see *Table 3.1*, **Fig. 3.4** and *Appendix A* **Figs. S21-S22**), which shows good agreement between results obtained with US-MD and HREUS-MD methodologies. Our computed dissociation constants, K_D, indicate one to two orders of magnitude stronger binding of neutral d- or l-sotalol to open hERG channel compared to their cationic counterparts (**Table 3.1**) in agreement with our previous results for dofetilide and moxifloxacin [16]. Combined K_D values (taking into account neutral and cationic drug contributions at physiological pH=7.4) of about 2 mM are very similar for d- vs. l-sotalol, and also for US-MD and HREUS-MD simulations (**Table 3.1**). They are also in excellent agreement with racemic sotalol IC_{50} values for a non-inactivated hERG S620T mutant [133].

From hERG channel – sotalol US-MD simulations, we also computed position-dependent diffusion coefficient (D) profiles (see **Fig. 3.4C**), which are very similar for all the sotalol forms and indicate a steep ~70-fold drop in the drug diffusion as it enters the confinement of the hERG channel intra-cavitary space, as was also shown previously for dofetilide and moxifloxacin [16, 127] as well as sotalol – lipid membrane partitioning [126]. Using ΔG and D profiles, we computed ingress or "on" rates, k_{on}, which are very similar for d- and l-sotalol and somewhat smaller for cationic vs. neutral counterparts (see **Table 3.1**). Using computed K_D and k_{on} estimates we calculated their products corresponding to "off" or egress rates, k_{off}, similar for d- and l- stereoisomers and 1-2 order of magnitude smaller for sotalol(0) compared to sotalol(+) due to stronger binding of the former (**Table 3.1**). k_{on} and k_{off} MD estimates will be used as parameters for functional kinetic models described in Section 3.3.4.

3.3.3. Experimental validations of stereospecificity in sotalol binding to hERG channel

Sotalol is commercially only available as a racemic mixture of its hydrochloride salt. We separated the racemic mixture into the *S*- and *R*- isomers known as d- and l-sotalol, respectively, using quantitative chiral HPLC technique to obtain multi-milligram quantities of both enantiomers (see *Appendix A* **Fig. S1**), which were tested using whole-cell patch-clamp measurements with hERG channels stably expressed in HEK-293 cells at room temperature with continuous superfusion of drug-containing external solution. We observed comparable hERG current inhibition by 0.3 mM d- or l-sotalol application, both at depolarized potentials and upon hyperpolarization, indicating classical drug-induced channel blockade (**Fig. 3.5**, top panels). Fitting of concentration response curves (**Fig. 3.5**, bottom panels) revealed IC_{50} values of 0.286 ± 0.007 mM and of 0.288 ± 0.010 mM for d- and

l-sotalol, respectively. The Hill coefficients from these curves were 1.474 ± 0.051 for *d*-sotalol and 1.370 ± 0.010 for *l*-sotalol, respectively, suggesting cooperative interaction between more than one sotalol molecule to block hERG channel in agreement with flooding MD simulation data (Section 3.3.1 and **Fig. 3.2**). IC_{50} values also did not reveal any distinction in the ability of the two sotalol enantiomers to inhibit hERG current in good agreement with the results of enhanced sampling MD simulations reported above (Table 3.1). They are more favorable than MD K_d values of 1.5 to 2.3 mM, but the latter were computed for an open state hERG model, whereas in patch-clamp measurements using a voltage protocol in **Fig. 3.5**, the channel is mostly in the inactivated state, and sotalol binding is stabilized by channel inactivation [128]. Our experimental and MD data are in agreement with an electrophysiology study of hERG channel interaction with racemic sotalol, where the IC_{50} for wild-type hERG and S620T hERG mutant with abolished inactivation are 0.516±0.036 mM and 2.22±0.38 mM, respectively [133]. This suggests that our US-MD derived kinetic parameters (Table 3.1 and Section 3.3.2) are robust enough to be used for functional scale modeling.

3.3.4. Functional scale modeling of sotalol – hERG channel interactions and their effect on cardiac rhythm

To develop a functional kinetic model of sotalol – hERG channel interactions, we used the multiscale strategy we recently reported [16]. We used a drug-free hERG Markov model [16] and incorporated open and inactivated hERG channel – drug interactions via corresponding neutral and cationic drug "on" (k_{x_d} and k_{xd}) and "off" (r_{x_d} and r_{xd}) transition rates, where *x* = o or i for open and inactivated state, respectively (see *Appendix A* **Fig. S2**). We used US- MD

computed drug "on" and "off" rates (**Table 3.1**) as our open-state hERG – sotalol(0) and sotalol(+) model estimates (k_{o_d}, k_{od}, r_{o_d} and r_{od} in *Appendix A* **Fig. S2** and **Tables S2-S3**).

Since we lacked a structural atomistic model of inactivated hERG channel we relied on literature data for relative sotalol affinities for open versus inactivated states with experimental estimates indicating more potent inhibition for the latter [128, 133]. We first used the reported 4.3-fold ratio of sotalol IC_{50} values for a non-inactivated S620T mutant to WT hERG channel from experiments in Chinese hamster ovary (CHO) cells at room temperature [133] as K_{Do} / K_{Di} in our Model 1 (solid light-blue and dotted black curves in **Fig. 3.6A**) to optimize "on" rates, which provided excellent fit to experimental hERG inhibition data from this study (blue circles in **Fig. 3.6A**). Notably, however, there is very little hERG inhibition for physiologically relevant drug concentrations from 1.4 to 14.7 μM [105, 152] (black box in **Fig. 3.6A)**: up to ~2% for this model.

To investigate the effect of the hERG channel – sotalol interactions on cardiac electrophysiology, we included hERG – sotalol model 1 (by swapping the drug-free I_{Kr} model) into the O'Hara-Rudy human ventricular cardiomyocyte model [135]. We simulated the effect of sotalol on the pseudo-ECGs computed from a 1D strand of O'Hara-Rudy ventricular myocytes and calculated the QT interval [16]. We observed negligible prolongation of the QT interval with model 1 when considering hERG channel block alone by the sotalol racemic mixture (d- and l-sotalol in a 1:1 ratio) as shown in **Fig. 3.6B**. In QT prolongation traces shown in **Fig. 3.6C** we simulated the sympathetic stimulation of 1D ventricular myocyte strand via the additive impact of 1 μM of potent beta-adrenergic agonist isoproterenol (ISO)

and its stereoselective inhibition by sotalol [107-111]. l-Sotalol has a strong beta-blocking activity with K_i = 650 ng/ml vs. 38,000 ng/mol for d-sotalol [109]. Beta adrenergic stimulation did not notably increase the QT prolongation for model 1 (see *Appendix A* **Fig. S4A&C** for d- and l-sotalol, respectively). Simulating the stereospecific effect of beta-blockade in addition to hERG inhibition effect by racemic dl-sotalol, model 1 increases (due to l-sotalol, *Appendix A* **Fig. S4C**) but still significantly underestimated QT prolongation compared to clinically reported QT data [136]: compare blue and black curves in **Fig. 3.6C.**

When the functional model of hERG channel – sotalol interactions was optimized to data from expressed hERG channels *in vitro* to determine the relative strength of inactivated state block (as shown for model 1 above), we were unable to predict the clinical features of hERG channel block by sotalol. Therefore, we set out to make predictions about what relative affinities of sotalol to the open and inactivated state would allow reproduction of the clinical data. Because the open state affinity is determined by the MD simulations, we performed a "top down" model optimization to predict the inactivated state affinity of sotalol to hERG channel. In other words, we worked backward from the clinically reported effect of sotalol on the QT interval in humans to determine the inactivated state affinity since all the other parameters in the model are constrained by specific measurements or simulations.

The results of the top-down model optimization (model 2) are shown in **Fig. 3.7**. The model shown in **Fig. 3.7A** for d- and l-sotalol (solid red and dotted black curves, respectively) was identified as best able to reproduce the effect of sotalol on the QT interval. The model predicted that, consistent with some other hERG channel blockers such as dofetilide [133],

the relative affinity of sotalol to the hERG inactivated state should be > 50-fold the affinity to the hERG open state. We found that a 63-fold open to inactivated state affinity ratio yielded computed IC_{50} values of 20 μM during a voltage clamp protocol consistent with reference guinea pig ventricular myocyte hERG inhibition data [134] used for fitting this model. This functional kinetic hERG – sotalol interaction model 2 resulted in up to ~40% hERG inhibition for physiologically relevant d- and l-sotalol concentrations from 1.4 to 14.7 μM [105, 152] as shown in **Fig. 3.7A**.

In **Fig. 3.7B** we showed that our predicted model 2 effects of dose-dependent racemic dl-sotalol induced hERG channel inhibition alone in a 1D strand of ventricular myocytes (red curve) underestimates clinical QT prolongation data [136] (black curve)**.** However, after including the combined stereospecific beta-blocking effect of sotalol (dominated by l-sotalol as shown in *Appendix A* **Fig. S4D**) in addition to hERG inhibition effects by racemic dl-sotalol, we were able to reproduce clinical QT interval prolongation [136] by model 2 (compare black and red curves in **Fig. 3.7C**). Notably, using a 4.3 ratio for hERG open to inactivated state affinities as in model 1 resulted in worse fit to reference hERG inhibition data [134] and smaller QT prolongation compared to clinical data [136] as shown in *Appendix A* **Fig. S5**.

Thus, we observed that model 2 accurately predicts clinical QT prolongation by dl-sotalol if we take into account hERG block, beta-adrenergic stimulation and stereospecific beta-blockade. We tested a range of drug concentration effects as a function of time to predict arrhythmogenic impacts of d-, l- and dl-sotalol using model 2 as shown in **Fig. 3.8.** We observed that upon beta-adrenergic stimulation, hERG block alone (**Fig. 3.8A-C**, top rows)

leads to appearance of early afterdepolarizations (EADs) on pseudo-ECGs (left panels for each condition) and variable effects on the cardiac rhythms in time (right panels for each condition indicate the peak positions of R and T waves). Upon beta-blockade pro-arrhythmia markers emerged for d-sotalol at all concentrations similar to the setting of hERG block alone (**Fig. 3.8A,** top two rows). For l-sotalol (**Fig. 3.8B**, middle rows) and the dl-sotalol racemic mixture (**Fig. 3.8C**, bottom rows), a different story emerged: In the setting of hERG block alone, arrhythmogenic patterns emerged for all drug concentrations tested, but when both hERG block and βAR blockade effects were simulated, the computed cardiac rhythms fully normalized. These tests were extended to a wide range of l-sotalol concentrations from 200 to 2400 ng/ml resulting in the same outcome (data not shown). These predictions suggest that a more potent beta-adrenergic blockade by l-sotalol may serve as the key plausible mechanism to reduced arrhythmogenicity with l-sotalol alone and for the racemic mixture.

3.4. Discussion

3.4.1. A crucial link between sotalol stereochemistry and its arrhythmogenicity

Computational modeling and simulation approaches at various length and time scales have demonstrated usefulness to make predictions, suggest new experiments, and to reconcile seemingly disparate existing data [124, 125, 153, 154]. In this study, multi-scale modeling and simulation approaches [16, 122, 155-157] allowed us to specifically ask questions about the importance of isomerism in determining fundamental mechanisms of arrhythmia proclivity induced by d- sotalol, l-sotalol and the dl-sotalol racemic mixture [107, 110, 111, 158-161]. One benefit of computational modeling and simulation is the ease of performing component dissection to determine which attributes of a system yield emergent impacts

[122, 155]. Here, we show clearly in MD simulations, which were validated by experimental data, that d- sotalol and l-sotalol have similar affinity and interaction with the hERG channel (see **Table 3.1** and **Figures 3.3 – 3.5**), in contrast to observed or proposed stereospecific binding of some other hERG-blocking chiral drugs [78] such as methadone [80], quinidine vs. quinone [82], bupivacaine and ropivacaine [86, 87]. Similar stereoisomer hERG channel affinities were previously reported for verapamil [162] and chromanol 293B [163]. Our findings are also in line with a previous experimental observation of similar effects of d-,l- and racemic dl-sotalol on action potential and time-dependent potassium current in isolated cardiac muscle and Purkinje fibers from animal models in the absence of catecholamines [107, 164]. Therefore, we conclude that stereo-specificity of drug-induced cardiotoxicity attributed to d-sotalol is unlikely to result from differential binding affinities of sotalol stereoisomers to hERG channel. However, the comprehensive multiscale modeling approach [16] allowed us to go a step further and ask if the stronger beta blocking effect of l-sotalol [107-109, 111, 164-166] was necessary and sufficient to account for a reduction in pro-arrhythmic risk.

3.4.2. How to resolve disconnect between clinical and experimental data

One of the longstanding conundrums related to hERG block by sotalol is that relatively high concentration of drug required to block the channel when assessed in isolated cloned channels expressed *in vitro* compared to the relatively low plasma concentrations reported in humans that apparently result in substantial QT interval prolongation [105, 136, 167]. Human plasma concentrations from patients on sotalol are consistently reported in the 1.4 – 14.7 μM (500 – 4000 ng/mL) range [105, 152]. Even smaller, 0.5 μM sotalol plasma

concentration, results in a 50% likelihood of ≥10ms increase in human QT interval [167]. This is in contrast to concentrations reported from *in vitro* measurements that suggest up to 100-fold higher sotalol concentrations required for substantial channel inhibition, although the range of experimentally reported IC_{50} values is variable [105, 133, 134, 167-175].

We attempted to better understand this disconnect by building computational models that were optimized to experimental cell line data from our laboratory and were similar to previous studies (IC_{50} values of ~290 μM from this work, 586±179 μM and 4.3-fold inactivated to open state inhibition from [133], 210-450 μM from [170], 103 μM from [167], etc.). Consistent with earlier reports [167, 176, 177] , we also noted that models built on data from expressed channel – drug interactions [133] did not yield clinically observed prolongation of the QT interval [136]. However, when we performed a top-down model optimization, working backward from the clinically reported effects of sotalol on QT interval we found an IC_{50} value ~ 20 μM, which reflected ~ 63-fold higher affinity for inactive to open state. Interestingly, these values are similar to sotalol inhibition data of the reported low- and high-affinity dofetilide binding sites in guinea pig ventricular myocytes [134], although in the study eporting those binding assays, the authors interpret the low affinity site as non-specific binding, not necessarily related to hERG channel current inhibition [134, 178]. Additional studies may be needed to provide further clarification.

There is no question that collecting data in the future from a physiologically relevant system with all of the interacting components like the guinea pig ventricular myocyte [134], is likely to yield more reliable data for model optimization. Nevertheless, we were able to use a top-

down model approach to constrain model parameters and predict QT interval prolongation as a function of drug concentration that was an excellent agreement with clinically reported data [136] (see **Figure 3.7**). These results may suggest the critical importance of making drug affinity assessments in a physiologically relevant environment as the differences between the clinical dose and resulting effects cannot currently be reconciled with the dose response curves from expressed channels. Indeed, one possibility is that the induced pluripotent stem cell-derived cardiomyocyte (iPSC-CM) based drug screening technology may create new capacity and potential to do just that [179-181].

3.4.3. Limitations and future directions

In this study we were able to predict sotalol induced QT interval prolongation om the ECG and its stereospecific pro-arrhythmia proclivities with our functional hERG – sotalol models optimized using "on" and "off" drug rates for the open-state hERG channel. Since we lacked a structural atomistic hERG channel model in the inactivated state, we had to use a top-down approach to predict an optimal ratio of sotalol affinities to open and inactivated hERG channels, which turned out to correspond to a ratio of sotalol IC_{50} values for low and high affinity dofetilide binding sites in ventricular cardiomyocytes [134]. Yet, the low-affinity binding site in the Duff et al study was interpreted as non-specific binding rather than hERG channel inhibition [134, 178]. Such drug binding to other proteins or a lipid membrane itself will alter its effective intracellular concentration, availability for hERG channel inhibition and thus pro-arrhythmia proclivities, which can be investigated in future work. As an alternative, we also tested a ratio of sotalol IC_{50} values for wild-type and non-inactivated S620T mutant channels from cultured cells [133], with the latter agreeing well with our US-

MD K_d estimates. Functional models optimized using these data provided good fit to our experimental WT hERG inhibition dose response curves but failed to capture dose-dependent clinical QT prolongation [136] in line with previous reports suggesting a significant gaps between drug doses required to cause *in vitro* hERG channel inhibition and QT prolongation observed *in vivo* [167].

Such discrepancies can be related to multiple factors not explicitly considered here. For instance, hERG channel isoforms, 1a and 1b, with the same transmembrane but different intracellular domain composition contribute to physiological I_{Kr} and have distinct gating kinetics [182], which may modulate drug effect on cardiac electrophysiology. Moreover, mutations in auxiliary hERG binding protein MiRP1 were found to affect drug-induced arrhythmogenicity also due to altered channel gating kinetics [118, 183], although WT MiRP1 binding was shown not to affect sotalol hERG channel block [128]. Also, not only hERG channel – drug interaction, but also ventricular myocyte model may have an effect on predicted drug-induced QT prolongation and arrhythmogenicity as was tested and/or discussed previously [184-187]. Here and in previous studies [16, 118, 186, 187] the O'Hara-Rudy human ventricular cardiac myocyte model [135] was used providing good agreement with clinical QT prolongation data [136] for our myocyte-based model, whereas comparison with other widely used models such as Grandi – Bers [188] and ten Tusscher – Panfilov [189] models will be performed in subsequent work.

In this study, MD simulations used an available cryo-EM hERG channel structure [26], which we demonstrated to be in the open conducting state [16, 73, 127]. However, many hERG

blocking drugs including sotalol are suggested to have a higher affinity for the inactivated channel state [27, 128, 133]. Structural information about potential hERG channel inactivated state just started to emerge from recent cryo-EM [72] and MD simulation [74] studies, but was not yet available for our present work. Interestingly, however, our multi-microsecond long unbiased drug flooding simulations resulted in a hERG channel structure with a distorted selectivity filter (SF), pinched in the middle (in 3 out of 4 simulations) and significantly widened at the top, in line with some findings from those new studies [72, 74]. A similar SF conformation was also shown to be non-conducting in our previous hERG channel simulations [127] and may potentially represent a transition to the inactivated state of the channel bearing some similarity to C-type inactivated KcsA [190, 191] and Shaker family [192, 193] channel structures, although there might be multiple structural mechanisms of K^+ channel inactivation [193]. Inactivating conformational transition may also explain stable sotalol binding poses, located deep inside the pore in some unrestrained drug flooding MD but not in any restrained US-MD runs, in line with previously suggested sotalol binding to open state and subsequent stabilization by hERG channel inactivation [128] .

Finally, we found that beta-blocking properties of sotalol enantiomers are crucial for their pro-arrhythmia proclivities. Yet, in this study we did not explicitly study sotalol binding to beta-adrenergic receptors via MD simulations due to a complexity of this problem, requiring a separate study currently underway in our laboratory using recent human β_1 adrenergic receptor (β_1AR) structures [194] and state-specific functional models of sotalol – receptor

interactions [195], which will allow for a comprehensive exploration of sotalol QT modulation effect at different BCL (RR interval) values [136].

.

3.5. Conclusions

Cardiotoxicity in the form of cardiac arrhythmia is a major reason for multiple drug withdrawals from the market. Such drug-induced arrhythmogenicity has been largely attributed to a blockade of hERG K^+ channels, which repolarize cardiac myocytes. However, not all hERG-blocking drugs cause deadly arrhythmias. In the case of the anti-arrhythmic beta-blocker sotalol, a subtle change in drug chemistry due to stereoisomerism leads to different pro-arrhythmia outcomes. In this study, we investigated and predicted molecular determinants of stereospecific d- and l-sotalol pro-arrhythmia proclivities through a combination of atomistic molecular dynamics (MD) simulations with electrophysiological recordings as well as experiment- and MD-informed multi-scale modeling of cardiac electrophysiology at cell and tissue levels. MD simulations predicted that up to 2 sotalol molecules can bind in the hERG channel pore, demonstrated stronger binding of neutral drug forms as well as similar d- and l-sotalol binding poses and affinities for the open channel pore. These predictions are in good agreement with electrophysiology recordings of hERG channel inhibition in HEK cells by both sotalol enantiomers. MD simulation computed "on" and "off" rates for open hERG – sotalol interactions were used as parameters for functional kinetic models, which were optimized to reproduce hERG inhibition dose response curves using cultured cells from this work or cardiomyocyte data from a previous study. We also explored different estimates of sotalol affinities for open and inactivated hERG conformational states using a top-down approach. Optimized models were incorporated into

standard ventricular cardiomyocyte cell and tissue simulations to predict dose-dependent d- and l-sotalol effect on heart rhythm. The model based on cardiomyocyte hERG inhibition data was able to predict clinically observed sotalol induced QT prolongation when taking into account both hERG channel and beta-adrenergic receptor inhibition, whereas the model based on a less potent sotalol effect on the hERG channel in cultured cells significantly underestimated clinical QT interval lengthening. The former model also correctly predicted higher pro-arrhythmia risk of d-sotalol compared to l-sotalol and racemic mixture attributing this to stereospecific beta-blocking properties, ameliorating the arrhythmogenic hERG channel inhibition effect.

Disclosures

None. The authors declare no competing interest.

Acknowledgments

The work in C.E.C., I.V., H.W., J.T.S., V.Y.Y., and S.Y.N. groups were supported by NIH NHLBI grants 5R01HL128537, 5U01HL126273, NIH Common Fund 1OT2OD026580-01 and 3OT2OD026580-01 (C.E.C. and I.V.). Support was also provided by the following: American Heart Association Predoctoral Fellowship 16PRE27260295 (K.R.D.) and Career Development Award 19CDA34770101 (I.V.), NIH NHLBI grants 1R01HL152681 (C.E.C. and I.V.) and R01HL128537 (S.Y.N.), Canadian Institutes of Health Research Project Program grant Funding Reference Number 156236 (S.Y.N.), Department of Physiology and Membrane Biology Research Partnership Fund (I.V. and C.E.C.), Extreme Science and Engineering Discovery Environment (XSEDE) Grant MCB170095 (I.V., C.E.C., K.R.D.), National Center for

Supercomputing Applications (NCSA) Blue Waters Broadening Participation Allocation (C.E.C., I.V., K.R.D.), Texas Advanced Computing Center (TACC) Leadership Resource Allocation MCB20010 (I.V., C.E.C., K.R.D.), Oracle cloud for research allocation (I.V., C.E.C.), Pittsburgh Supercomputing Center (PSC) Anton 2 allocations PSCA17085P, PSCA16108P, PSCA18077P, MCB160089P, and PSCA17021P (I.V., C.E.C., K.R.D., S.Y.N.). Anton 2 computer time was provided by the PSC through Grant R01GM116961 from the National Institutes of Health. The Anton 2 machine at PSC was generously made available by D.E. Shaw Research.

Appendix A. Supplementary Materials

Supplementary material 1 contains detailed methodology description, Tables S1-S3, Figures S1-S22 and references. It can be also obtained using the following URL:

https://ars.els-cdn.com/content/image/1-s2.0-S0022282821001097-mmc1.pdf

Appendix B. Data Supplement

Supplementary material 2: Data supplement contains high-performance liquid chromatography (HPLC), nuclear magnetic resonance (NMR), high-resolution mass spectrometry **(**HRMS) spectra and X-ray crystallography data. It can be also obtained using the following URL:

https://ars.els-cdn.com/content/image/1-s2.0-S0022282821001097-mmc2.pdf

Table 3.1. Open hERG pore sotalol binding data from US-MS and HREUS-MD simulations. Molecular dynamics (MD) computed drug binding free energies (ΔG_{bind}), dissociation constants (K_D) and diffusion coefficients at the drug binding site ($\mathcal{D}_{pore}$) as well as drug "on" (k_{on}) and "off" (k_{off}) rates used for parameterizing functional scale models. Data are means ± standard error of means (SEM) for 10-ns or 20-ns US-MD and HREUS-MD simulation blocks.

		ΔG_{bind} (kcal mol^{-1})	K_D (mM)	D_{pore} (10^{-6} cm^2 s^{-1})	k_{on} (μM^{-1}s^{-1})	k_{off} (s^{-1})
d-Sotalol(0)	**US-MD**	-5.34 ± 0.74	0.17 ± 0.21	0.13 ± 0.02	$7.4 \cdot 10^2$	$1.3 \cdot 10^5$
	HREUS-MD	*-5.03 ± 0.52*	*0.28 ± 0.24*			
d-Sotalol(+)	**US-MD**	-2.32 ± 0.07	23.3 ± 2.6	0.12 ± 0.02	$3.6 \cdot 10^2$	$8.3 \cdot 10^6$
	HREUS-MD	*-2.44 ± 0.33*	*19 ± 10*			
d-Sotalol (pH=7.4)			**2.3** ***(1.5)***			
l-Sotalol (0)	**US-MD**	-4.57 ± 0.51	0.60 ± 0.49	0.16 ± 0.02	$7.9 \cdot 10^2$	$4.7 \cdot 10^5$
	HREUS-MD	*-5.08 ± 0.24*	*0.26 ± 0.10*			
l-Sotalol (+)	**US-MD**	-3.60 ± 0.21	2.9 ± 1.0	0.17 ± 0.05	$4.4 \cdot 10^2$	$1.3 \cdot 10^6$
	HREUS-MD	*-2.80 ± 0.08*	*10.5 ± 1.4*			
l-Sotalol (pH=7.4)			**2.0** ***(2.0)***			

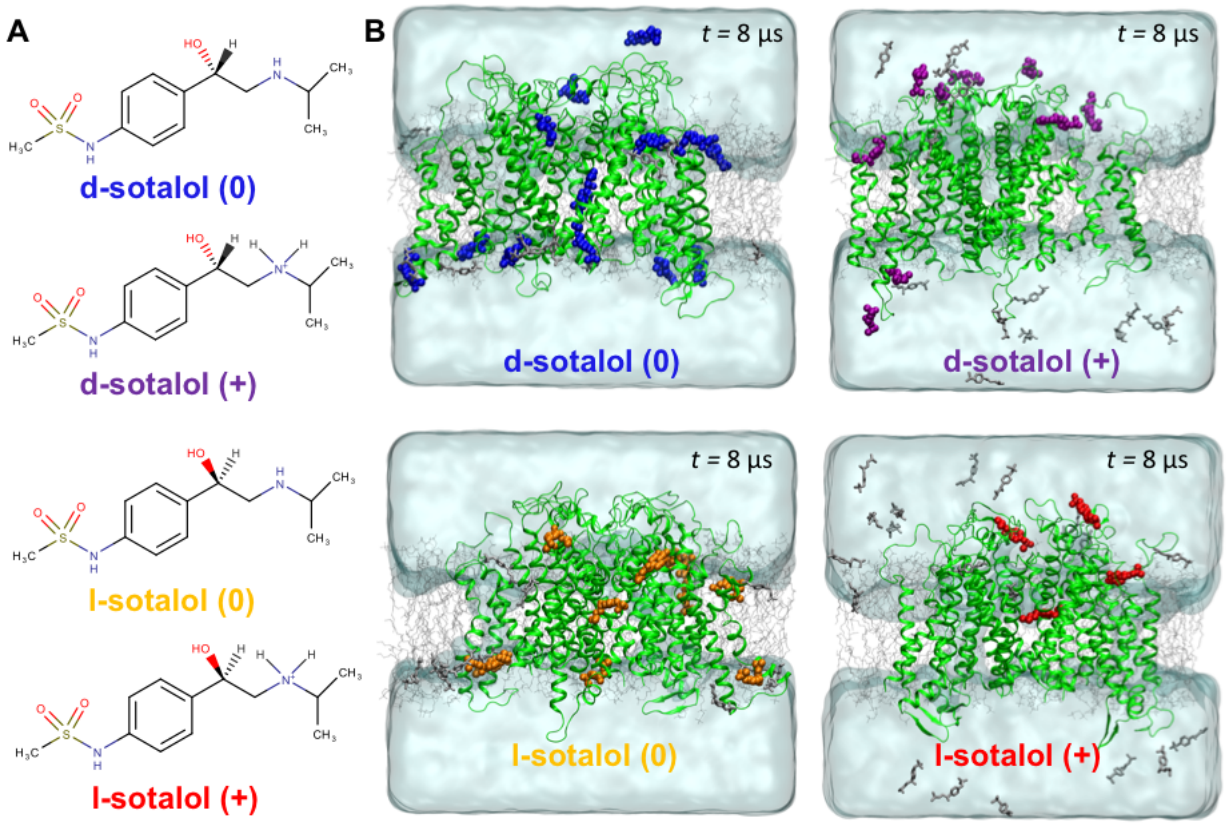

Figure 3.1. Distribution of cationic (+) or neutral (0) d- or l-sotalol around the hERG channel from multi-µs long unbiased MD simulations. (A) Chemical structures of neutral (0) and cationic (+) forms of d- and l-sotalol **(B)** Snapshots of the molecular systems consisting of the hERG channel embedded in the POPC bilayer, solvated with aqueous 150 mM KCl and initial 50 mM sotalol solution , at the end of 8.1 µs MD simulations. For sotalol molecules within 3.5 Å of hERG protein residues non-hydrogen atoms are shown in the colored space filling representation, non-interacting sotalol molecules are shown as grey sticks. The hERG channel is shown as green ribbons, POPC lipid tails as thin gray sticks, water as aquamarine surface, K^+ and Cl^- ions are not shown for clarity.

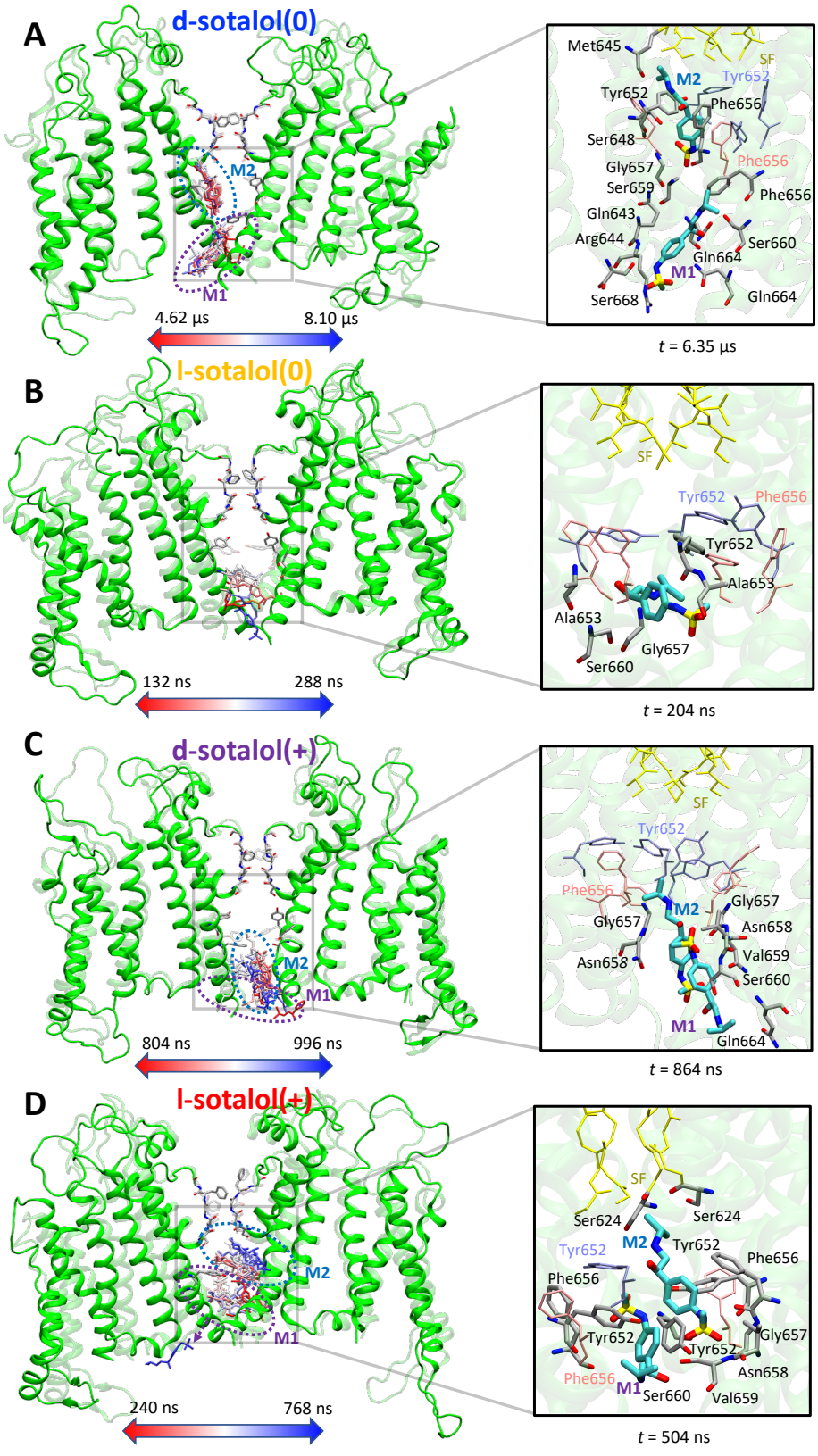
A
d-sotalol(0)
M2
M1
4.62 µs
8.10 µs
Met645
SF
M2
Tyr652
Tyr652
Phe656
Ser648
Gly657
Phe656
Ser659
Phe656
Gln643
Arg644
Ser660
Gln664
M1
Ser668
Gln664
t = 6.35 µs
B
l-sotalol(0)
132 ns
288 ns
SF
Tyr652
Phe656
Tyr652
Ala653
Ala653
Gly657
Ser660
t = 204 ns
C
d-sotalol(+)
M2
M1
804 ns
996 ns
SF
Tyr652
Phe656
Gly657
M2
Gly657
Asn658
Asn658
Val659
Ser660
M1
Gln664
t = 864 ns
D
l-sotalol(+)
M2
M1
240 ns
768 ns
SF
Ser624
Ser624
M2
Tyr652
Tyr652
Phe656
Phe656
Tyr652
Gly657
Tyr652
Asn658
Phe656
M1
Ser660
Val659
t = 504 ns

Figure 3.2.

<u>Figure 3.2.</u> Binding sites of neutral (0) or cationic (+) d- or l-sotalol around the hERG channel 8.1 μs long unbiased MD simulations. (A) d-sotalol(0); **(B)** l-sotalol(0); **(C)** d-sotalol(+); **(D)** l-sotalol(+). *Left panels:* Time-series rendering for binding of one or two sotalol molecules (labeled M1 and M2) within the hERG pore. Sotalol molecules in the frames are shown by colored sticks from the beginning (red) to the end (blue) of each representative binding event. The hERG channel is shown in the initial (transparent green ribbons) and the final (solid green ribbons) conformations. Canonical drug interacting residues Phe656 and Tyr652 as well as selectivity filter (SF) residues are shown as solid or transparent atom-colored ribbons (C – gray, O – red, N – blue)**.** *Right panels:* Representative binding poses adopted by sotalol molecules (thick atom-colored sticks with C – cyan, S – yellow, others as above) in the hERG channel pore. Interacting hERG residues (within 3.5 Å of any non-H atoms of the drug) are shown as thick atom-colored sticks (C – gray, others are as above). Non-interacting hERG residues Phe656, Tyr652 as well as its SF residues are shown as thin pink, blue and yellow sticks. Hydrogen atoms are not shown for clarity.

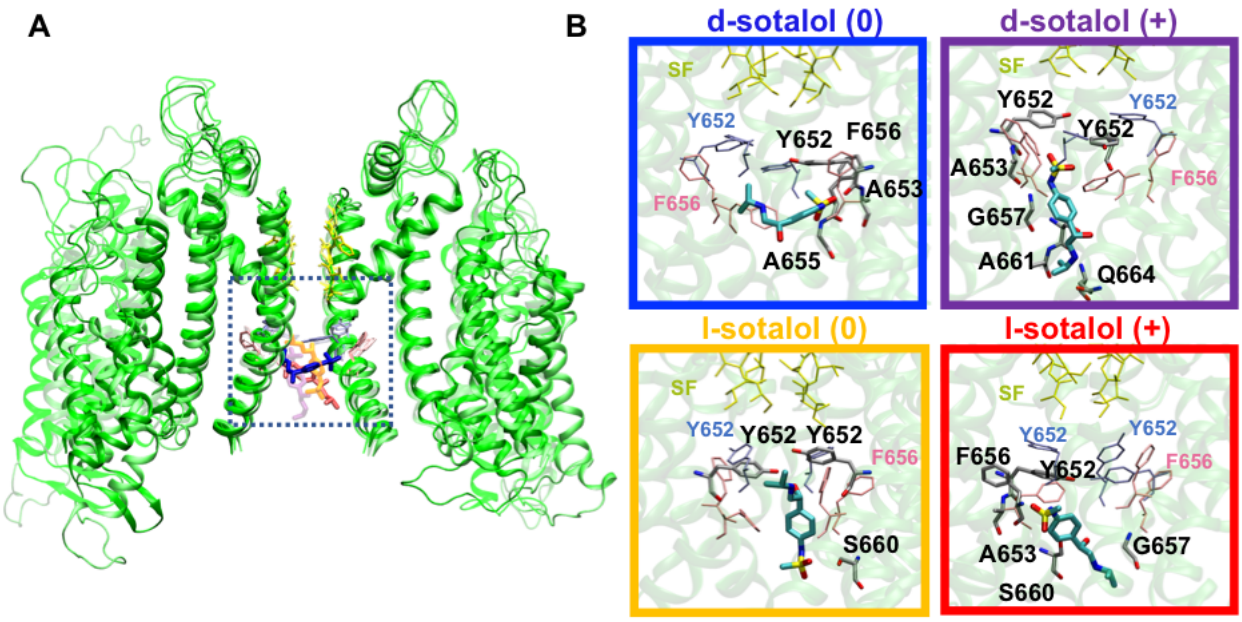

Figure 3.3. Representative binding poses of neutral (0) and cationic (+) d- and l-sotalol to open hERG channel obtained from US-MD simulations. (A) hERG channel – bound sotalol structures from four US-MD runs corresponding to free energy minima for each simulation are superimposed and represented by different shades. Two opposite chains of the open-state hERG channel structures are shown as green ribbons. Bound sotalol molecules are shown as thick colored sticks: d-sotalol(0) – blue, d-sotalol(+) – purple, l-sotalol(0) – orange, and l-sotalol (+) – red . hERG SF residues are shown as yellow thin sticks, and canonical binding residues F656 and Y652 as thin pink and ice-blue sticks. **(B)** Close-up views of sotalol hERG binding poses corresponding to a dashed box location in **panel A**. Sotalol molecules are shown as thick atom-colored sticks (C – cyan, N – blue, O – red, S – yellow). hERG channel is shown by transparent green ribbons with residues within 3.5 Å of sotalol non-hydrogen atoms shown by thin atom-colored sticks (C – gray, N – blue, O – red). Non-interacting SF, F656 and Y652 residues are shown by thin colored sticks as in panel A. Hydrogen atoms are not shown for clarity. Box border coloration in **panel B** corresponds to coloration of each isoform of d- and l-sotalol in **panel A.**

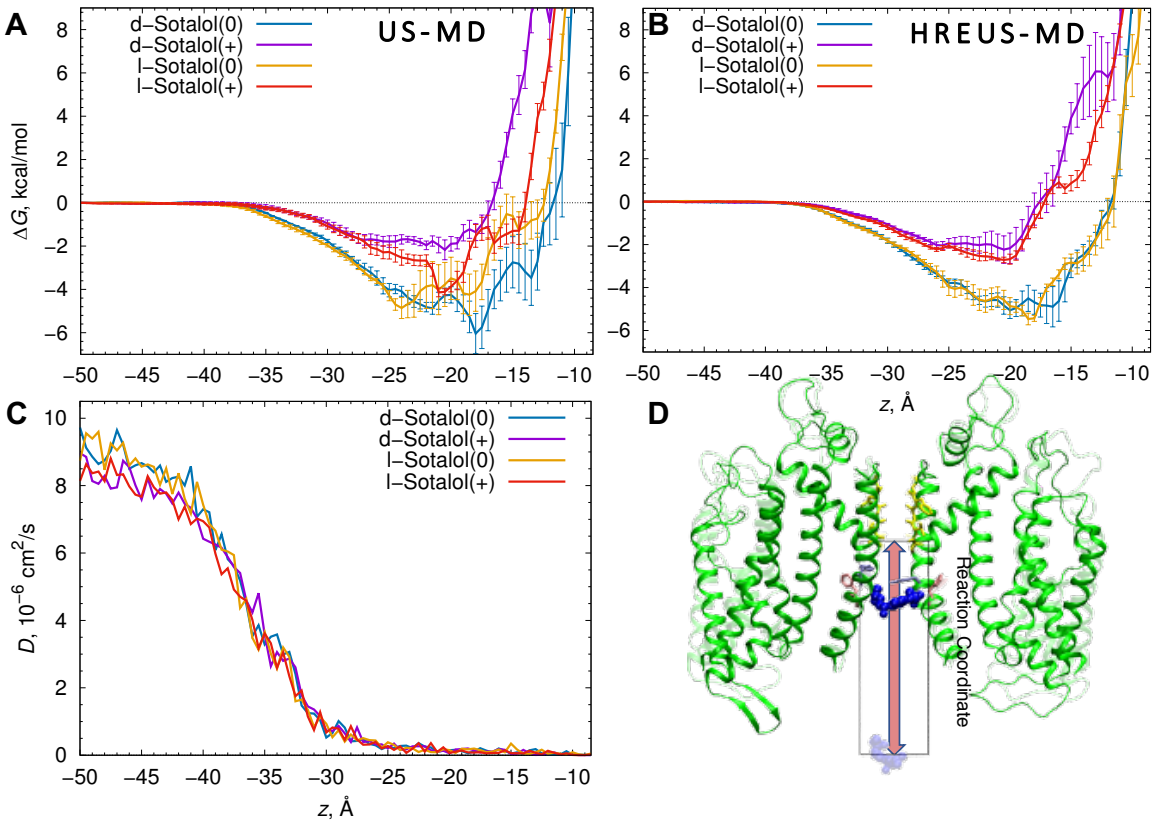

Figure 3.4. Thermodynamics and kinetics of d- and l-sotalol binding to the open hERG pore from US-MD simulations. Free energy, ΔG, profiles **(A)** and corresponding diffusion coefficient, D, profiles **(C)** computed from US-MD simulations**,** and **(B)** free energy, ΔG, profiles alternatively computed from HREUS-MD simulations for d-sotalol (0) (blue), d-sotalol (+) (purple), l-sotalol (0) orange, and l-sotalol (+) (red). Error bars are computed from block averaging and represent standard errors of mean. **(D)** Molecular snapshots of d-sotalol(0) simulated systems with two opposite chains of the open hERG channel shown as green ribbons, selectivity filter residues shown as yellow sticks, and sotalol molecule shown in blue space-filling representation at the pore binding site (opaque) or in the bulk aqueous solution (transparent). The reaction coordinate for these simulations is the z-coordinate with respect to the SF backbone C_α center of mass, leading from the intracellular bulk aqueous solution (z=– 50 Å) to the bottom of the selectivity filter (z=–5.5 Å), shown as an arrow and a bounding box with a 20 Å width corresponding to a diameter of the flat-bottom restraint in the xy-plane.

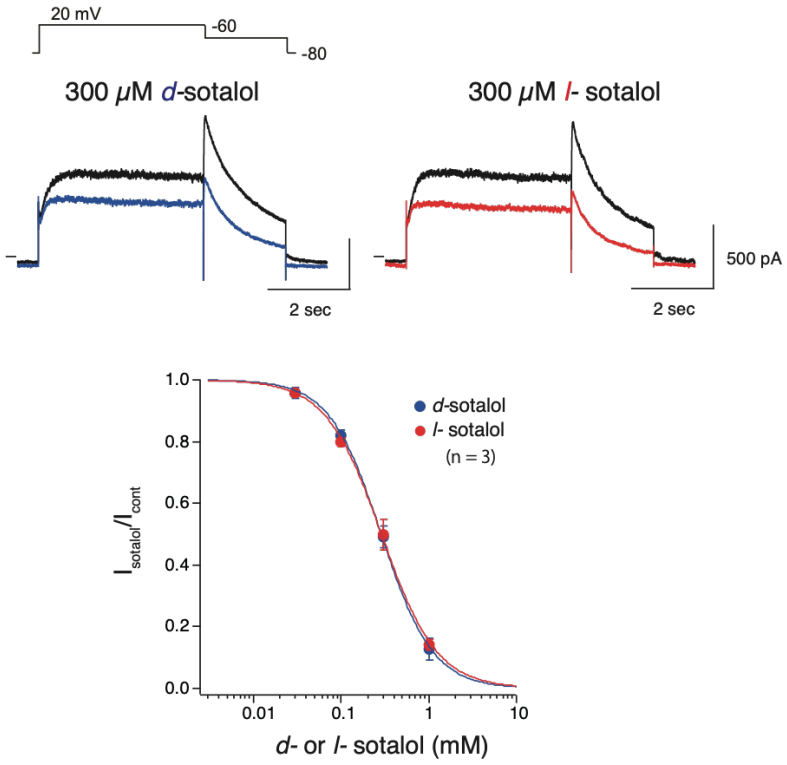

Figure 3.5. d- and l-Sotalol concentration-response from patch clamp electrophysiology experiments. (Upper panels) Whole-cell currents from HEK-293 cells expressing hERG channels in response to voltage-clamp pulses from −80 mV to +20 mV and then to −60 mV to record pulse-current and tail currents, respectively. Black lines indicate the control currents and blue as well as red lines indicate the decreased currents in the presence of 300 μM of d- or l-sotalol, respectively. **(Bottom panel)** Concentration-response for block of hERG channels by d- (blue) or l-sotalol (red). Drug effects on tail current peak amplitude are plotted. Data are means ± standard error of means (SEM) from 3 cells each for d- or l-sotalol. Blue and red curves represent the fitted Hill equation.

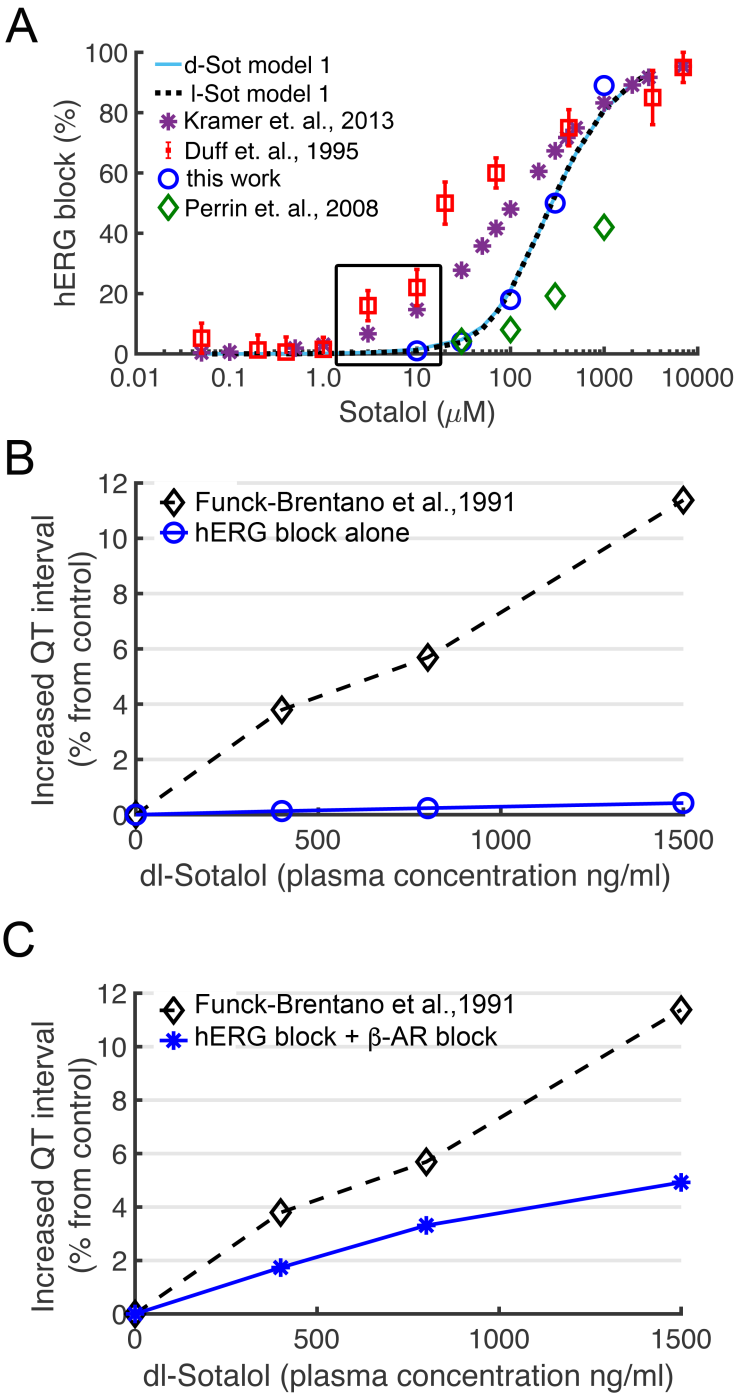
A
d-Sot model 1
l-Sot model 1
Kramer et. al., 2013
Duff et. al., 1995
this work
Perrin et. al., 2008
hERG block (%)
Sotalol (μM)
B
Funck-Brentano et al.,1991
hERG block alone
Increased QT interval (% from control)
dl-Sotalol (plasma concentration ng/ml)
C
Funck-Brentano et al.,1991
hERG block + β-AR block
Increased QT interval (% from control)
dl-Sotalol (plasma concentration ng/ml)

Figure 3.6.

Figure 3.6. Concentration dependent block of hERG and QT prolongation by sotalol. **(A)** Experimentally measured dose dependent inhibition of hERG channel by sotalol (colored symbols) and model 1 optimization based on experiments by us and others from expressed channels in mammalian cell lines for d-sotalol (solid light-blue line) and for l-sotalol (dashed black line). Black boxes indicate therapeutic plasma concentrations. Experimental data are from: Kramer 2013 – ref. [169]; Duff 1995 – ref. [134]; Perrin 2008 – ref. [133]; and this work – see ***Fig. 3.5***. **(B)** Concentration dependent increase in QT intervals by d,l-sotalol with hERG channel block alone (blue circles) compared to clinical data (black diamonds) from ref. [136]. **(C)** During sympathetic stimulation via concurrent ISO 1μM application, simulations showed a concentration dependent increase in QT interval by d,l-sotalol dependent hERG block and βAR blockade (blue asterisks) compared to clinical data from ref. [136] (black diamonds).

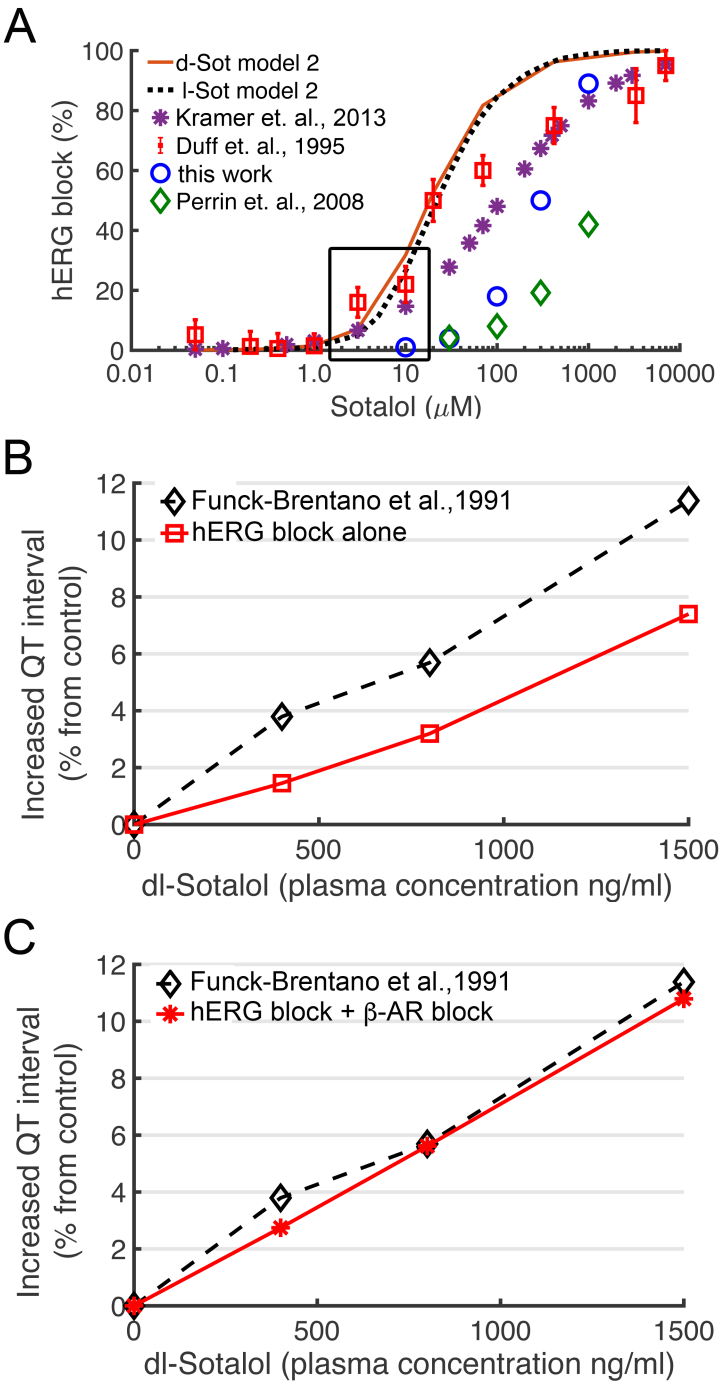
A
d-Sot model 2
l-Sot model 2
Kramer et. al., 2013
Duff et. al., 1995
this work
Perrin et. al., 2008
hERG block (%)
Sotalol (μM)
B
Funck-Brentano et al.,1991
hERG block alone
Increased QT interval (% from control)
dl-Sotalol (plasma concentration ng/ml)
C
Funck-Brentano et al.,1991
hERG block + β-AR block
Increased QT interval (% from control)
dl-Sotalol (plasma concentration ng/ml)

Figure 3.7.

Figure 3.7. Validation of computational drug screening with human clinical data.
Experimentally measured dose dependent inhibition of hERG by sotalol (colored symbols) and model 2 optimization for d-sotalol (solid red line) and for l-sotalol (dashed black line). using data from ref. [134]. Experimental data are from: Kramer 2013 – ref. [169]; Duff 1995 – ref. [134]; Perrin et al, 2008 – ref. [133]; and this work – see Fig. 5. **(B)** Concentration dependent increase in QT intervals by d,l-sotalol with hERG channel block alone (red cicrles) compared to clinical data (black diamonds) from ref. [136]. **(C)** During concurrent ISO 1μM application to model sympathetic stimulation, simulations showed a concentration dependent increase in QT interval by d,l-sotalol dependent hERG block and βAR blockade (red asterisks). Accounting for the effect of β-AR blockade, the model 2 predictions compared well to clinical data from ref. [136] (black diamonds).

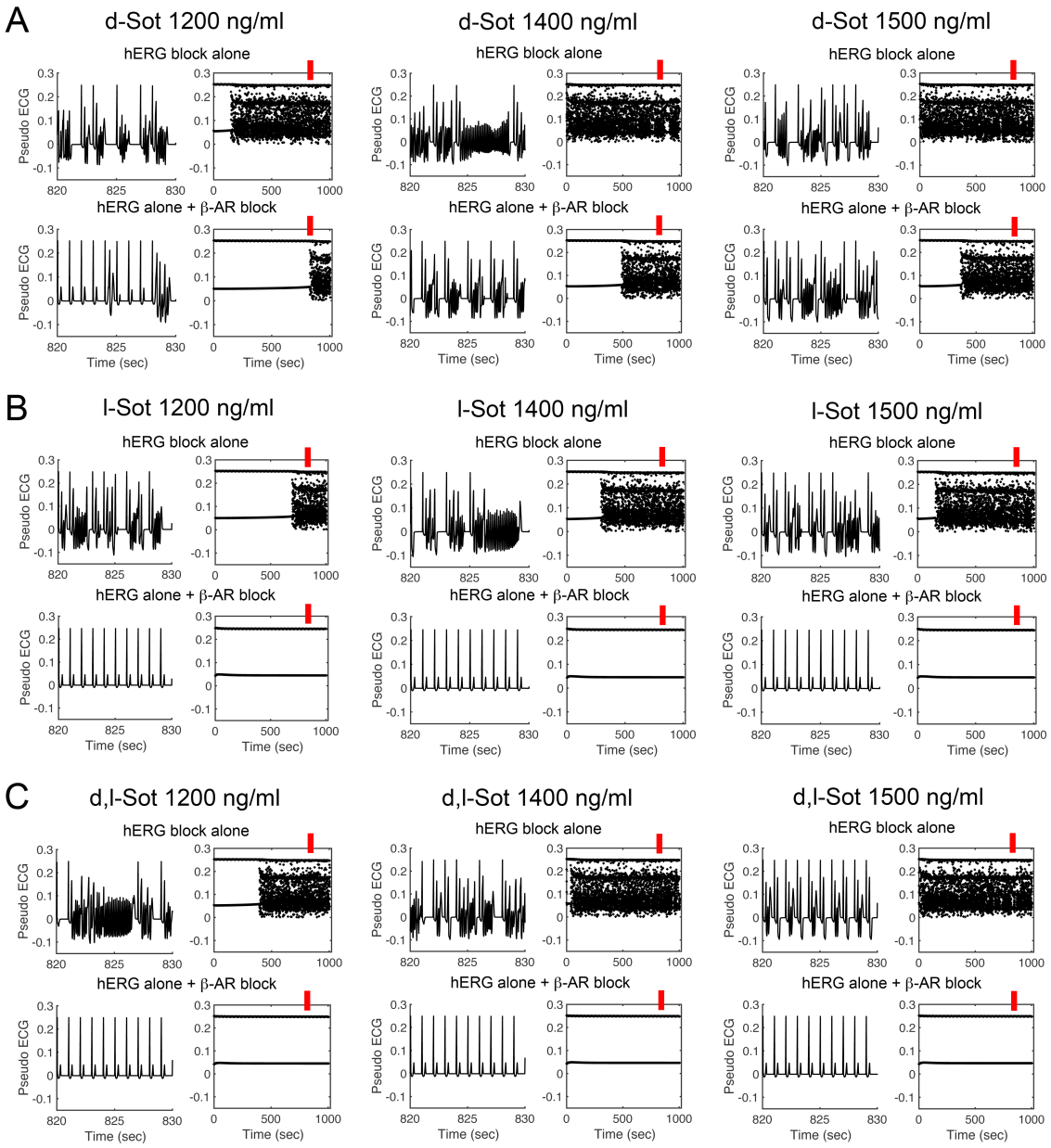

<u>Figure 3.8.</u> Model prediction of Sotalol effects on hERG block and βAR blockade during ISO 1μM application. The timecourse of pseudo ECGs of model 2 between 820 and 830 seconds (red bars) at three sotalol plasma concentrations are shown in the left columns of every panel. The peaks of R and T waves are plotted during a 1000 second long simulation timecourse as summary data shown in the right columns of every panel. **(A)** The predicted additive effect of d-sotalol to block hERG and βAR did not abolish EADs at any tested concentrations. **(B)** l-sotalol with both hERG and βAR blockade abolished EADs at 1200 ng/ml and higher concentrations. **(C)** Similar to l-sotalol, racemic d,l-sotalol 1200 ng/ml removed EADs.

Chapter 4: Modeling Stereospecific Drug interactions with Beta-Adrenergic Receptors

4.1 Introduction

> "Fear, range and pain, and the pangs of hunger are all primitive experiences which human beings share with the lower animals. These experiences are properly classed as among the most powerful that determine the action of men and beasts. A knowledge of the conditions which attend these experiences, therefore, is of general and fundamental importance in the interpretation of behavior.
>
> Walter Bradford Cannon, in Preface to "Bodily Changes in Pain, Hunger, Fear, and Rage," 1915.

Walter Bradford Cannon, the American physiologist who developed the theory of homeostasis, defined the term "fight-or-flight" to describe the downstream consequences of activation of the Sympathetic Nervous System, or SNS[196, 197]. SNS stimulation opposes the action of the Parasympathetic Nervous System, or PNS, which mediates the "Rest-and-Digest" and "Breed-and-Feed" processes[197, 198]. The proper balance of these autonomic systems is fundamental to human physiology and well-being. As society grows more aware of the autonomic nervous system, and as autonomic dysregulation grows more abundant, medicines have been developed to lay a finger on the homeostatic balance between the SNS and PNS.

SNS stimulation of the cardiovascular system increases cardiac output by increasing heart rate, the force of contraction, and conduction rate; consequently, more blood is supplied to the body, a necessary physiological adjustment in circumstances of danger, terror, or exertion[197]. Excessive stimulation of the sympathetic pathway may induce potentially deadly arrhythmias, especially in situations with underlying cardiac disease[10, 199]. The release of one of either catecholamine neurotransmitters norepinephrine (NE), released

from cardiac sympathetic neurons, or epinephrine (Epi), released from the medulla, initiates cardiac sympathetic stimulation[22]. Alternatively known as "adrenaline and noradrenaline," these substances drive the fight-or-flight response by binding the G-protein coupled receptors (GPCRS) named beta-adrenergic receptors (βARs), which are seven-transmembrane segment proteins found within the cardiac myocytes of the human heart and other vascular tissues [25, 200]. By binding to beta-adrenergic receptors, NE or Epi induce the receptor to activate the stimulatory G-protein Gs. Activation of G_s begins the cAMP-induced PKA phosphorylation of a multitude of cellular targets that exert electrophysiological changes necessary to increase contractility[22]. By inhibiting the binding of NE or Epi to beta-adrenergic receptors, one prevents the deleterious effects of excessive sympathetic stimulation. Drugs that prevent this action through antagonism are termed beta blockers[22]. Beta blockers are widely used to treat cardiac irregularities such as atrial fibrillation, myocardial infarction, and heart failure[22]. There are three βAR subtypes within the human heart: β_1, which accounts for approximately 75 to 80% of receptors, β_2, for 15% to 18%, and β_3 for only 2% to 3% of βARs[201]. Though it is critical to note that in the failing human heart, the ratio of β_1 and β_2 subtype becomes approximately equal[202]. Beta blockers have different affinities for each subtype[203], and the populations βARs in non-cardiac vascular tissue differ. Namely, β_2AR is more prevalent in arteries than in the heart and is thus the predominant target of the nonselective hypotensive beta-blocker propranolol [204, 205]. Beta blockers which predominantly target β1AR are "cardioselective" and are the third generation of beta-blockers[206]. However, there is another factor that may affect affinity: stereoselectivity.

In Chapter 3, we discussed the multi-target effects of the antiarrhythmic dl-sotalol, a stereoisomeric beta-blocking drug in functional scale cardiac electrophysiological simulations. While both d- and l-sotalol are capable of blocking hERG ion channel current, only l-sotalol is capable of binding beta-adrenergic receptors with a high enough affinity to attenuate sympathetic stimulation at physiological dose. DeMarco et al. concluded that when modeling hERG potassium channel block, either sotalol stereoisomer is sufficient to induce the markers of deadly arrhythmia in the absence of any simulated sympathetic stimulation[15]. However, incorporating adrenergic signaling into the model eliminates the arrhythmogenic markers for l-sotalol, but not d-sotalol. Indeed, the different selectivity for sotalol has been long known because of the fatal Survival With ORal D-sotalol trial[18], wherein the administration of d-sotalol to intentionally block hERG current in patients proved to be deadly. However, the precise molecular mechanism governing this stereoselective block is not known. Furthermore, the prototypical beta-blocker propranolol also exhibits stereospecificity towards beta receptors[207] and can block hERG channel [19-21], yet whether R-propranolol similarly is also capable of being pro-arrhythmic in the same manner as d-sotalol is unclear. In fact, most beta blockers are administered as racemates. Identifying the mechanisms through which beta-adrenergic receptors exhibit selectivity towards stereoisomers in molecular simulation merits consideration.

In this chapter, we discuss the modeling of beta-blockade at the molecular level for the drugs d-sotalol, l-sotalol, R-propranolol, and S-propranolol and receptor interactions with NE to assess the model quality and finally establish whether molecular interactions can be identified which govern stereoselectivity attributable to cardiac risk (**Table 4.2**). To do so

requires models of the beta-adrenergic receptor subtypes β1 and β2 which predominate cardiac sympathetic stimulation in healthy and pathological conditions. As it is unclear whether these antagonists prefer the active or inactive state conformations or whether the stereospecific selectivity manifests as such, models of both the active and inactive receptor are necessary for either subtype. It is further important to consider the participation of the stimulatory G-protein in maintaining an active state for drug binding; therefore, active state models with and without the Gs heterotrimer are considered.

4.2 Methods

4.2.1. Preparation of β_2AR & β_2AR-Gs templates

Multiple structures of beta-adrenergic receptors and g-proteins are available on the Protein Databank, though not all of them are of the human sequence. While the sequences of bovine and rat G-protein subunits are identical to those of *Homo sapiens*, the same is not true for the beta-1 adrenergic receptor and the turkey-derived structures available at the time this work began. Furthermore, physiologically impactful components such as the ICL3 are not readily resolved because of their intrinsic disorder. In order to model the unresolved regions of the beta-adrenergic receptor protein, templates must be prepared from available experimental structural templates which may further differ in their originating organism.

Therefore, models were prepared identically in preparation for homology modeling to maintain consistent methodology for *de novo* modeling, but only the β_1AR model is a true homology model.

The published x-ray crystallographic structure of adrenaline-activated β_2AR bound to a high-affinity camelid antibody (PDB: 4LDO) was obtained from the Protein DataBank (PDB)

to serve as a template for the activated receptor model[208]. For the protein complex model incorporating the Gs heterotrimer, a Gs heterotrimer template was isolated from the 3D coordinates of the X-ray crystallographic structure of the β_2AR-Gs complex bound to agonist P0G (PDB: 3SN6)[209]. The 3D coordinates were obtained as biological assemblies oriented by the Orientations of Proteins in Membranes (OPM) database to be used for molecular dynamics simulation[210]. The adrenaline-bound receptor 4LDO was aligned to 3SN6 using UCSF Chimera Matchmaker and then used to replace the P0G-bound receptor of 3SN6; then all ligands and non-native protein fragments including the camelid antibody were removed[58]. The resulting template structure consisted of the beta-adrenergic receptor isolated from PDB ID 4LDO in complex with the Gs heterotrimer from PDB ID

3SN6. This complex was then assessed for steric clashes within van der Waals radii and was found free of collisions and thus suitable for structural modeling.

4.2.2. β_2AR & β_2AR-Gs loop rebuilding

The β_2AR structure 4LDO has unresolved the intracellular loop 3 (ILC3), as well as the termini and similarly disordered portions of the G-protein. These regions were modeled *de novo* using the ROSETTA implementation of fragment-based cyclic coordinate descent method (CCD)[55, 211]. Target sequences for remodeled regions of either the human β_2AR (**Fig. 4.2**) and the G_s heterotrimer (**Fig. 4.3**) were obtained from UniProt[212] and visualized using Jalview[213]. The Hybridize Mover of Rosetta comparative (RosettaCM) modeling was applied with the Rosetta Membrane Energy Function[214] to generate ten thousand decoy models of loop-rebuilt β_2Ar-G_s from which a candidate model was selected for further simulation[40, 215, 216]. Rosetta clustering analysis with root-mean-squared deviation

values was used to assess the convergence of models into different microstates using a radius of 2.5 Å[56]. The lowest-energy model of the most populated cluster was selected as a candidate model for additional refinement (**Fig. 4.4**).

Energy minimization was then applied to relax the backbone and sidechain region of rebuilt portions of β_2AR-G_s complex. One thousand energy-minimized decoys were generated from the sequence-complete β_2AR-Gs using the Rosetta FastRelax application with the membrane energy function[217]. Relaxation was permitted only to residues that were modeled *de novo* or residues within 3.5 Å of the α5 helix of G_sα subunit of the G_s heterotrimer. The lowest energy decoy was then selected for ligand docking and MD simulations.

4.2.3. Preparation of active β_1AR-Gs and inactive β_1AR templates

The published X-ray crystallographic structure of isoprenaline-activated, turkey β_1AR bound to nanobody Nb80 (PDB: 6H7J) was obtained from the PDB as biological assemblies lipid membrane oriented by the OPM database[218]. To form the human β_1AR-G_s complex, the sequence-complete G_s heterotrimer model was isolated from our β_2AR-G_s complex model derived from its X-ray crystallographic structure (PDB: 3SN6), ensuring continuity of the G-protein conformation between models[209]. The isoprenaline-bound receptor from PDB ID 6H7J structure was aligned to our β_2AR-Gs candidate model using UCSF Chimera Matchmaker to ensure consistency in orientation with the G-protein-free template and to replace the β_2AR receptor model with the activated turkey β_1AR to create a β_1AR-G_s templates[58]. All ligands and non-native proteins including isoprenaline and nanobody Nb80 were then removed. The resulting template structures consisted of the turkey beta$_1$-

adrenergic receptor 6H7J in complex with our previously modeled Gs-heterotrimer. The turkey β_1AR-G_s complex was assessed similarly for steric clashes using van der Waals radii before homology modeling.

4.2.4. β_1AR & β_1AR-Gs homology modeling

Homology modeling was used to generate putative receptor models of human active-state β_1AR and β_1AR-G_s complex from their homologous turkey-derived template structures using a target sequence for human β1AR obtained from Uniprot. Sequence similarity between the human and turkey structures was (48.65%), permitting effective use of comparative modeling via RosettaCM. Much of the divergence between the β_2AR and β_1AR sequences originate within the length of the ICL3; β_1AR 6H7J structure lacks sixty residues in the ICL3 region, compared to twenty-seven in β_2AR 4LDO. Therefore, multiple sequence alignment using Clustal Omega was first performed to determine the identical start and end points for structural modeling[219, 220]. Human β_1AR was modeled to complete the ICL3 and to match with the N- and C-termini of our β_2AR model, which has the identical sequences in those regions. Partial threading was first performed to generate a sequence-correct human template model fitted into the geometry of the turkey structure and in accordance with the sequence alignment. Then RosettaCM was applied: fragment-based method for protein structure building using templates sampled from a pre-generated fragment library to complete missing regions in a three-stage protocol that completes and refines the modeled geometry in a Monte Carlo trajectory. First, fragment recombination is used to construct a sequence-complete template. Recombination is performed by inserting fragments in torsion space from randomly those randomly selected from the fragment library, and then scored

using the low-resolution centroid scoring function. Second, to optimize this geometry and correct for unrealistic backbone lengths, de novo fragments or library-based fragments are randomly super-imposed to substitute particularly distorted regions of the first stage output and then concludes with another round of full-backbone energy minimization using a cartesian space centroid energy function. After one thousand runs, the lowest energy structure is passed to the third stage. In the third stage, side-chains are incorporated into the model using Rosetta's Monte Carlo combinatorial side-chain optimization, and subsequently minimized using "FastRelax." The Rosetta Membrane Energy Function REF15[221] was used for centroid and full-atom scoring[40]. Ten thousand decoy models of β_1AR and β_1AR-G_s were generated from which candidate models were selected [40, 215, 216]. Rosetta clustering analysis was used to assess the convergence of models into different microstates based on their RMSDs using a radius of 2.5 Å [56]. The lowest-energy decoy of the most populated cluster was selected as the candidate model for additional refinement using Rosetta FastRelax [217]. One thousand energy-minimized decoys were generated for either candidate homology model. Relaxation was permitted only to residues that were modeled *de novo* or residues within 3.5 Å of the α5 helix of $G_s\alpha$ subunit of the G_s heterotrimer. The lowest energy decoy was then selected for ligand docking and MD simulations.

For the inactivated state, the isoprenaline-bound turkey β_1AR structure (PDB: 2Y03) "with stabilizing mutations" was chosen as a template and prepared identically, but without the G_s heterotrimer[222]. Though isoprenaline is an agonist, this structure adopts an inactivate-like conformation, and because it lacks any auxiliary proteins such as nanobodies within the cytosolic region it may serve as a control for assessing allosteric effects in subsequent molecular dynamics simulations.

Preparation of Human β_1AR & β_1AR-Gs Templates from Crystallographic Structures

The release of a more-contemporary membrane energy function "Franklin2019" [221], and critically important the publishing of multiple structures of the human β_1-adrenergic receptor, necessitated a second pass at the modeling both states of β_1AR, and their interactions with the G-protein. Xu et al. published crystal structures of the human β_1AR in complex with epinephrine (PDB: 7BU6) and the antagonist carazolol (PDB: 7BVQ) bound to the nanobody 6B9 [223]. These structures were selected as templates for active and inactive state models of β_1AR, respectively. The previously modeled G_s heterotrimer derived from

PDB structure 3SN6 was used to form a human β_1AR-G_s complex template. All model coordinates were obtained as biological assemblies oriented by the Orientations of Proteins in Membranes (OPM) database, but were subsequently aligned to the previously developed β_2AR-Gs model and cleaned of ligands and all non-native peptides using UCSF Chimera to ensure consistent orientation[58, 210]. The human β_1AR-G_s complex was assessed for steric clashes using van der Waals radii before proceeding to loop modeling.

4.2.5. β_1AR & β_1AR-Gs loop rebuilding

The β_1AR structure lacks coordinates for the ICL3, which in β_1AR is substantially longer and potentially more disordered than its β_2AR counterpart. To harness the new membrane energy function "Franklin2019", a stepwise protocol was devised in place of comparative modeling to achieve better convergence. To model the sixty-residue long ICL3 and eleven residues of C-terminus *de novo*, loop reconstruction was performed using kinematic closure with fragments in staged process[42]. One thousand decoys of the ICL3-added receptor

models were generated and clustered using RMSDs with a radius of 5 Å, and a candidate model was selected from the lowest energy cluster. Four thousand decoy models with added C-terminus were then generated, and a top candidate model was selected from the lowest energy cluster after clustering using RMSDs with a radius of 0.8 Å. Relaxation was performed using FastRelax and the Franklin2019 membrane energy function after ligand docking was performed as described below.

4.2.6. RosettaLigand docking of endogenous norepinephrine and beta blockers to βAR models

ROSETTA-Ligand[224-226] was used to simulate the docking of ligands to β-adrenergic receptors. Up to 200 rotamers and Rosetta energy function parameters were generated for the ligands norepinephrine, R-propranolol, S-propranolol, d-sotalol, and l-sotalol by OpenEye Omega [227] and ROSETTA scripts. A box size of 5 Å was used for ligand transformations such as rotation, translation, and conformational changes along with a 7 Å ligand distance cutoff for side chain and backbone reorientations (with <0.3 Å C_α restraint). 50,000 docked poses were generated in each run with the top 10% selected by total score, out of which the fifty lowest-interfacial score decoys were verified for their convergence and accuracy with the crystallized ligand of their original PDB template structure. Subsequent molecular dynamics simulations were conducted using the absolute lowest-interfacial score structure to serve as the candidate model, unless otherwise specified. Analysis of binding sites was performed in UCSF Chimera[58] and using the Protein-Ligand Interaction Profiler or PLIP[228].

4.2.7. *Molecular dynamics simulations*

Molecular dynamics were used to better understand state-specific dynamics and stability of the human beta-adrenergic receptor complexes and the nature of their interaction with beta blockers. CHARMM-GUI Membrane Builder[46, 67, 229-232], an online web service for establishing initial systems for MD simulations using the CHARRM force field[46], was used to create systems of hundreds of thousands of atoms. The CHARMM-GUI Membrane Builder follows a five-step protocol where PDB coordinates are first read into the web server and then oriented according to parallel XY-planes representing the upper and lower leaflets. The dimensions of the system are then determined, including the minimal extent of water needed. Fourth, the individual components are calculated and built separately: the lipid bilayer is placed around the protein, water molecules are placed to solvate the protein, and ions are placed using Monte Carlo sampling to populate the solvent according to a prescribed concentration. Fifth, these individually built components are assembled into a single system. Sixth, the system and pre-determined equilibration protocol are provided to the user, though this equilibration protocol is inadequate, and the presented systems underwent additional equilibration.

Using this methodology, each beta-adrenergic receptor model was embedded in a heterogenous lipid bilayer of palmitoyl-oleoyl-phosphatidylcholine (POPC) and palmitoyl-oleoyl-phosphatidylserine (POPS) of approximately two hundred lipids per leaflet. This composition was adopted from previous simulations by Dror et al.. 2015[233], and consisted of an upper leaflet of POPC lipids and a bottom leaflet 70:30 mixture of POPC:POPS lipids. Protonation states, terminal group patching, histidine protonation, and lipidations were

similarly derived from Dror et al., 2015. Critically, each receptor was protonated at the equivalent residues Glu147 and Asp155 for β_1AR, or Glu122 and Asp130 for β_2AR. S-palmitoylation is specified Cys392 in β_1AR and Cys341 in β_2AR. For all simulations incorporating the G-protein, heterotrimer, the three additional residues were further lipidated: Gly2 of Gsα was myristoylated and Cys3 palmitoylated, while Cys68 of Gγ was geranlygeranylated. Beta-receptors were given acetylated N-termini and methylamidated C-termini as terminal patches. When included, the heterotrimeric G-protein termini were also patched. Gsα was given a standard C-terminus, but as the N-terminus of Gsα forms the crucial α-5 helical insertion that mediates receptor association, Gsα was given no N-terminal patch. Gβ had an acetylated N-terminus and a standard C-terminus. Gγ had an acetylated N-terminus and methylated C-terminus as this region inserts into the lower leaflet. All histidines were epsilon-protonated, except residues 225 and 331 of Gβ which were instead delta protonated. The system was solvated with 150mM aqueous NaCl using the CHARMM36m all-atom force field. The TIP3P water model was used. Parameters for drugs norepinephrine and RS-propranolol were first obtained via CGENFF [234, 235], the generalized CHARMM force field for small molecules. Norepinephrine was further optimized using the FFTK protocol in conjunction with Gaussian software[236, 237]. Parameters for sotalol were generated by Drs. Kevin DeMarco and Igor Vorobyov and published in DeMarco et al, 2021[15].

Simulations were performed with Nanoscale Molecular Dynamics (NAMD) software[47]. Simulations were conducted in an NPT ensemble at 1 atm pressure and 310K. Visualizations and analysis were performed in VMD[238] and using in-house scripts. To extend timeframes

on the order of microseconds, equilibrated systems were run on the ANTON supercomputer[239, 240].

4.2.8. Equilibration protocol

All systems underwent a 40-nanosecond staged equilibration protocol to allow time for added regions of the proteins to rearrange, without risking the stability of the protein core, and to establish reference data for the drug poses to compare conformations with and without restraints.

Stage	Steps	Duration(ns)	Restraint (kcal/mol)
1	7.1 - 7.4	4	1.0 for all backbone Cα carbons.
2	7.5 - 7.10	6	1.0 for backbone Cα carbons not modeled *de novo*.
3	7.11 - 7.15	5	0.5 for backbone Cα carbons not modeled *de novo*.
4	7.16 – 7.20	5	0.25 for backbone Cα carbons not modeled *de novo*.
5	7.21 – 7.30	10	0.1 for backbone Cα carbons not modeled *de novo*.
6	7.31 – 7.40	10	0.5 for backbone Cα carbons within 3.5 Å of docked or crystallographic ligand.
7	7.41 – 90	50	No restraint.

Table 4.1. Restraint Regime for Extended Equilibration.

4.3 Results

4.3.1 Modeling active and inactive state beta adrenergic receptors using RosettaCM

Ten-thousand decoy models were generated for both active and inactive states of human β_2AR and β_1AR structural models derived using human β_2AR or turkey β_1AR template structures with RosettaCM. For active-state models, bound stimulatory G (G_s) protein was present based on its structure from the β_2AR-G_s complex (PDB ID: 3SN6). The top four most-

populated clusters were examined for each of them, but no clear relationship between root-mean-square deviation (RMSD) from the top-scoring decoy and a given decoy's score could be established (**Fig. 4.5 B&D**).

In the case of active state β_1AR, the intracellular loop 3 (ICL3) was so disordered such that clusters were entirely governed by the orientation and direction of ICL3 and not its secondary structure. Therefore, the candidate model was chosen based on the assumption that the ICL3 would not readily penetrate region which Rosetta treats as implicit membrane. The candidate model was thus the top scoring decoy from cluster 2 (**Fig. 4.5 A**)**.** Curiously, loop remodeling with the membrane energy function permitted loops to traverse into the implicit membrane. As $G_s\alpha$ was present during loop remodeling, the ICL3 could not similarly be built downwards into solvent as it could be outward or upward.

As the ICL3 of β_2AR is significantly shorter than that of β_1AR (10 residues vs. 30 residues in β_1), the loop would not rebuild into implicit membrane region, and clusters therefore aggregated either away from or adjacent to $G_s\alpha$. (**Fig. 4.5 C**)**.** In this instance, the top scoring decoy of the lowest-energy cluster was selected as the candidate model (**Fig. 4.5 C**).

The same protocol and selection criteria were applied to select an inactive state β_2AR model (**Fig. 4.4 A, top**) in the absence of the G_s heterotrimer. For inactive β_1AR the lack of the G-protein meant *ab initio* modeling of an entirely unconstrained thirty-residue long ICL3. Clustering yielded twenty low-population clusters (**Fig. 4.6B**) that lacked any predominant secondary structure aside from the top-scoring model (**Fig. 4.6C**) which was selected to be the candidate model and relaxed.

4.3.2 Docking of norepinephrine into RosettaCM-derived active and inactive state beta adrenergic receptors

To validate preservation of the ligand binding pocket and to generate representative models of functional receptor complex with its endogenous ligand, neutral and cationic norepinephrine were docked into active state models of both receptors as well as the inactive state model of β_2AR **(Fig 4.7)**. Top fifty poses for all conditions except neutral norepinephrine in active β_2AR exhibited tight binding. Only in the case of cationic norepinephrine docking to active β_2AR was the crystallographic epinephrine binding pose (**Fig 4.7A**) consistently recapitulated. The order of peak probabilities of interfacial scores or interaction energies (IE) would suggest that the more similar the crystal ligand is to the docked ligand, the lower the IE. The mean IE of docked norepinephrine into a formerly epinephrine occupied binding pocket from PDB ID 4LDO is more favorable than docking into a formerly isoprenaline (agonist) or propranolol (antagonist) bound models based on PDB IDs 6H7J and 6PS5, respectively[218, 241]. However, their probability distributions nearly overlap (**figure 4.7D**). This trend is abolished for the case of neutral norepinephrine, despite mostly tight geometric convergence within the binding pocket, a change likely attributable to expected much higher affinity of cationic NE binding to β_2AR, which cannot be directly assessed using Rosetta energy scoring function.

4.3.3 Docking of stereoisomeric beta blockers into RosettaCM-derived inactive state beta adrenergic receptor

The top fifty scoring poses of docked d- and l-sotalol docked to inactive β_1AR occupy nearly identical regions of the binding pocket and their IEs in Rosetta Energy Units (REU) are

statistically indistinguishable (l-sotalol: -10.64 +/- 0.71 REU versus d-sotalol -10.67 +/- 0.37 REU, averaged over the top 50 poses) (**Fig. 4.8A**). Their top binding poses both have their sulfonamide moiety in the same orientation within the binding pocket, and coordinating with Ser228 but not Ser232. Both serine residues, denoted Ser $S^{5.24}$ $S^{5.46}$ Ballesteros-Weinstein nomenclature[242] govern catechol hydroxyl recognition[243] as seen in the crystal structures for β_1AR-Epinephrine(PDB ID: 7BTS) and β_1AR-Norpinephrine(PDB ID7BU6), and the and crystal structures of β_2AR-Epinephrine(PDB ID: 4lDO)(**Fig. 4.8 A&B**)[223]. Cationic RS-propranolol, being a larger molecule, occupied a larger volume of the binding pocket, including a region deeper into β_1AR interior, which is seldomly sampled by sotalol (**Fig. 4.9A&B**). The mean IEs of the top fifty poses for both stereoisomers lie within error of one another (S-propranolol: -13.19 +/- 0.34 REU versus d-sotalol -13.31 +/- 0.64 REU). Both sets of docking data tougher indicate that IEs computed using RosettaLigand may not account for experimentally known stereospecificity against the β_1AR homology model. Therefore, molecular dynamics simulations were conducted based upon the candidate sotalol-β_1AR complexes shown in **Fig. 4.8B**.

4.3.4 Molecular dynamics of sotalol interactions with the human β_1AR homology model

To test whether incorporating dynamics into these systems could potentially reveal the stereospecific drug binding preferences, the candidate poses of human β_1AR homology model docked to either d- or 1-sotalol were simulated using fully atomistic molecular dynamics. However, as the docking simulations suggested, no stereospecific preferences were observed in MD simulations either. **Fig. 4.10** depicts results of multi-microsecond unbiased MD simulations of either sotalol stereoisomer bound to the inactive-state β_1AR

model. Between the two stereoisomers, l-sotalol reorients most significantly during the simulation, yet both maintain the same orientation within the binding pocket and end the simulation at approximately 4 Å RMSD with respect to the initial binding pose. Curiously, while both drugs begin with similar positions of their sulfonamide group with respect to the receptor, in the case of d-sotalol this moiety digs deeper into the protein interior and holds a consistent orientation for longer. However, the dynamical consequences of sotalol binding on the receptor structure do not significantly differ between stereoisomers. In both conditions the receptor adopts a more inactivated orientation, with TM6 shifting more inward,. With no clear obvious distinction suggesting preferential β_1AR interactions with l-sotalol over d-sotalol, enhanced sampling MD simulation techniques are necessary.

4.3.5 Structural modeling of active and inactive state of beta-1 adrenergic receptors

Recently human beta-1 adrenergic receptor structures were published[223], which eliminates homology modeling as a potential variable in experimental design. Therefore, we developed new models of β_1AR using those structures as templates and adjusting our previous Rosetta protocol to achieve better convergence and potentially accuracy as well. The protocol for creating models was like the RosettaCM process described above and is depicted in **Figure 4.11A**, however *ab initio* structural modeling was broken up into two steps of kinematic loop remodeling with fragments. Whereas using our previous approach RosettaCM yielded one model with the ICL3 and the C-terminus rebuilt, this new protocol performed the *ab initio* modeling in two separate steps. This permits the best practice of selecting for the most-convergent regions per-segment; clustering is otherwise less effective when assessed by RMSD across the entire protein as was done previously. Furthermore,

eliminating RosettaCM meant that template sidechains were unchanged, better preserving the binding site conformation. Lastly, the alternative loop modeling protocol, when applied using the Franklin2019 Rosetta membrane energy function, also eliminated membrane-penetrating loop rebuilds which would otherwise be discarded and worsened sampling. The final active and inactive state protein models, shown docked with norepinephrine in **Fig. 4.11A&B** (right-hand side) have considerably different ICL3 when compared to those in **Fig. 4.4B and 4.6D**.

To validate stability of the model, the active receptor was simulated in molecular dynamics without the G-protein after being docked with cationic norepinephrine in accordance with the previous RosettaLigand and MD simulation protocol (**Fig. 4.12**). The final frame of the MD simulation illustrates a loss of some secondary structure of the ICl3 as it extends in the aqueous solution. Norepinephrine binding remained intact, and so we proceeded to docking beta blockers to our new human β_1AR structural models.

4.5.6 Docking of stereoisomeric beta blockers into active and inactive state beta-1 adrenergic receptor models

Beta blockers RS-propranolol and dl-sotalol were docked into the new human β_1AR structural model using a RosettaLigand protocol outlined above. When docked to the active-state β_1AR model, the same findings as determined via the receptor homology model held: the most favorable interfacial scores between d- and l-stereoisomers of sotalol were indistinguishable (see **Fig. 4.13A**).

When examining the average interfacial energy of the top fifty poses, we found that R- and S-propranolol had more favorable interface energies (R-propranolol: -14.05 +/- 0.08 REU, S-propranolol: -14.20 +/- 0.09 REU) than sotalol (l-sotalol: -9.76 +/- 0,40 REU, d-sotalol: -10.01 +/- -.42 REU). Though top 1 pose of d-sotalol scored higher than the top 1 of l-sotalol (-13.46 REU, not shown), the top 2 pose of d-sotalol was selected as a candidate model on account of orientation. For all candidate poses, binding orientation is distinct from co-crystalized NE from the original template structure (**Fig. 4.13B**). One of either opposing asparagine residues Asn344 and Asn363, associated with receptor type selectivity, and one of either serine residues Ser228 or Ser232, associated with catechol hydroxy recognition, are forming hydrogen bonds with the ligand for all beta blockers(**Figure 4.13C)** [243]**.**

Average interfacial energies determined from the top fifty poses against the inactive state β_1AR model indicate that RS-propranolol binding worsened, while l-sotalol binding improves and d-sotalol remains constant (**see average IE of Figs. 4.13A and 4.14A**). Regarding differences between isomer, S- and R-propranolol lie within error (S-propranolol: -13.97 +/- 0.88 REU versus R-propranolol: -12.68 +/- 0.53 REU)(**Fig. 4.14A).** The average interface energies for sotalol overlap, suggesting no difference (l-sotalol: -10.87 +/- 0.098 REU versus d-sotalol: -10.18 +/- 0.63 REU)(**Fig. 4.14A**). The top pose for S-propranolol but not R-propranolol bind similarly to co-crystallized carazolol from the original structure(**Fig. 4.14B**). The top 1 pose for l-sotalol and top 2 pose d-sotalol, with similar scores, have aligned their sulfonamide groups similarly (**Fig. 4.14B**). the top 1 pose for d-sotalol (not shown), scored considerable higher than the top 2 pose (-14.26 REU) and had flipped such that its

propran-2-ylamino group was located where the methanesulfonamide position was for the top 2 pose.

We no longer observe participation of serine in the top poses of RS-propranolol docked to the inactive state; instead Tyr367 or Tyr220 participate (**Fig. 4.14C**). For sotalol, both candidate poses interact with Ser228, Thr220, and Phe218, with the distinction being the coordination of either Thr220 or Asn344 with the hydroxy moiety of sotalol, a consequence of their chiral center (**Fig. 4.14C**).

When overlaid, the ensembles of top fifty scoring poses for each drug diverge significantly in general shape and orientation for active β_1AR model than those obtained from docking to the inactive state receptor model (**Fig. 4.13A & Fig.4.14A**), suggesting that the volume available for the ligands is quite different. This may account for the different binding modalities observed in the sotalol ensembles. When docking to the active(?) state, the sotalol adopt a linear orientation with the sulfonamide "digging" into the binding pocket (**Fig.4.14A**). However, in the inactive state, there is a bifurcation in orientations that differ from the active-state modality (**Fig. 4.13A**).

We observe some distinctions in ensemble orientations when comparing the top fifty poses of beta-blocker docking against either turkey-derived β_1AR homology model or the human-derived β_1AR model. For instance R- and S-propranolol binding pose ensembles were tighter when bound to the human-derived model in comparison to the homology model, where the set of poses adopted a flatter, more distributed shape **(cf. Figs. 4.9A & 4.14A**).The top

interfacial energy scores for either stereoisomer improved by about one Rosetta energy unit form their corresponding top poses against the β_1AR homology model (cf. Figure 4.9B and 4.14B). The top fifty poses of active-state propranolol binding β_1AR are dominated by two observable orientations, with our docked R-propranolol seemingly favoring the binding orientation seen in the crystallographic pose of S-propranolol PDB ID 6PS5, and docked S-propranolol favoring the opposite orientation (**Fig. 4.13A**). The inactivate-state β_1AR - propranolol docking abolishes this pattern in the top 50 poses (**Fig.4. 14A**), and S-propranolol poses form a tight cloud around the orthosteric ligand binding pocket in contrast to R-propranolol which exhibits a binding modality more like sotalol, interacting with the β_1AR extracellular vestibule.

We also analyzed interacting β_1AR residues for each top ligand binding pose as shown in panels C of Figures 4.13 and 4.14. One consistent pattern between the top poses of docked sotalol is the participation of Ser228 for both inactive and active states with the exception of active β_1AR - d-sotalol interaction (**Fig. 4.13C & Fig. 4.14C**). In addition, Asn344 participates in active, but not inactive state β_1AR binding of sotalol (**Fig. 4.13C & Fig. 4.14C**) Validating whether this pattern is indicative of a stereospecific, state-dependent interaction necessitates a more thorough examination of the full data set than is presented here. Lastly, it is of note that the preferential interaction of R-propranolol is consistent across β_1AR model systems discussed here. R-propranolol has a more favorable interfacial score(?) than S-propranolol when docked to the inactive human β_1AR homology model based on turkey receptor structure (**Fig. 4.9B**) as well as new inactive-state (**Fig. 4.14B**) and active-state (**Fig. 4.13B**) β_1AR models developed using human receptor structures

4.4. Discussion

In this work, we constructed the first homology models of contiguous Human B_1AR in complex with the stimulatory G-protein and in the inactive state before the publishing of human structures. We similarly developed models of β_2AR and β_2AR-Gs. We docked norepinephrine into the β_2AR models and found the top poses to be in good agreement with a β2AR structure co-crystallized with epinephrine. Docking the inactive homology model of human β_1AR beta blockers dl-sotalol and RS-propranolol indicated more favorable energetic interactions for propranolol than sotalol, but no preference for a stereoisomer was observed. Subsequently simulating the docked stereoisomers of sotalol in multi-microsecond molecular dynamics indicated that both poses were stable but did not differ significantly in their trajectories.

Upon the release of human β_1AR crystal structures, we developed new models with an alternative protocol using the latest Rosetta Membrane Energy Function. In this instance, the active state interactions with the human β_1AR model recapitulated the findings with the homology models. However, the average interface energies for the top fifty poses against the inactive state suggest a slight preference for the l-sotalol and S-propranolol.

This work can be improved upon through devising enhanced sampling molecular dynamics experiments that sample the energetics along a reaction coordinate that captures the complete transit of the drug from solvent into the binding pocket for reasons that are discussed below. To assess drug – protein interaction during drug entrance or egress may identify the determinizing factor stereospecific binding. Drug flooding simulations can be

used identify reaction coordinates for drug access. Once a reaction coordinate is determined, enhanced sampling molecular dynamics such as Umbrella Sampling should be sufficient for determining the free energy profiles and subsequently the dissociation constants for either stereoisomer of either drug[15, 16].

4.4.1. The vestibule as a mechanism of stereoselectivity

One reason that may account for the small difference between stereoisomer Rosetta energies is the possibility that a different portion of the protein is conveying selectivity. Dror et al. have shown in MD simulations that ligands encounter a large energy barrier when transitioning from the vestibule, an intermediate region between the extracellular space and the binding pocket, into the binding pocket[244]. This intermediary binding site may be more selective than the binding pocket itself, so while d-sotalol and l-sotalol are theoretically very stable when occupying the pocket, d-sotalol may simply have a more difficult time passing the vestibule. It is of note that there are very few differences in sequence identity between the β_1 and β_2 subunits within the binding pocket itself; they are effectively identical in sequence within the pocket, with only a Phe/Tyr substitution[245]. Otherwise, the most proximal the in sequence reside at the edge of the pocket, near the vestibule[243].

4.4.2. Regarding the selection of homology models and clustered models

Further iterations of relaxation of the top decoy of each candidate model may provide better criteria for decoy selection and provide a quantitative justification for selecting one cluster over another, as opposed to assuming that membrane-penetration is not feasible. Alternatively, we should consider using the most-likely decoy as opposed to the lowest

energy decoy. This would mean considering the distribution of scores within a cluster and thus select multiple mean-value decoys from which a second round of clustering may be used assess the validity of each cluster in this new set of mean decoys. However, molecular dynamics samples conformations extensively. **Fig. 4.12** demonstrates how rapidly the ICL3 can rapidly adopt alternative conformations that would significantly increase protein root-mean-square deviation (RMSD) values, but at the same time it may still retain some secondary structure elements.

4.4.3. The possibility of allostery not captured by docking

It is important to acknowledge that the human β_1AR homology model was derived from an isoprenaline-bound template that resembles an inactive structure. In other words, we docked antagonists into a formerly agonist-bound pocket. This may explain why propranolol failed to recapitulate the pose adopted in a known crystallographic binding pose of the ligand during docking (**Fig. 4.9**). This may indicate that suggests that perturbing local sidechain and backbone orientation is inadequate to capture beta-blocker-like interactions with the receptor. Larger backbone movements may be associated with facilitating inactivation within the binding pocket, movements that cannot be sampled by RosettaLigand with the present protocol. In the case of sotalol, it may be that the structure is flexible, but we also may have not captured the experimental binding pose in our ensembles. Future molecular dynamics simulations ought to examine receptor backbone reorganizations and potentially correlate such movements with drug orientation in the binding pocket and could be assessed using e.g. position and polar angle of the ligand binding orientation as was shown in Chapter 3.

4.4.4. Alternative measures, a new hypothesis, and alternative sites of stereoselective discrimination

One advantage of assessing stereoisomers is that one may appropriately compare the scores between them when evaluating drug docking. A more thorough examination of docking energetics, hydrogen bonding networks, and contact maps should be performed on the top 1 to 5 percent of binding poses to yield a more substantial dataset for such analysis: for instance, Smith & Meiler found in screening tests that within the top 1% of top-scoring poses, 21% of those poses will recapitulate a native binding pose when using the Rosetta Score function Talaris2014[246, 247], with this dropping off 6.9% for any of four assessed score functions[248]. This drops to 4.4% and 3.1% when using the top 5% or 10% of poses respectively[249]. This means when examining the top 5,000 poses of 50,000, we may conservatively estimate that 155 models will recapitulate native binding. If we select to 1%, we can expect 34 of 500 poses to be accurate representations of native binding; using Talaris2014 could raise this to one in five models. At that level of fidelity, introducing alternative quantities such as binding density, the ratio of binding energy to buried surface area, can provide new measures to support alternative candidate docked ligand conformations, or perhaps ligand clustering would be a sufficient to determine a candidate.

Ultimately, determining the energetics and kinetics of the interactions based upon an identified reaction coordinate would circumvent the present inadequacies. Determining the dissociation constants of dl-sotalol against β_1AR across multiple states using enhanced sampling methodologies can address the inadequacies in the present study or provide

alternative hypotheses that may reveal allosteric interactions necessary for β_1AR to discriminate between stereoisomers. One key consideration is whether access via the previously discussed extracellular vestibule above the binding pocket is stereospecific. Dror et al observed a metastable binding position for the beta blocker alprenolol occurring at the extracellular vestibule above the receptor[244]; they conclude that the primary barrier to binding is this metastable site outside of the binding pocket. While our top fifty poses interactnear regions adjacent to the inner vestibule in varying orientations it is unclear whether we can readily observe this phenomenon from the present analysis (**Fig. 4.14A&B**). I would hypothesize that the molecular mechanism for stereospecific selectivity occurs at this vestibule rather than the binding pocket, and is perhaps state-dependent, given our present conclusions. Therefore, simulations should be conducted to search not only the absolute free-energy minimum within the binding pocket, but also for free energy minima that serve as a metastable state preceding interaction with the orthosteric binding pocket. Should atomistic molecular dynamics be unfeasible for assessing the along this access pathway, then adjusting the RosettaLigand docking window to target the extracellular vestibule warrants consideration. Capping this vestibule is the extracellular helix of extracellular loop 2 (ECL2). To test this hypothesis, examination of ECL2 motility from previous simulations and assessing sequence conservation between receptors in relation to stereospecific ligand affinities would be a first step towards assessing extracellular portions of the receptor governing stereoselectivity of ligand binding.

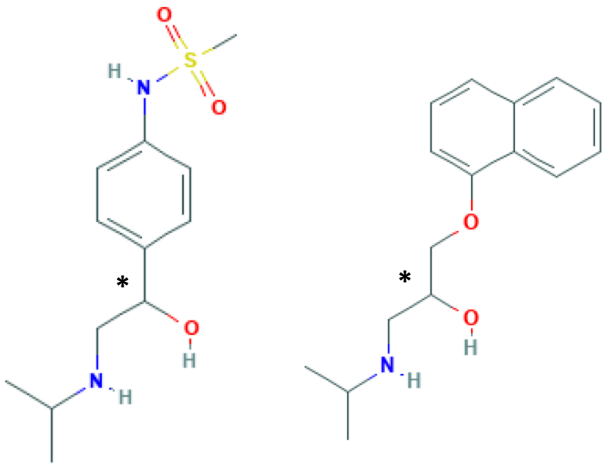

	dl-sotalol	RS-propranolol
I_{kr} Block	Yes	Yes
QT Prolongation	Yes	Yes
βAR Binding	β_1 & β_2	β_1 & β_2
Arrhythmia Risk of d- or s-Enantiomer	High	Unknown

Table 4.1. Structure and arrhythmogenic properties of racemic beta blockers dl-sotalol and RS-propranolol.
Chiral centers denoted with asterisk.

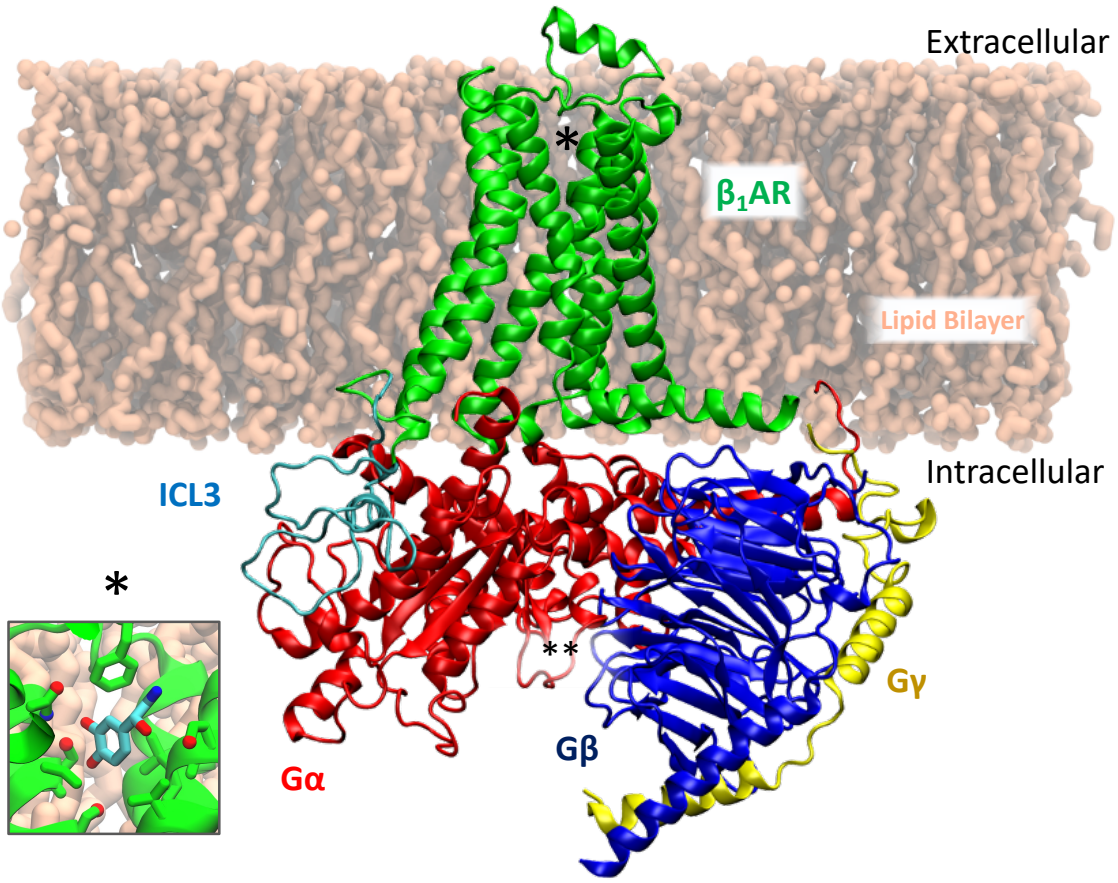

Figure 4.1. Beta1-Adrenergic Receptor (β_1AR) in Complex with the Stimulatory G-Protein (G_s) Heterotrimer. When expressed at the plasma membrane, the beta-adrenergic receptor is oriented such that the ligand binding pocket (*) is accessible to ligands from the extracellular side (Ex.) of the membrane. The $G_s\alpha$ (red), Gβ (blue), and Gγ (yellow) subunits comprise the G_s heterotrimer. Nucleotides GDP or GTP bind Gα at the P-loop(**). Inset: Representative image of Norepinephrine bound within the ligand binding pocket.

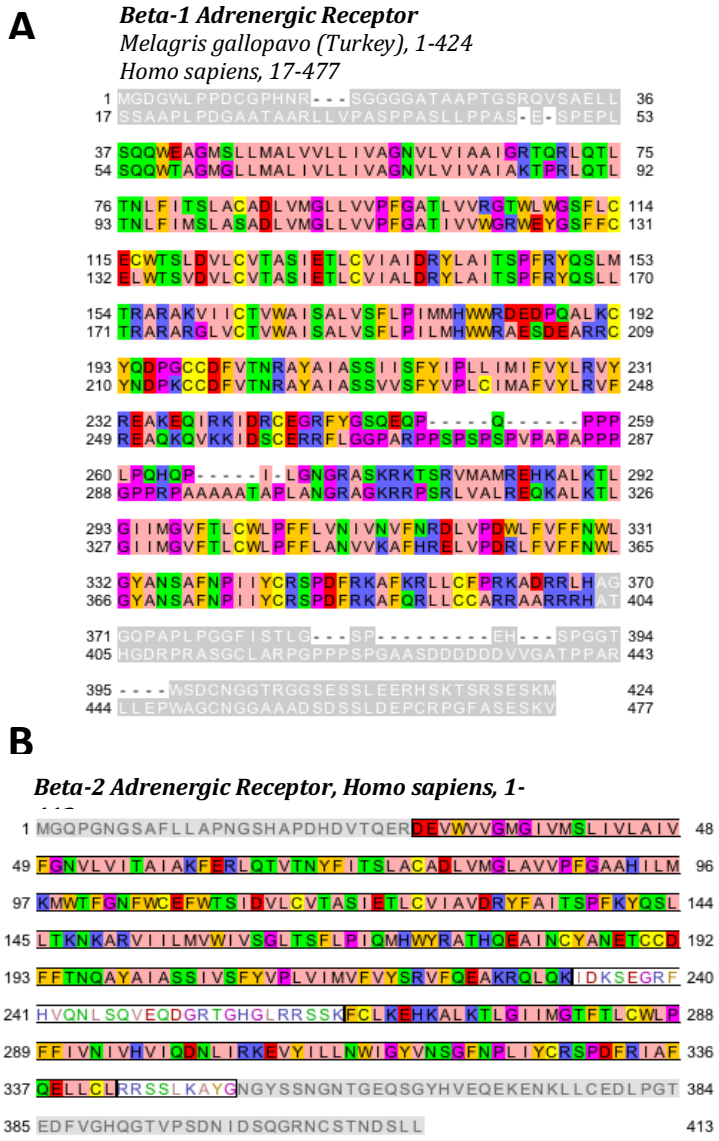

<u>Figure 4.2.</u> Amino acid residue sequences of the Beta-1 Adrenergic Receptor (β_1AR) and Beta-2 Adrenergic Receptor (β_2AR). (**A**) Pairwise sequence alignment of the amino acid residue sequences for β_1AR genes for turkey (above) and human (below) visualized using Jalview. Residues in "Zappo" color scheme are modeled whereas grey-colored residues were omitted from modeling. The intracellular loop 3 (ICL3) for the human protein sequence spans residues 256 to 314 and was modelled *de novo*. *De novo* modeling of the C-terminus spans residues 342 to 350. (**B**) The β_2AR sequence included in the template model("Zappo" coloring). Regions that were modeled *de novo* are denoted with colored text and white backgrounds: the ICL3 spanning residues 233 to 263 and the C-terminus spanning residues 342 to 351.

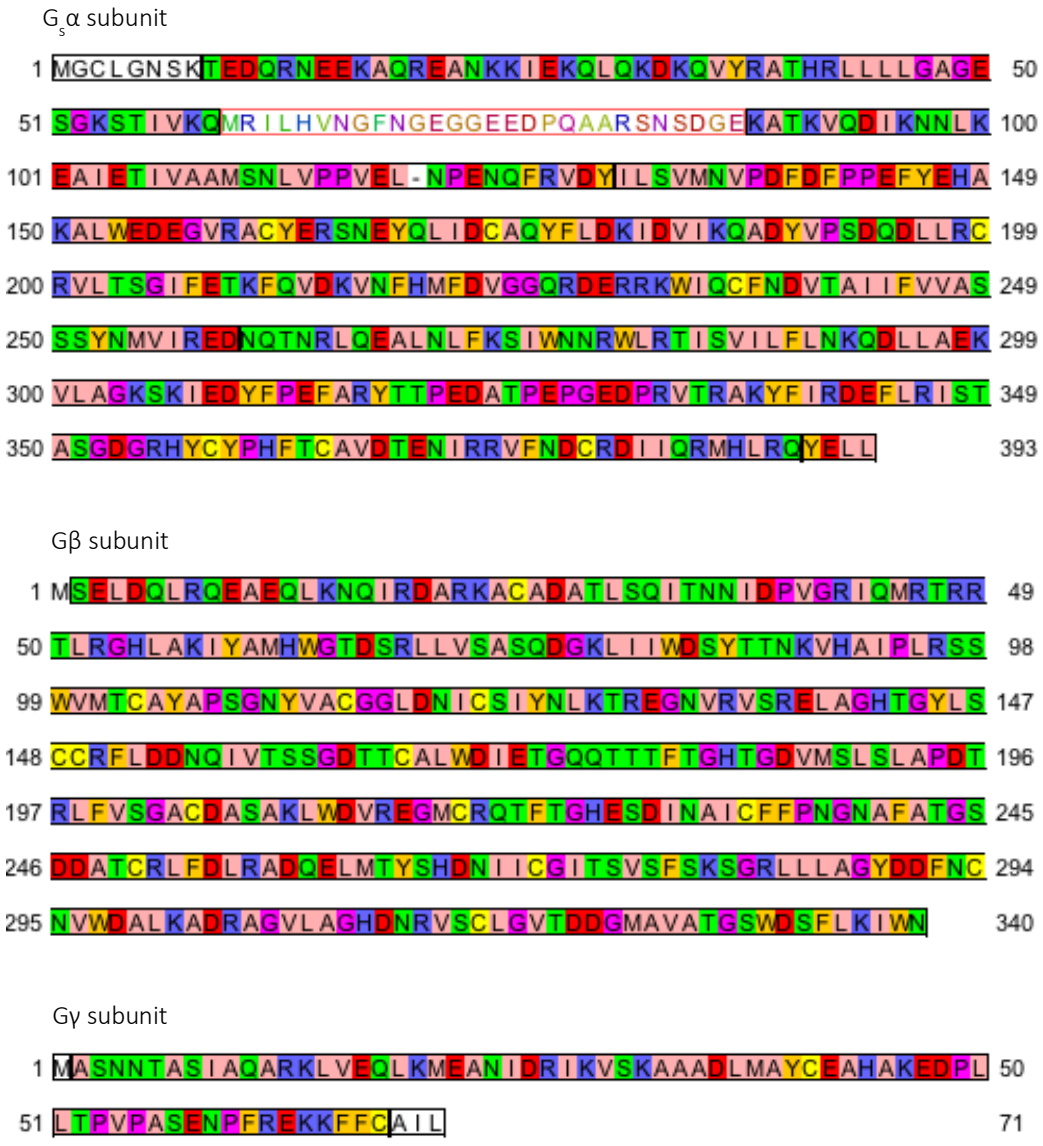

<u>Figure 4.3.</u> Protein Sequences of G-Protein subunits Gsα, Gβ, and Gγ. All three sequences are imaged in "Zappo" coloration using Jalview. Sequences depicted in black and white including, N-terminal Met, which genetically encoded were omitted from unresolved in the template model. *Gsα Subunit.* Residues 61 to 87 of Gsα were modeled *de novo* using RosettaCM and are depicted in color text with white background. Residue 72 of Gsα ("-") is Ala. *Gβ Subunit.* All residues of the gene Gγ Subunit excluding N-terminal Methionine are modeled. Residues 62 to 68 of Gγ are modeled de novo and were not resolved in PDB ID 3SN6.

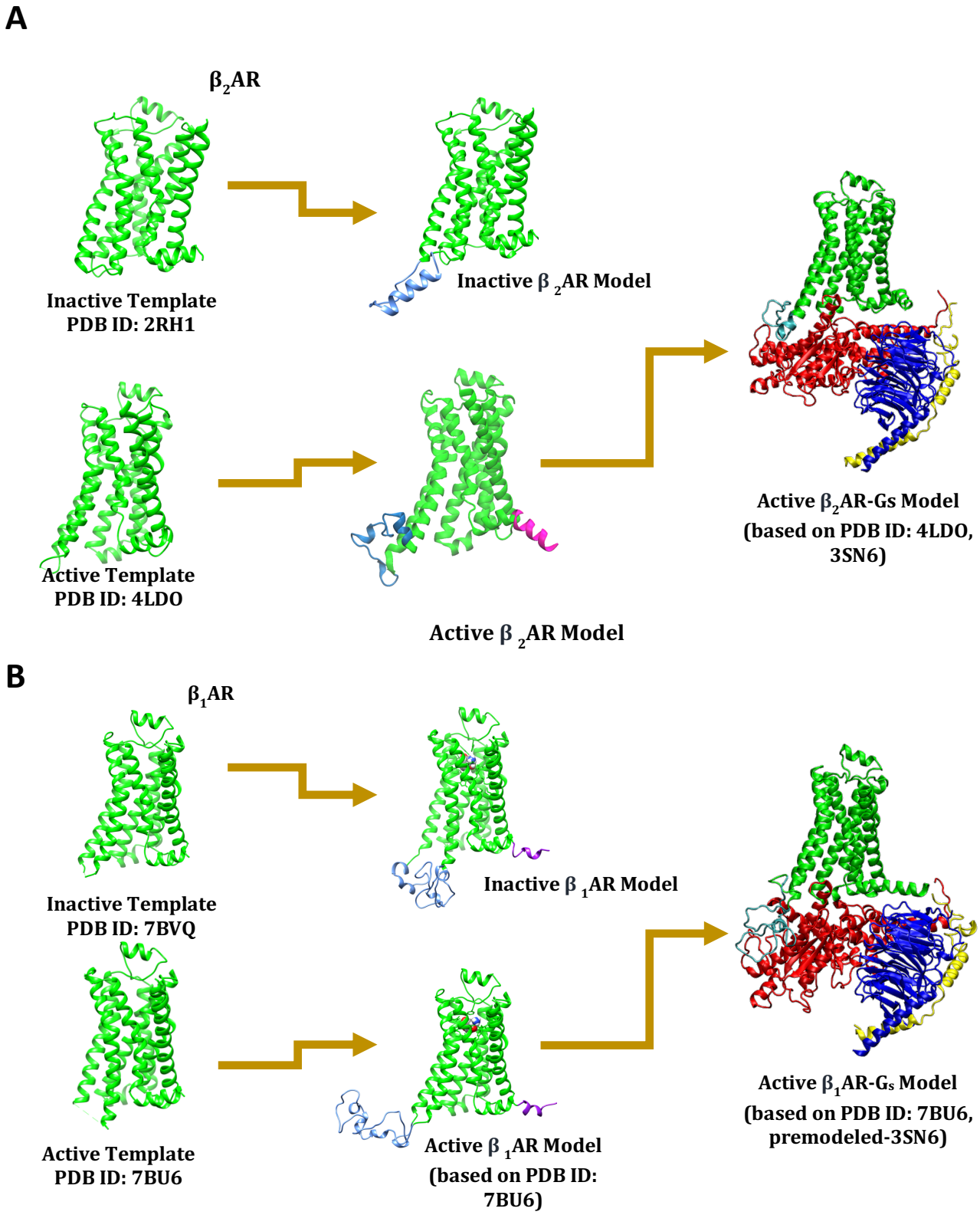

Figure 4.4. Schematics of modeling protocol for (A) β_2AR and (B) β_1AR and their complexes with the stimulatory G (G_s) protein developed Using RosettaCM. Template models are prepared from published crystal structures for respective states. For active state models Loop modeling and FastRelax are performed in the presence of the G-protein.

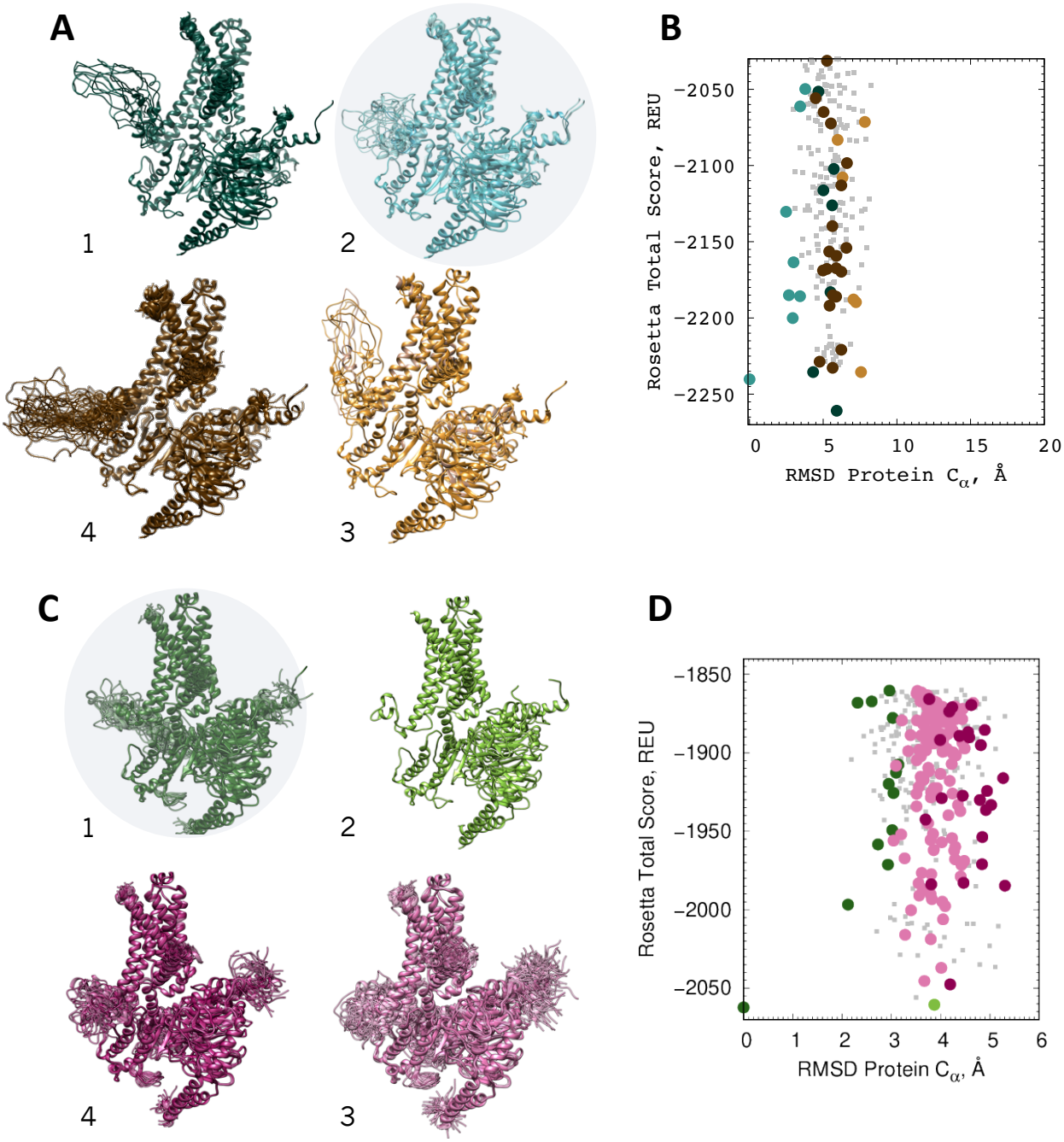

Figure 4.5: Clustering analysis of active β_1AR/G_s and β_2AR/G_s models developed using RosettaCM protocol. (**A**) Top four clusters for β_1AR/G_s demonstrating that gross orientation of the β_1AR ICL3 (shown as a protrusion in the left central portion for each model) governs clustering. The candidate model is selected from cluster 2 (circled). (**B**) Graph of total Rosetta energy score for each clustered β_1AR decoy according to root-mean-square deviation (RMSD) from the candidate model. Top four clusters are colored according to their image on the left. (**C**) Top four clusters for β_2AR/G_s demonstrating tighter convergence about the shorter ICL3 (small protrusion on the left for

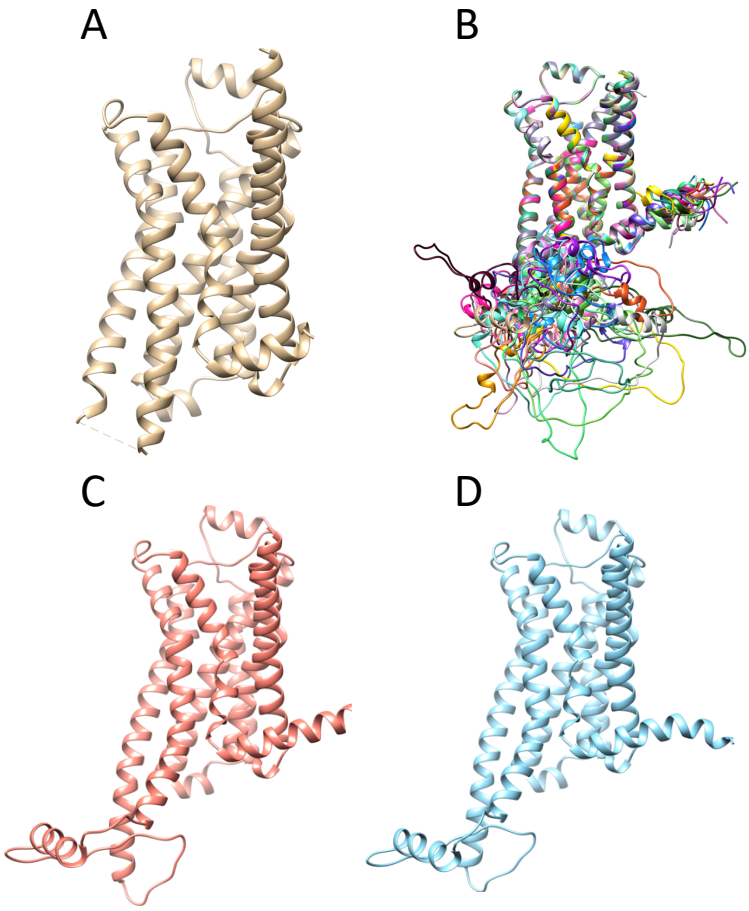

Figure 4.3. Stages of homology modeling for inactive human β_1AR from turkey β_1AR (PDB ID: 2Y03). (**A**) The template PDB after removal of ligands isoprenaline, cholesterol hemisuccinate, and HEGA-10**. (B**) Steric clashes prohibited incorporating a G-protein into modeling; in the absence of the G-protein, the top decoys of the top 20 clusters demonstrate poor convergence when overlaid. (**C**) Candidate model selected from 10,000 decoy models. (**D**) Candidate model after restrained relaxation step.

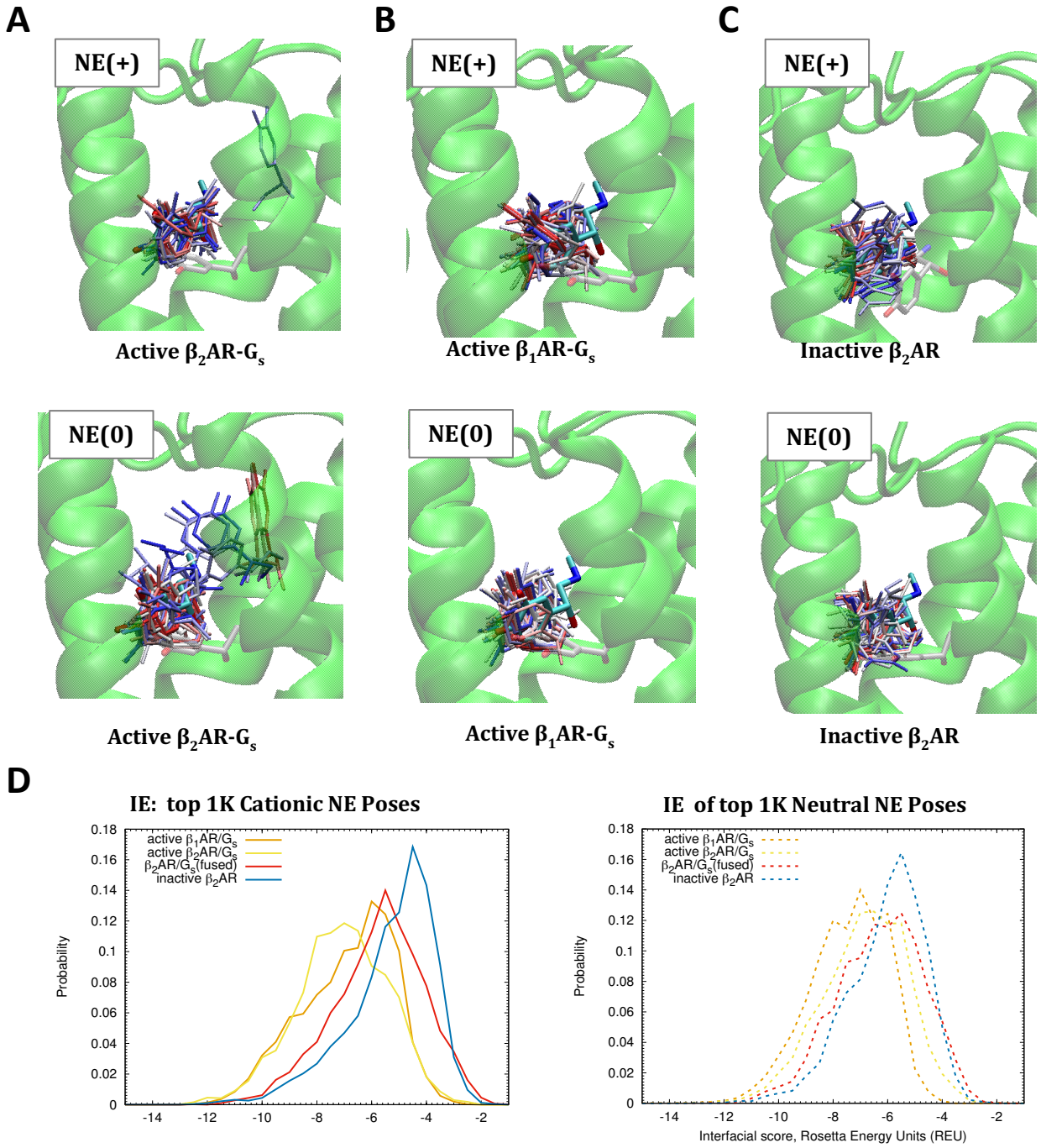

Figure 4.7. Docking of norepinephrine into RosettaCM-derived β_1AR and β_2AR models . (**A-C**) Top fifty poses of cationic (top) and neutral (bottom) norepinephrine (NE) into (**A**) active β_2AR-G_s, (**B**) active β_1AR-G_s, (**C**) inactive β_2AR homology models. Crystalized epinephrine of PDB 4LDO is depicted in cyan after alignment with the candidate models. (**D**) Probability distributions of Rosetta interfacial scores or interaction energies (IE)_for dockedcationic (left) or neutral (right) norepinephrine against active β_2AR, inactive β_2AR, and active β_1AR models as well as G_s-fused β_2AR structure PDB ID 6E67.

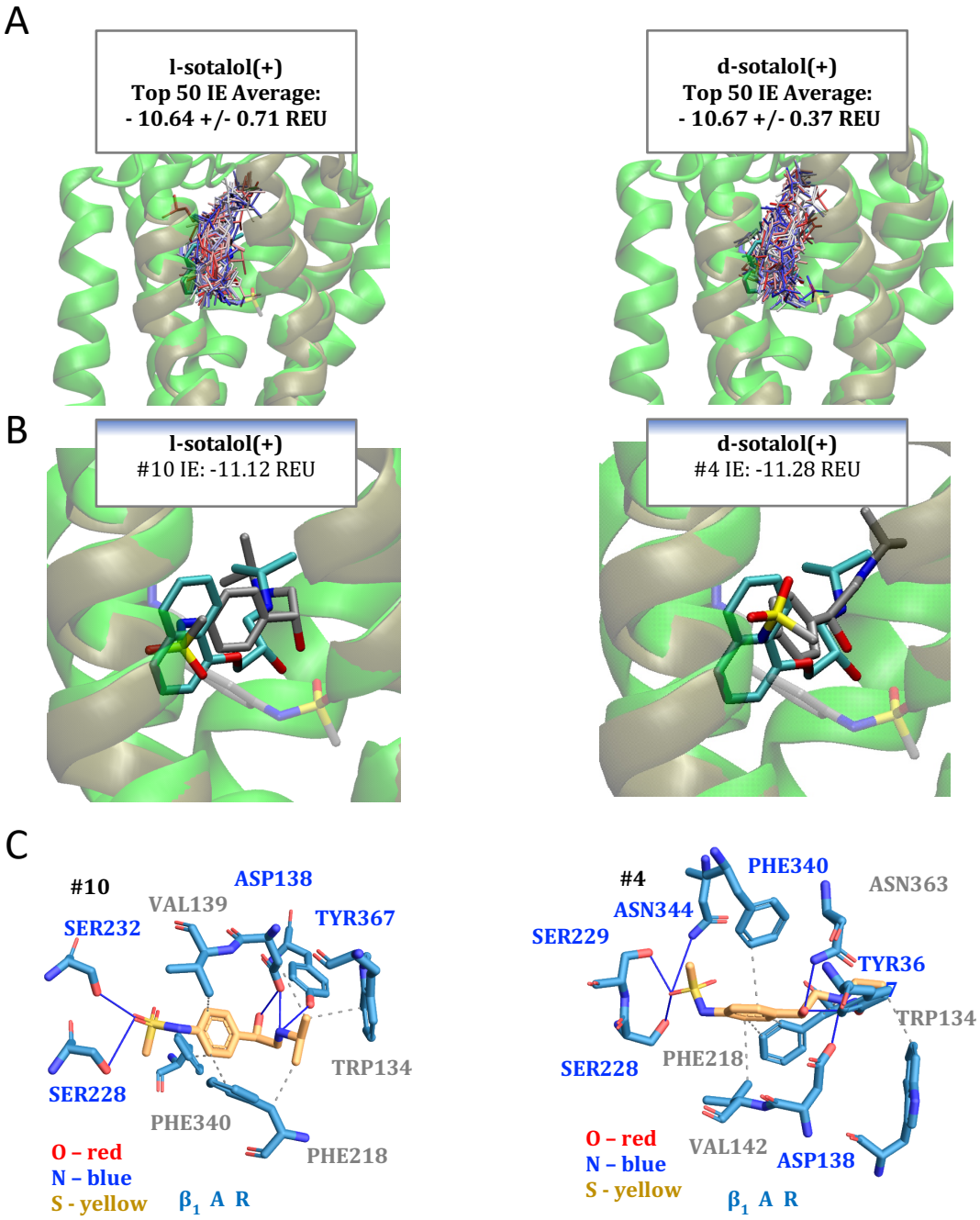

<u>Figure 4.8.</u> Docking of dl-sotalol stereoisomers into inactive human β $_1$AR homology model. **(A)** Top fifty poses of l-sotalol (left) and d-sotalol (right) colored from red to blue as first to fiftieth lowest energy. β_2AR crystal structure from PDB ID 6PS5 (tan) with bound cationic S-propranolol (cyan) is shown as a reference in panels A and B. (**B**) β_1AR protein model in green with tenth top-scoring pose of l-sotalol (left, gray) or forth scoring pose of d-sotalol (left, gray) and their respective initial positions (transparent). C) PLIP analysis showing interacting residues of tenth scoring pose of l-sotalol (left) and fourth scoring pose of d-sotalol (right). Nonpolar interactions are denoted by gray dashed lines, and hydrogen-bonding interactions by blue lines.

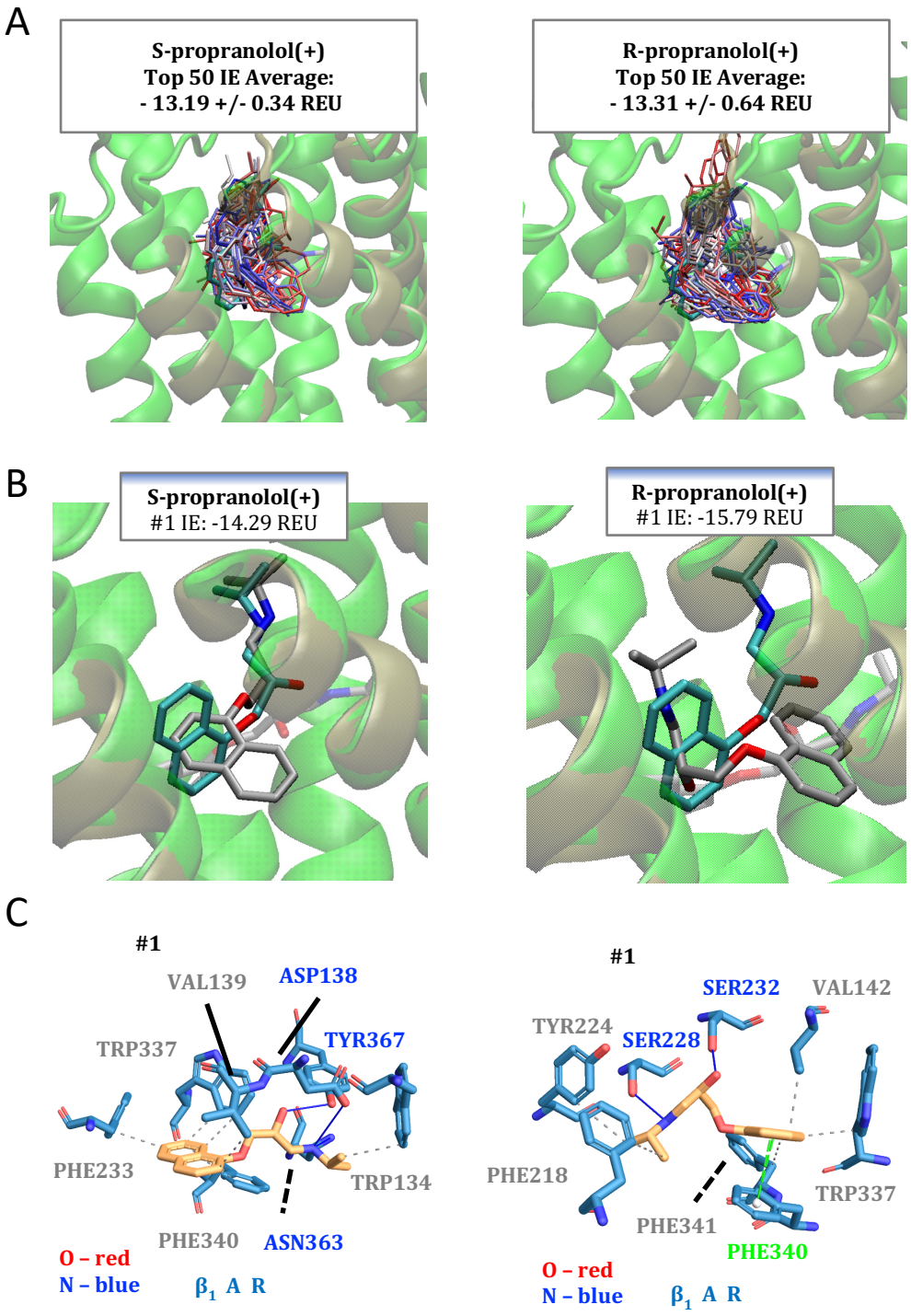

Figure 4.9. Docking of RS-propranolol stereoisomers into inactive Human β $_1$AR homology model. (A) Top fifty poses of S-propranolol (left) and R-propranolol (right) colored from red to blue as first to fiftieth lowest energy. Inactive β_2AR crystal structure from PDB ID 6PS5 (yellow) with bound cationic S-propranolol (cyan) is shown as a reference in panels A and B. **(B)** β_1AR protein model in green with top scoring pose of propranolol (solid gray) and initial position(transparent gray). **C**) PLIP analysis of interacting residues of top poses for S-propranolol (left) and R-propranolol (right). π-stacking interaction is denoted by green line, nonpolar interactions are denoted by gray dashed lines, and hydrogen-bonding interactions by blue lines.

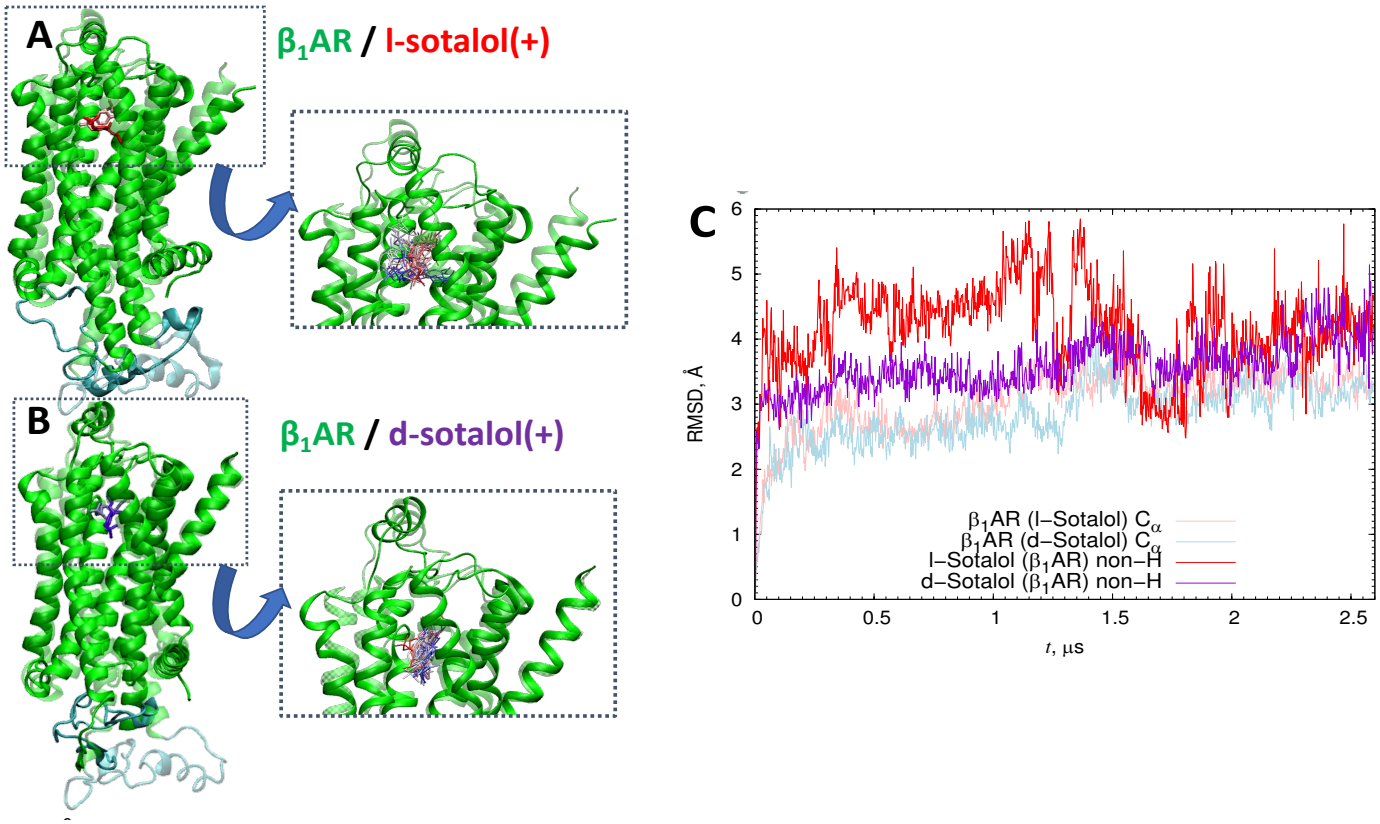

Figure 4.10. Multi-microsecond all-atom MD simulations of cationic d- and l-sotalol bound to inactive beta-1 adrenergic receptor homology model. Initial (transparent) and final (solid) positions of the receptor and drugs (**A**) cationic l-sotalol (red) and (**B**) d-sotalol (blue). Inset images are timeseries of individual poses of either drug taken from the 2.5 microsecond long simulations and are colored by from the beginning of the trajectory (red) to the final frame (blue). (**C**) Root-mean-square deviation (RMSD) of protein C_α atoms as well as either d- or l-sotalol non-hydrogen atoms from their initial docked positions with respect to the receptor.

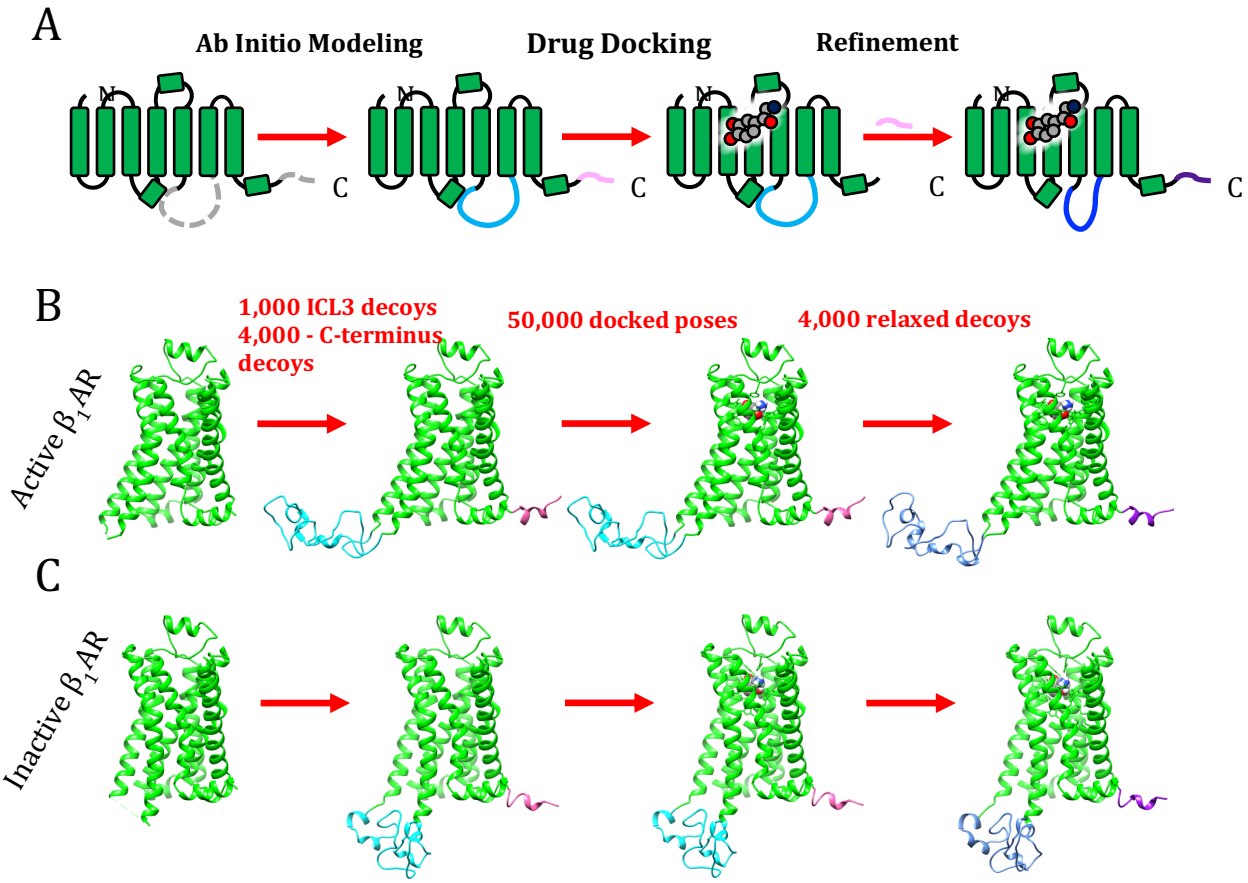

Figure 4.11. Loop modeling protocol using human β₁AR structural templates and Franklin2019 Rosetta membrane energy function. (**A**) This protocol uses kinematic loop closure to generate putative structures of the ICL3 and C-terminus of β₁AR and was applied for both (**B**) active and (**C**) inactive states of β₁AR

A

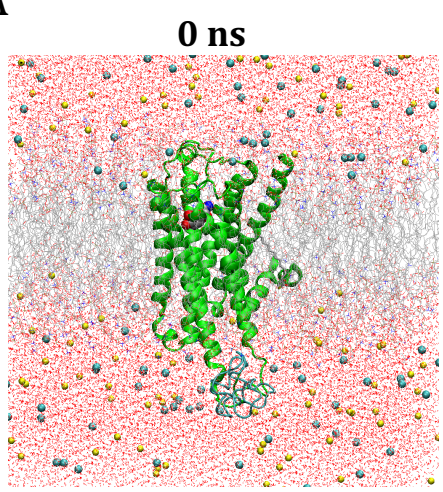

B

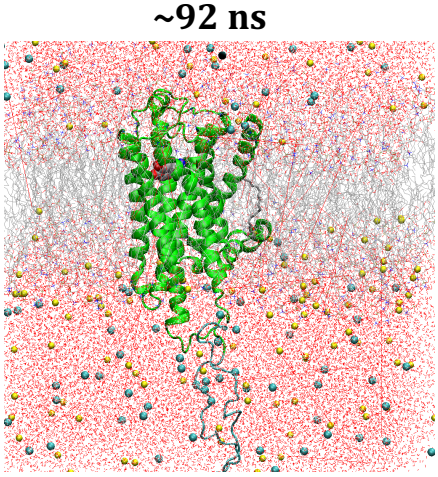

<u>Figure 4.12</u>. Active human β_1AR structural model MD stability test. All-atom MD simulation of the receptor bound to cationic norepinephrine embedded in a POPC/POPS lipid bilayer and hydrated by 0.15 M NaCl at 310 K and 1 atm, totaling ~187K atoms. NAMD 2.14 & 3.0 alpha (conducted on the Oracle cloud) was used to assess stability of the rebuilt model. Gradual protein harmonic restraints were applied for the first 42 ns. (**A**) Initial frame. **(B**) Final frame.

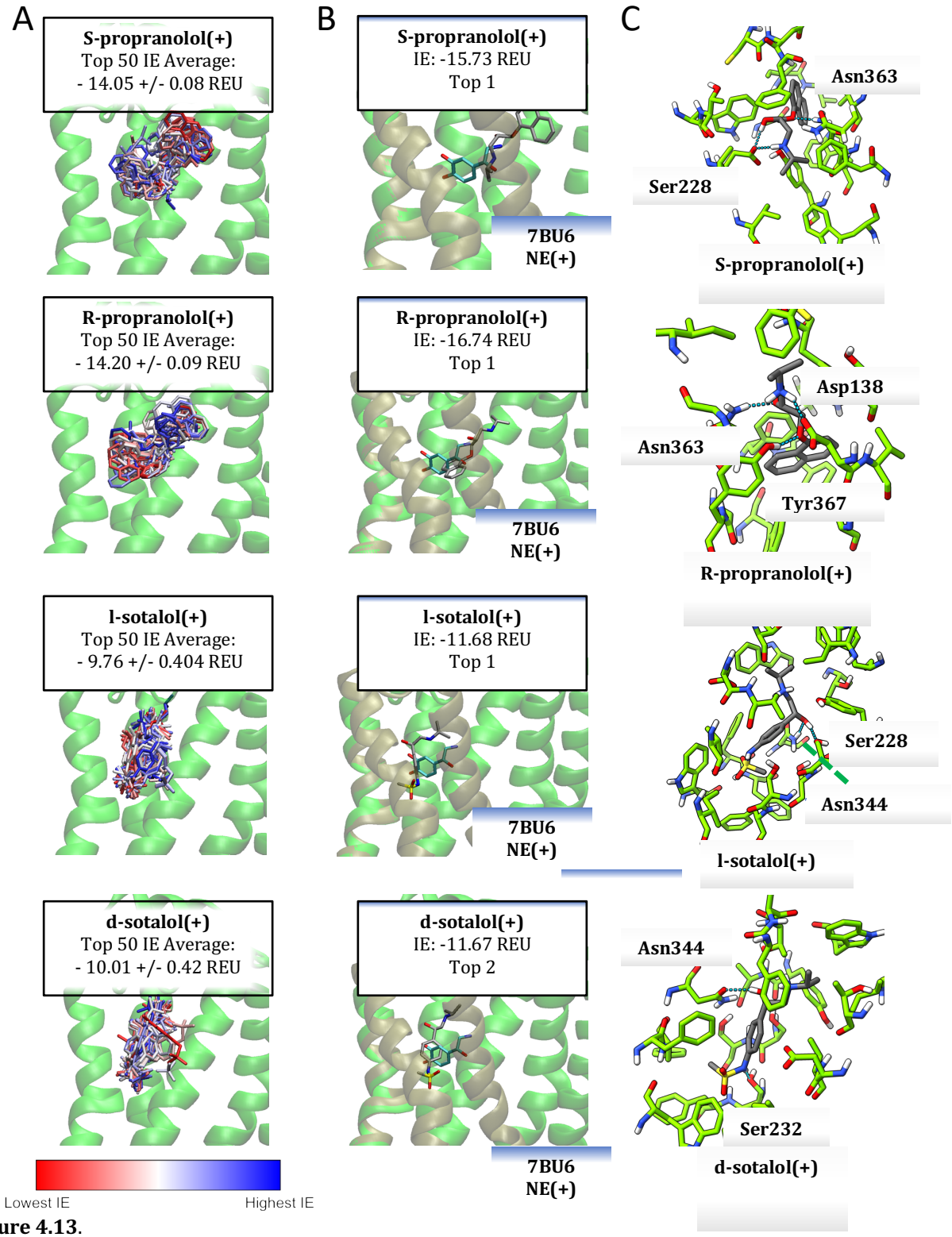
A
S-propranolol(+)
Top 50 IE Average:
- 14.05 +/- 0.08 REU
R-propranolol(+)
Top 50 IE Average:
- 14.20 +/- 0.09 REU
l-sotalol(+)
Top 50 IE Average:
- 9.76 +/- 0.404 REU
d-sotalol(+)
Top 50 IE Average:
- 10.01 +/- 0.42 REU
Lowest IE
Highest IE
B
S-propranolol(+)
IE: -15.73 REU
Top 1
7BU6
NE(+)
R-propranolol(+)
IE: -16.74 REU
Top 1
7BU6
NE(+)
l-sotalol(+)
IE: -11.68 REU
Top 1
7BU6
NE(+)
d-sotalol(+)
IE: -11.67 REU
Top 2
7BU6
NE(+)
C
Asn363
Ser228
S-propranolol(+)
Asp138
Asn363
Tyr367
R-propranolol(+)
Ser228
Asn344
l-sotalol(+)
Asn344
Ser232
d-sotalol(+)

Figure 4.13.

Figure 4.13. RosettaLigand docking stereoisomers of sotalol and propranolol into active state human beta-1 adrenergic receptor. (A) Top fifty poses of cationic drug docking into the active human β_1AR model colored from lowest interaction energy, IE (red, most favorable) to highest IE (blue, least favorable). (**B**) Candidate pose selected from top ten scoring poses compared to crystalline norepinephrine (NE) (cyan) as bound to the original template model (tan) from PDB ID:7BU6. (**C**) Contact analysis of the candidate pose for each drug with interacting residues labeled and H-bonds depicted by dotted blue lines.

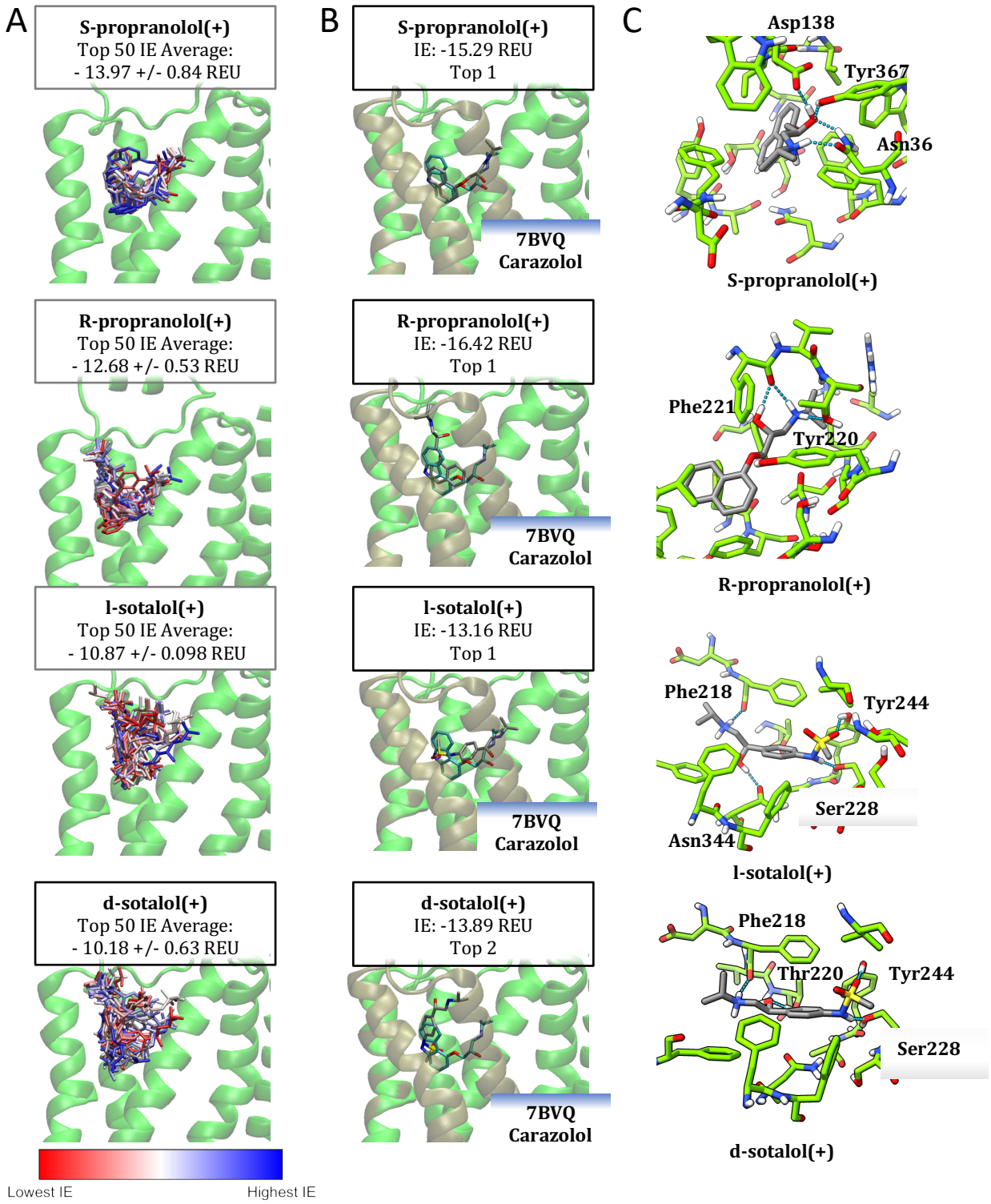
A
S-propranolol(+)
Top 50 IE Average:
- 13.97 +/- 0.84 REU
R-propranolol(+)
Top 50 IE Average:
- 12.68 +/- 0.53 REU
l-sotalol(+)
Top 50 IE Average:
- 10.87 +/- 0.098 REU
d-sotalol(+)
Top 50 IE Average:
- 10.18 +/- 0.63 REU
Lowest IE
Highest IE
B
S-propranolol(+)
IE: -15.29 REU
Top 1
7BVQ
Carazolol
R-propranolol(+)
IE: -16.42 REU
Top 1
7BVQ
Carazolol
l-sotalol(+)
IE: -13.16 REU
Top 1
7BVQ
Carazolol
d-sotalol(+)
IE: -13.89 REU
Top 2
7BVQ
Carazolol
C
Asp138
Tyr367
Asn36
S-propranolol(+)
Phe221
Tyr220
R-propranolol(+)
Phe218
Tyr244
Ser228
Asn344
l-sotalol(+)
Phe218
Thr220
Tyr244
Ser228
d-sotalol(+)

Figure 4.14.

Figure 4.14. RosettaLigand docking stereoisomers of sotalol and propranolol into inactive state human beta-1 adrenergic receptor. (A) Top fifty poses of cationic drug docking into the inactive human β_1AR model colored from lowest interaction energy, IE (red, most favorable) to highest IE (blue, least favorable. (**B**) Candidate pose selected from top ten scoring poses compared to crystalline carazolol, a betablocker, (cyan) as bound to the original template structural model (tan) PDB ID: 7BVQ. (**C**) Contact analysis of the candidate pose for each drug with interacting residues labeled and H-bonds depicted by dotted blue lines.

Chapter 5: Summary

In this work, we aimed to study the molecular determinants of the pro-arrhythmic drugs that bind multiple targets within the cardiac myocyte. To do so, we developed models of cardiac proteins in different states and characterized their interactions with drugs using Rosetta modeling and molecular dynamics simulations. We find that pairing extensive protein-modeling and drug docking procedures with multi-microsecond simulations may reproduce *in vivo* physiological phenomena. Using kinetic parameters derived from these techniques may inform functional scale models that describe cardiac electrophysiology. However, doing so requires careful consideration of the biological question. These findings contribute a larger collaborative effort to predict the cardiotoxic effect of drugs *in silico*.

In particular, we have described the process of characterizing state-dependent protein-ligand interactions in an effort to characterize computationally predicted and clinically-known drug-induced cardiotoxicities associated with a blockade of a cardiac potassium channel $K_V11.1$ encoded by human Ether-à-go-go-Related Gene (hERG). As a part of a multi-lab team, we developed an *in silico* multi-scale modeling pipeline to predict drug-induced cardiotoxicities in the form of cardiac arrhythmia markers at cell and tissue scales starting from drug chemistry and atomistic-level description of protein – drug interactions. In Chapter 2 we confirmed that our putative open-state hERG potassium channel model conducted potassium ions under applied transmembrane voltage. We identified protein geometries favoring ion permeation and validated that a non-conducting hERG channel S641A mutant was incapable of conduction when challenged with the same applied voltage as our the wild-type model and may represent inactivated state of the channel. An open state

hERG channel model we developed was instrumental in two applications of a multi-scale model of drug cardiac safety predictions. In one of our recently published papers[16] we successfully predicted different pro-arrhythmia outcomes of two hERG blocking drugs, dofetilide and moxifloxacin, by obtaining kinetics and affinities of their interactions with our open-state hERG channel model and using this information as functional kinetic model parameters to predict emergent pro-arrhythmia markers in cardiac tissue simulations. The manuscript presented in Chapter 3 and recently published as well[15] utilizes our open-state hERG channel model to emulate its blockade by d- and l-sotalol, two stereoisomers of beta-blocking, antiarrhythmic drug sotalol clinically prescribed as a racemic mixture. Here we demonstrate how molecular dynamics simulations may be used to characterize stereospecific sotalol interactions with the channel, and ultimately derive pertinent affinity and "on"/"off" rate values for use in functional scale models. In simulating blockade of racemic dl-, l- or d-sotalol against simulated tissue, it was determined that the beta-blocking affinity of l-sotalol is essential for reducing pro-arrhythmia risk in the racemic drug. However, the parameters used for beta-adrenergic receptor – drug interactions in that study were experimentally derived. This begs the question; can these findings be replicated using entirely MD-derived parameters for drug – receptor interactions? Addressing this question would be an immense boon to computational drug screening for predictive cardiac safety pharmacology.

Our work described in Chapter 4 marks the first step in incorporating simulated parameters from one drug against multiple protein targets to create a multi-scale model explicitly incorporating atomistic description of a multi-target block. Chapter 4 highlights structural

atomistic models made for type 1 and 2 beta-adrenergic receptors in both active and inactive (resting) states and their interactions with stereoisomeric beta blockers. Beta blockers are an ideal test case: they are typically racemic drugs with stereoisomers of different affinities. Being stereoisomers, they retain identical molecular composition, making experimental design simpler, and cross-system comparisons are readily obtainable. However, we find that docking simulations alone may not capture known differences in a binding modality that affect their affinity against receptor targets. As we broaden our study to simulate these drugs against hERG channel and other protein targets, we must acknowledge that multi-microsecond-long enhanced sampling MD simulations remain the most accurate means of computing energetics and kinetics. However, as the quantity of atomistic resolution structures of cardiac proteins is ever expanding, so does the potential for integrating such structures as targets in a multi-scale model of cardiac cell electrophysiology and signaling. However, consider comparing two drugs in two ionization states, as two stereoisomers, against two receptors occupying one of two conformational states of a single protein target. The number of simulations needed becomes exponentially large, especially if one desires converged simulation results and statistical power in distinguishing stereospecific, state preferences etc. Higher throughput methods are needed. New means of robust and fairly accurate determination of ligand binding energetics, such as all-atom MD simulation based fragment-based docking technique “Site Identification by Ligand Competitive Saturation” (SILCS) coupled with machine learning prediction optimizations may address these concerns[250, 251].

The domain of physics-based computational pharmacology is rapidly maturing. The problem of protein structure determination nears atomistic resolution with technologies like cryo-EM and its subsequent boon to deep learning. The next biophysical revolution will be dynamical. One may now download a model of literally any protein within minutes. Yet, how does one corroborate that model with biology? Making deductions based on the bell curve of big data is seductive. Yet, capturing a million images of an ion channel on a plate result in a very good 3D model of that ion channel – on a plate, absent the dynamics conferred by its native cellular environment. Drawing physiologically relevant conclusions from this wealth of structural information necessitates knowledge of pertinent biology, rigor in applying computational validation, and ultimately experimental corroboration. This work demonstrates a means of achieving this by characterizing the function and stability of novel protein structures using molecular dynamics and how to accurately create a model where one is absent. It outlines how to simulate drug interactions with these protein models, how to screen and select them, and how one might relate such data to the human health outcomes by means of multi-scale modeling through our collaborative work. In other words, it outlines a protocol for discernment when at the frontiers of structural biology.

6. References

1. Ferri, N., et al., *Drug attrition during pre-clinical and clinical development: understanding and managing drug-induced cardiotoxicity.* Pharmacol Ther, 2013. **138**(3): p. 470-84.
2. Onakpoya, I.J., C.J. Heneghan, and J.K. Aronson, *Post-marketing withdrawal of 462 medicinal products because of adverse drug reactions: a systematic review of the world literature.* BMC Medicine, 2016. **14**(1): p. 10.
3. Roden, D.M., *Drug-induced prolongation of the QT interval.* N Engl J Med, 2004. **350**(10): p. 1013-22.
4. Waldo, A.L., et al., *Effect of d-sotalol on mortality in patients with left ventricular dysfunction after recent and remote myocardial infarction. The SWORD Investigators. Survival With Oral d-Sotalol.* Lancet, 1996. **348**(9019): p. 7-12.
5. U.S. Department of Health and Human Services, F.a.D.A., Center for Drug Evaluation and Research (CDER), Center for Biologics Evaluation and Research (CBER). *Guidance for Industry*, in *E14 Clinical Evaluation of QT/QTc Interval Prolongation and Proarrhythmic Potential for Non-Antiarrhythmic Drugs*. 2005.
6. Li, M. and L.G. Ramos, *Drug-Induced QT Prolongation And Torsades de Pointes.* P & T : a peer-reviewed journal for formulary management, 2017. **42**(7): p. 473-477.
7. Drew, B.J., et al., *Prevention of torsade de pointes in hospital settings: a scientific statement from the American Heart Association and the American College of Cardiology Foundation.* Circulation, 2010. **121**(8): p. 1047-60.
8. Freemantle, N., et al., *beta Blockade after myocardial infarction: systematic review and meta regression analysis.* BMJ (Clinical research ed.), 1999. **318**(7200): p. 1730-1737.
9. James, P.A., et al., *2014 Evidence-Based Guideline for the Management of High Blood Pressure in Adults: Report From the Panel Members Appointed to the Eighth Joint National Committee (JNC 8).* JAMA, 2014. **311**(5): p. 507-520.
10. Goldberger, J.J., et al., *Autonomic Nervous System Dysfunction: JACC Focus Seminar.* Journal of the American College of Cardiology, 2019. **73**(10): p. 1189-1206.
11. Haverkamp, W., et al., *Efficacy and safety of d, l-sotalol in patients with ventricular tachycardia and in survivors of cardiac arrest.* Journal of the American College of Cardiology, 1997. **30**(2): p. 487-495.
12. Kawakami, K., et al., *Comparison of HERG channel blocking effects of various beta-blockers-- implication for clinical strategy.* British journal of pharmacology, 2006. **147**(6): p. 642-652.
13. Poole-Wilson, P.A., et al., *Comparison of carvedilol and metoprolol on clinical outcomes in patients with chronic heart failure in the Carvedilol Or Metoprolol European Trial (COMET): randomised controlled trial.* Lancet, 2003. **362**(9377): p. 7-13.
14. Colatsky, T., et al., *The Comprehensive in Vitro Proarrhythmia Assay (CiPA) initiative - Update on progress.* J Pharmacol Toxicol Methods, 2016. **81**: p. 15-20.
15. DeMarco, K.R., et al., *Molecular determinants of pro-arrhythmia proclivity of d- and l-sotalol via a multi-scale modeling pipeline.* Journal of Molecular and Cellular Cardiology, 2021.
16. Yang, P.C., et al., *A Computational Pipeline to Predict Cardiotoxicity:From the Atom to the Rhythm.* Circ Res, 2020. **126**: p. 947-964.

17. Waldo, A.L., et al., *Survival with oral d-sotalol in patients with left ventricular dysfunction after myocardial infarction: rationale, design, and methods (the SWORD trial).* Am J Cardiol, 1995. **75**(15): p. 1023-7.
18. Pratt, C.M., et al., *Mortality in the Survival With ORal D-sotalol (SWORD) trial: why did patients die?* Am J Cardiol, 1998. **81**(7): p. 869-76.
19. Yao, X., et al., *Propranolol inhibits the human ether-a-go-go-related gene potassium channels.* Eur J Pharmacol, 2005. **519**(3): p. 208-11.
20. Dupuis, D.S., D.A. Klaerke, and S.P. Olesen, *Effect of beta-adrenoceptor blockers on human ether-a-go-go-related gene (HERG) potassium channels.* Basic Clin Pharmacol Toxicol, 2005. **96**(2): p. 123-30.
21. Chatzidou, S., et al., *Propranolol Versus Metoprolol for Treatment of Electrical Storm in Patients With Implantable Cardioverter-Defibrillator.* J Am Coll Cardiol, 2018. **71**(17): p. 1897-1906.
22. Grandi, E. and C.M. Ripplinger, *Antiarrhythmic mechanisms of beta blocker therapy.* Pharmacological research, 2019. **146**: p. 104274-104274.
23. Bristow, M.R., *Treatment of chronic heart failure with β-adrenergic receptor antagonists: a convergence of receptor pharmacology and clinical cardiology.* Circ Res, 2011. **109**(10): p. 1176-94.
24. Lowes, B.D., et al., *Myocardial gene expression in dilated cardiomyopathy treated with beta-blocking agents.* N Engl J Med, 2002. **346**(18): p. 1357-65.
25. Lymperopoulos, A., G. Rengo, and W.J. Koch, *Adrenergic nervous system in heart failure: pathophysiology and therapy.* Circ Res, 2013. **113**(6): p. 739-53.
26. Wang, W. and R. MacKinnon, *Cryo-EM Structure of the Open Human Ether-a-go-go-Related K(+) Channel hERG.* Cell, 2017. **169**(3): p. 422-430 e10.
27. Vandenberg, J.I., et al., *hERG K(+) channels: structure, function, and clinical significance.* Physiol Rev, 2012. **92**(3): p. 1393-478.
28. Sanguinetti, M.C., et al., *A mechanistic link between an inherited and an acquired cardiac arrhythmia: HERG encodes the IKr potassium channel.* Cell, 1995. **81**(2): p. 299-307.
29. Smith, P.L., T. Baukrowitz, and G. Yellen, *The inward rectification mechanism of the HERG cardiac potassium channel.* Nature, 1996. **379**(6568): p. 833-6.
30. Priest, B., I.M. Bell, and M. Garcia, *Role of hERG potassium channel assays in drug development.* Channels, 2008. **2**(2): p. 87-93.
31. Ficker, E., et al., *Molecular Determinants of Dofetilide Block of HERG K^+ Channels.* Circulation Research, 1998. **82**(3): p. 386-395.
32. Durdagi, S., et al., *Modeling of open, closed, and open-inactivated states of the hERG1 channel: structural mechanisms of the state-dependent drug binding.* J Chem Inf Model, 2012. **52**(10): p. 2760-74.
33. Butler, A., et al., *An Update on the Structure of hERG.* Frontiers in Pharmacology, 2020. **10**(1572).
34. Zhang, M., J. Liu, and G.-N. Tseng, *Gating charges in the activation and inactivation processes of the HERG channel.* The Journal of general physiology, 2004. **124**(6): p. 703-718.

35. Zequn, Z. and L. Jiangfang, *Molecular Insights Into the Gating Kinetics of the Cardiac hERG Channel, Illuminated by Structure and Molecular Dynamics.* Frontiers in Pharmacology, 2021. **12**(1400).
36. Yarov-Yarovoy, V., et al., *Structural basis for gating charge movement in the voltage sensor of a sodium channel.* Proc Natl Acad Sci U S A, 2012. **109**(2): p. E93-102.
37. Priest, M.F., E.E. Lee, and F. Bezanilla, *Tracking the movement of discrete gating charges in a voltage-gated potassium channel.* Elife, 2021. **10**.
38. Zhou, Y. and R. MacKinnon, *The Occupancy of Ions in the K+ Selectivity Filter: Charge Balance and Coupling of Ion Binding to a Protein Conformational Change Underlie High Conduction Rates.* Journal of Molecular Biology, 2003. **333**(5): p. 965-975.
39. Flood, E., et al., *Atomistic Simulations of Membrane Ion Channel Conduction, Gating, and Modulation.* Chem Rev, 2019. **119**(13): p. 7737-7832.
40. Yarov-Yarovoy, V., J. Schonbrun, and D. Baker, *Multipass membrane protein structure prediction using Rosetta.* Proteins, 2006. **62**(4): p. 1010-25.
41. Barth, P., J. Schonbrun, and D. Baker, *Toward high-resolution prediction and design of transmembrane helical protein structures.* Proc Natl Acad Sci U S A, 2007. **104**(40): p. 15682-7.
42. Mandell, D.J., E.A. Coutsias, and T. Kortemme, *Sub-angstrom accuracy in protein loop reconstruction by robotics-inspired conformational sampling.* Nature Methods, 2009. **6**(8): p. 551-552.
43. Long, S.B., et al., *Atomic structure of a voltage-dependent K+ channel in a lipid membrane-like environment.* Nature, 2007. **450**(7168): p. 376-382.
44. Roux, B., *The Membrane Potential and its Representation by a Constant Electric Field in Computer Simulations.* Biophysical Journal, 2008. **95**(9): p. 4205-4216.
45. Brooks, B.R., et al., *CHARMM: a program for macromolecular energy, minimization, and dynamics calculations.* Journal of computational chemistry, 1983. **4**(2): p. 187-217.
46. Brooks, B.R., et al., *CHARMM: the biomolecular simulation program.* Journal of computational chemistry, 2009. **30**(10): p. 1545-1614.
47. Phillips, J.C., et al., *Scalable molecular dynamics with NAMD.* J Comput Chem, 2005. **26**(16): p. 1781-802.
48. Feller, S.E., et al., *Constant pressure molecular dynamics simulation: The Langevin piston method.* The Journal of Chemical Physics, 1995. **103**(11): p. 4613-4621.
49. Nosé, S., *A unified formulation of the constant temperature molecular dynamics methods.* The Journal of Chemical Physics, 1984. **81**(1): p. 511-519.
50. Hoover, W.G., *Canonical dynamics: Equilibrium phase-space distributions.* Physical Review A, 1985. **31**(3): p. 1695-1697.
51. Ryckaert, J.-P., G. Ciccotti, and H.J.C. Berendsen, *Numerical integration of the cartesian equations of motion of a system with constraints: molecular dynamics of n-alkanes.* Journal of Computational Physics, 1977. **23**(3): p. 327-341.
52. Darden, T., D. York, and L. Pedersen, *Particle mesh Ewald: An N·log(N) method for Ewald sums in large systems.* The Journal of Chemical Physics, 1993. **98**(12): p. 10089-10092.
53. Andre, I., et al., *Prediction of the structure of symmetrical protein assemblies.* Proc Natl Acad Sci U S A, 2007. **104**(45): p. 17656-61.

54. Kim, D.E., D. Chivian, and D. Baker, *Protein structure prediction and analysis using the Robetta server.* Nucleic acids research, 2004. **32**(Web Server issue): p. W526-W531.
55. Wang, C., P. Bradley, and D. Baker, *Protein-protein docking with backbone flexibility.* J Mol Biol, 2007. **373**(2): p. 503-19.
56. Bonneau, R., et al., *De Novo Prediction of Three-dimensional Structures for Major Protein Families.* Journal of Molecular Biology, 2002. **322**(1): p. 65-78.
57. Rohl, C.A., et al., *Protein structure prediction using Rosetta.* Methods Enzymol, 2004. **383**: p. 66-93.
58. Pettersen, E.F., et al., *UCSF Chimera--a visualization system for exploratory research and analysis.* J Comput Chem, 2004. **25**(13): p. 1605-12.
59. Huang, J. and A.D. MacKerell, Jr., *CHARMM36 all-atom additive protein force field: validation based on comparison to NMR data.* J Comput Chem, 2013. **34**(25): p. 2135-45.
60. Best, R.B., et al., *Optimization of the Additive CHARMM All-Atom Protein Force Field Targeting Improved Sampling of the Backbone ϕ, ψ and Side-Chain χ1 and χ2 Dihedral Angles.* Journal of Chemical Theory and Computation, 2012. **8**(9): p. 3257-3273.
61. Klauda, J.B., et al., *Update of the CHARMM All-Atom Additive Force Field for Lipids: Validation on Six Lipid Types.* The Journal of Physical Chemistry B, 2010. **114**(23): p. 7830-7843.
62. Jorgensen, W.L., et al., *Comparison of simple potential functions for simulating liquid water.* The Journal of Chemical Physics, 1983. **79**(2): p. 926-935.
63. Boiteux, C., et al., *Local anesthetic and antiepileptic drug access and binding to a bacterial voltage-gated sodium channel.* Proc Natl Acad Sci U S A, 2014. **111**(36): p. 13057-62.
64. Smart, O.S., et al., *HOLE: a program for the analysis of the pore dimensions of ion channel structural models.* Journal of molecular graphics, 1996. **14**(6): p. 354-360.
65. Shaw, D.E., et al., *Anton 2: Raising the bar for performance and programmability in a special-purpose molecular dynamics supercomputer.* Sc14: International Conference for High Performance Computing, Networking, Storage and Analysis, 2014: p. 41-53.
66. Jensen, M.Ø., et al., *Atomic-level simulation of current-voltage relationships in single-file ion channels.* The Journal of general physiology, 2013. **141**(5): p. 619-632.
67. Jo, S., T. Kim, and W. Im, *Automated builder and database of protein/membrane complexes for molecular dynamics simulations.* PloS one, 2007. **2**(9): p. e880-e880.
68. Heginbotham, L. and R. MacKinnon, *Conduction properties of the cloned Shaker K+ channel.* Biophys J, 1993. **65**(5): p. 2089-96.
69. Bian, J.S., et al., *S641 contributes HERG K+ channel inactivation.* Cell Biochem Biophys, 2004. **41**(1): p. 25-40.
70. Vijayvergiya, V., et al., *Single channel and ensemble hERG conductance measured in droplet bilayers.* Biomed Microdevices, 2015. **17**(1): p. 12.
71. Grissmer, S., et al., *Pharmacological characterization of five cloned voltage-gated K+ channels, types Kv1.1, 1.2, 1.3, 1.5, and 3.1, stably expressed in mammalian cell lines.* Mol Pharmacol, 1994. **45**(6): p. 1227-34.
72. Asai, T., et al., *Cryo-EM Structure of K(+)-Bound hERG Channel Complexed with the Blocker Astemizole.* Structure, 2021. **29**(3): p. 203-212.e4.

73. Miranda, W.E., et al., *Selectivity filter modalities and rapid inactivation of the hERG1 channel.* Proceedings of the National Academy of Sciences, 2020. **117**(6): p. 2795-2804.
74. Li, J., et al., *Mechanism of C-type inactivation in the hERG potassium channel.* Sci Adv, 2021. **7**(5).
75. Chhabra, N., M.L. Aseri, and D. Padmanabhan, *A review of drug isomerism and its significance.* International journal of applied and basic medical research, 2013. **3**(1): p. 16.
76. Gandhi, K., U. Shah, and S. Patel, *Drug Stereochemistry: A Prodigy For Pharmacology And Drug Development.* Current Drug Discovery Technologies, 2019. **16**: p. 00-00.
77. Smith, S.W., *Chiral toxicology: it's the same thing… only different.* Toxicological sciences, 2009. **110**(1): p. 4-30.
78. Sintra Grilo, L., P.-A. Carrupt, and H. Abriel, *Stereoselective inhibition of the hERG1 potassium channel.* Frontiers in Pharmacology, 2010. **1**: p. 137.
79. Eap, C.B., et al., *Stereoselective block of hERG channel by (S)-methadone and QT interval prolongation in CYP2B6 slow metabolizers.* Clinical Pharmacology & Therapeutics, 2007. **81**(5): p. 719-728.
80. Ansermot, N., et al., *Substitution of (R, S)-methadone by (R)-methadone: impact on QTc interval.* Archives of internal medicine, 2010. **170**(6): p. 529-536.
81. White, N.J., *Cardiotoxicity of antimalarial drugs.* The Lancet infectious diseases, 2007. **7**(8): p. 549-558.
82. Yan, M., et al., *Stereoselective blockage of quinidine and quinine in the hERG channel and the effect of their rescue potency on drug-induced hERG trafficking defect.* International journal of molecular sciences, 2016. **17**(10): p. 1648.
83. Calvey, T., *Isomerism and anaesthetic drugs.* Acta Anaesthesiologica Scandinavica, 1995. **39**: p. 83-90.
84. Graf, B.M., et al., *Differences in cardiotoxicity of bupivacaine and ropivacaine are the result of physicochemical and stereoselective properties.* Anesthesiology: The Journal of the American Society of Anesthesiologists, 2002. **96**(6): p. 1427-1434.
85. Zapata-Sudo, G., et al., *Is comparative cardiotoxicity of S (−) and R (+) bupivacaine related to enantiomer-selective inhibition of L-type Ca2+ channels?* Anesthesia & Analgesia, 2001. **92**(2): p. 496-501.
86. González, T., et al., *Effects of levobupivacaine, ropivacaine and bupivacaine on HERG channels: stereoselective bupivacaine block.* British journal of pharmacology, 2002. **137**(8): p. 1269-1279.
87. Siebrands, C.C., N. Schmitt, and P. Friederich, *Local Anesthetic Interaction with Human Ether-a-go-go–related Gene (HERG) ChannelsRole of Aromatic Amino Acids Y652 and F656.* Anesthesiology: The Journal of the American Society of Anesthesiologists, 2005. **103**(1): p. 102-112.
88. Wainer, I., *Stereoisomers in clinical oncology: why it is important to know what the right and left hands are doing.* Annals of oncology, 1993. **4**: p. S7-S13.
89. Nguyen, L.A., H. He, and C. Pham-Huy, *Chiral drugs: an overview.* International journal of biomedical science: IJBS, 2006. **2**(2): p. 85.
90. Kirschenbaum, H.L. and J.M. Rosenberg, *Clinical experience with sotalol in the treatment of cardiac arrhythmias.* Clin Ther, 1994. **16**(3): p. 346-64.

91. Hohnloser, S.H. and R.L. Woosley, *Sotalol.* New England Journal of Medicine, 1994. **331**(1): p. 31-38.
92. Kühlkamp, V., et al., *Efficacy and proarrhythmia with the use of d, l-sotalol for sustained ventricular tachyarrhythmias.* Journal of cardiovascular pharmacology, 1997. **29**(3): p. 373-381.
93. Kühlkamp, V., et al., *Suppression of sustained ventricular tachyarrhythmias: a comparison of d, l-sotalol with no antiarrhythmic drug treatment.* Journal of the American College of Cardiology, 1999. **33**(1): p. 46-52.
94. Pacifico, A., et al., *Prevention of implantable-defibrillator shocks by treatment with sotalol.* New England Journal of Medicine, 1999. **340**(24): p. 1855-1862.
95. Anderson, J.L. and E.N. Prystowsky, *Sotalol: an important new antiarrhythmic.* American heart journal, 1999. **137**(3): p. 388-409.
96. Singh, B.N., *Sotalol: current status and expanding indications.* Journal of cardiovascular pharmacology and therapeutics, 1999. **4**(1): p. 49-65.
97. *HIGHLIGHTS OF PRESCRIBING INFORMATION: Sotalol hydrochloride injection for intravenous use* 2009, U.S. Food and Drug Administration Silver Spring, MD, U.S.A.
98. Kerin, N.Z. and S. Jacob, *The efficacy of sotalol in preventing postoperative atrial fibrillation: a meta-analysis.* The American journal of medicine, 2011. **124**(9): p. 875. e1-875. e9.
99. Giardina, E.-G., *Therapeutic use and major side effects of sotalol*. 2018, UpToDate, Inc.
100. *Sotalol Hydrochloride*. 2018, Drugs.com.
101. Soyka, L.F., C. Wirtz, and R.B. Spangenberg, *Clinical safety profile of sotalol in patients with arrhythmias.* The American journal of cardiology, 1990. **65**(2): p. 74-81.
102. Falk, R.H., *Proarrhythmia in patients treated for atrial fibrillation or flutter.* Annals of internal medicine, 1992. **117**(2): p. 141-150.
103. MacNeil, D.J., R.O. Davies, and D. Deitchman, *Clinical safety profile of sotalol in the treatment of arrhythmias.* The American journal of cardiology, 1993. **72**(4): p. A44-A50.
104. Lehmann, M.H., et al., *Sex difference in risk of torsade de pointes with d, l-sotalol.* Circulation, 1996. **94**(10): p. 2535-2541.
105. Redfern, W., et al., *Relationships between preclinical cardiac electrophysiology, clinical QT interval prolongation and torsade de pointes for a broad range of drugs: evidence for a provisional safety margin in drug development.* Cardiovascular research, 2003. **58**(1): p. 32-45.
106. Shantsila, E., T. Watson, and G.Y. Lip, *Drug-induced QT-interval prolongation and proarrhythmic risk in the treatment of atrial arrhythmias.* Europace, 2007. **9**(suppl_4): p. iv37-iv44.
107. Kato, R., et al., *Electrophysiologic effects of the levo-and dextrorotatory isomers of sotalol in isolated cardiac muscle and their in vivo pharmacokinetics.* Journal of the American College of Cardiology, 1986. **7**(1): p. 116-125.
108. Gomoll, A.W. and M.J. Bartek, *Comparative β-blocking activities and electrophysiologic actions of racemic sotalol and its optical isomers in anesthetized dogs.* European journal of pharmacology, 1986. **132**(2-3): p. 123-135.
109. Funck-Brentano, C., et al., *A mechanism of D-(+)-sotalol effects on heart rate not related to beta-adrenoceptor antagonism.* Br J Clin Pharmacol, 1990. **30**(2): p. 195-202.

110. Touboul, P., *Electrophysiologic properties of sotalol and d-sotalol. A current view.* European heart journal, 1993. **14**(suppl_H): p. 24-29.
111. Funck-Brentano, C., *Pharmacokinetic and pharmacodynamic profiles of d-sotalol and d, l-sotalol.* European heart journal, 1993. **14**(suppl_H): p. 30-35.
112. Behr, E.R. and D. Roden, *Drug-induced arrhythmia: pharmacogenomic prescribing?* Eur Heart J, 2013. **34**(2): p. 89-95.
113. De Ponti, F., E. Poluzzi, and N. Montanaro, *QT-interval prolongation by non-cardiac drugs: lessons to be learned from recent experience.* Eur J Clin Pharmacol, 2000. **56**(1): p. 1-18.
114. Ruskin, J.N., *The cardiac arrhythmia suppression trial (CAST).* N Engl J Med, 1989. **321**(6): p. 386-8.
115. Trudeau, M.C., et al., *HERG, a human inward rectifier in the voltage-gated potassium channel family.* Science, 1995. **269**(5220): p. 92-5.
116. Sanguinetti, M.C. and M. Tristani-Firouzi, *hERG potassium channels and cardiac arrhythmia.* Nature, 2006. **440**(7083): p. 463-469.
117. Sager, P.T., et al., *Rechanneling the cardiac proarrhythmia safety paradigm: a meeting report from the Cardiac Safety Research Consortium.* American heart journal, 2014. **167**(3): p. 292-300.
118. Romero, L., et al., *In silico screening of the impact of hERG channel kinetic abnormalities on channel block and susceptibility to acquired long QT syndrome.* Journal of molecular and cellular cardiology, 2014. **72**: p. 126-137.
119. Fermini, B., et al., *A New Perspective in the Field of Cardiac Safety Testing through the Comprehensive In Vitro Proarrhythmia Assay Paradigm.* J Biomol Screen, 2016. **21**(1): p. 1-11.
120. Plazinska, A. and W. Plazinski, *Stereoselective binding of agonists to the β 2-adrenergic receptor: insights into molecular details and thermodynamics from molecular dynamics simulations.* Molecular BioSystems, 2017. **13**(5): p. 910-920.
121. Shen, Q., et al., *Stereoselective binding of chiral drugs to plasma proteins.* Acta Pharmacologica Sinica, 2013. **34**(8): p. 998-1006.
122. Moreno, J.D., et al., *A computational model to predict the effects of class I anti-arrhythmic drugs on ventricular rhythms.* Science translational medicine, 2011. **3**(98): p. 98ra83-98ra83.
123. Roberts, B.N., et al., *Computational approaches to understand cardiac electrophysiology and arrhythmias.* American Journal of Physiology-Heart and Circulatory Physiology, 2012. **303**(7): p. H766-H783.
124. Zhang, Y., et al., *Multi-scale modeling of the cardiovascular system: disease development, progression, and clinical intervention.* Annals of biomedical engineering, 2016. **44**(9): p. 2642-2660.
125. Clancy, C.E., et al., *Multiscale modeling in the clinic: drug design and development.* Annals of biomedical engineering, 2016. **44**(9): p. 2591-2610.
126. DeMarco, K.R., et al., *Digging into Lipid Membrane Permeation for Cardiac Ion Channel Blocker d-Sotalol with All-Atom Simulations.* Frontiers in pharmacology, 2018. **9**: p. 26-26.

127. DeMarco, K.R., et al., *Atomistic modeling towards predictive cardiotoxicity.* bioRxiv, 2019: p. 635441.
128. Numaguchi, H., et al., *Probing the interaction between inactivation gating and Dd-sotalol block of HERG.* Circ Res, 2000. **87**(11): p. 1012-8.
129. Jo, S., et al., *CHARMM-GUI: a web-based graphical user interface for CHARMM.* J Comput Chem, 2008. **29**(11): p. 1859-65.
130. Phillips, J.C., et al., *Scalable molecular dynamics with NAMD.* Journal of Computational Chemistry, 2005. **26**(16): p. 1781-1802.
131. Torrie, G.M. and J.P. Valleau, *Nonphysical sampling distributions in Monte Carlo free-energy estimation: Umbrella sampling.* Journal of Computational Physics, 1977. **23**(2): p. 187-199.
132. Jiang, W., et al., *Calculation of Free Energy Landscape in Multi-Dimensions with Hamiltonian-Exchange Umbrella Sampling on Petascale Supercomputer.* Journal of Chemical Theory and Computation, 2012. **8**(11): p. 4672-4680.
133. Perrin, M.J., et al., *Drug binding to the inactivated state is necessary but not sufficient for high-affinity binding to human ether-a-go-go-related gene channels.* Mol Pharmacol, 2008. **74**(5): p. 1443-52.
134. Duff, H.J., Z.P. Feng, and R.S. Sheldon, *High- and low-affinity sites for [3H]dofetilide binding to guinea pig myocytes.* Circ Res, 1995. **77**(4): p. 718-25.
135. O'Hara, T., et al., *Simulation of the undiseased human cardiac ventricular action potential: model formulation and experimental validation.* PLoS Comput Biol, 2011. **7**(5): p. e1002061.
136. Funck-Brentano, C., et al., *Rate dependence of sotalol-induced prolongation of ventricular repolarization during exercise in humans.* Circulation, 1991. **83**(2): p. 536-45.
137. Sheldrick, G.M., *A short history of SHELX.* Acta Crystallographica, Section A, 2008. **64**: p. 112-121.
138. Zhou, Z., et al., *Properties of HERG channels stably expressed in HEK 293 cells studied at physiological temperature.* Biophysical journal, 1998. **74**(1): p. 230-241.
139. Hamill, O.P., et al., *Improved patch-clamp techniques for high-resolution current recording from cells and cell-free membrane patches.* Pflügers Archiv, 1981. **391**(2): p. 85-100.
140. Lees-Miller, J.P., et al., *Molecular determinant of high-affinity dofetilide binding toHERG1 expressed in Xenopus oocytes: involvement of S6 sites.* Molecular pharmacology, 2000. **57**(2): p. 367-374.
141. Mitcheson, J.S., et al., *A structural basis for drug-induced long QT syndrome.* Proc Natl Acad Sci U S A, 2000. **97**(22): p. 12329-33.
142. Perry, M., M. Sanguinetti, and J. Mitcheson, *Symposium review: Revealing the structural basis of action of hERG potassium channel activators and blockers.* The Journal of physiology, 2010. **588**(17): p. 3157-3167.
143. Dickson, C.J., C. Velez-Vega, and J.S. Duca, *Revealing molecular determinants of hERG blocker and activator binding.* Journal of chemical information and modeling, 2019. **60**(1): p. 192-203.

144. Raju, S., et al., *Exploring volatile general anesthetic binding to a closed membrane-bound bacterial voltage-gated sodium channel via computation.* PLoS Comput Biol, 2013. **9**(6): p. e1003090.
145. Martin, L.J. and B. Corry, *Locating the route of entry and binding sites of benzocaine and phenytoin in a bacterial voltage gated sodium channel.* PLoS Comput Biol, 2014. **10**(7): p. e1003688.
146. Nguyen, P.T., et al., *Structural basis for antiarrhythmic drug interactions with the human cardiac sodium channel.* Proc Natl Acad Sci U S A, 2019. **116**(8): p. 2945-2954.
147. Perissinotti, L., et al., *The pore-lipid interface: role of amino-Acid determinants of lipophilic access by ivabradine to the hERG1 pore domain.* Molecular Pharmacology, 2019. **96**(2): p. 259-271.
148. Kudaibergenova, M., et al., *Allosteric Coupling Between Drug Binding and the Aromatic Cassette in the Pore Domain of the hERG1 Channel: Implications for a State-Dependent Blockade.* Frontiers in pharmacology, 2020. **11**: p. 914.
149. Yu, Z., I.J. AP, and L.H. Heitman, *Kv 11.1 (hERG)-induced cardiotoxicity: a molecular insight from a binding kinetics study of prototypical Kv 11.1 (hERG) inhibitors.* Br J Pharmacol, 2015. **172**(3): p. 940-55.
150. Zhang, Y.H., C.E. Dempsey, and J.C. Hancox, *The Basis for Low-affinity hERG Potassium Channel Block by Sotalol.* Journal of pharmacology & pharmacotherapeutics, 2017. **8**(3): p. 130-131.
151. Negami, T., et al., *Calculation of absolute binding free energies between the hERG channel and structurally diverse drugs.* Scientific reports, 2019. **9**(1): p. 1-12.
152. Schulz, M. and A. Schmoldt, *Therapeutic and toxic blood concentrations of more than 800 drugs and other xenobiotics.* Die Pharmazie-An International Journal of Pharmaceutical Sciences, 2003. **58**(7): p. 447-474.
153. Qu, Z., et al., *Multi-scale modeling in biology: how to bridge the gaps between scales?* Progress in biophysics and molecular biology, 2011. **107**(1): p. 21-31.
154. Walpole, J., J.A. Papin, and S.M. Peirce, *Multiscale computational models of complex biological systems.* Annual review of biomedical engineering, 2013. **15**: p. 137-154.
155. Yarov-Yarovoy, V., T.W. Allen, and C.E. Clancy, *Computational models for predictive cardiac ion channel pharmacology.* Drug Discovery Today: Disease Models, 2014. **14**: p. 3-10.
156. Yang, P.C., et al., *In silico prediction of drug therapy in catecholaminergic polymorphic ventricular tachycardia.* J Physiol, 2016. **594**(3): p. 567-93.
157. Yang, P.C., et al., *A multiscale computational modelling approach predicts mechanisms of female sex risk in the setting of arousal-induced arrhythmias.* J Physiol, 2017. **595**(14): p. 4695-4723.
158. Yabek, S.M., et al., *Cellular electrophysiologic responses of isolated neonatal and adult cardiac fibers to d-sotalol.* Journal of the American College of Cardiology, 1988. **11**(5): p. 1094-1099.
159. Advani, S.V. and B.N. Singh, *Pharmacodynamic, pharmacokinetic and antiarrhythmic properties of d-sotalol, the dextro-isomer of sotalol.* Drugs, 1995. **49**(5): p. 664-679.

160. Singh, B.N., *Electrophysiologic basis for the antiarrhythmic actions of sotalol and comparison with other agents.* The American journal of cardiology, 1993. **72**(4): p. A8-A18.
161. Hsieh, Y.-C., et al., *d, l-Sotalol at therapeutic concentrations facilitates the occurrence of long-lasting non-stationary reentry during ventricular fibrillation in isolated rabbit hearts.* Circulation Journal, 2009. **73**(1): p. 39-47.
162. Waldegger, S., et al., *Effect of verapamil enantiomers and metabolites on cardiac K+ channels expressed in Xenopus oocytes.* Cellular Physiology and Biochemistry, 1999. **9**(2): p. 81-89.
163. Yang, I.C.-H., et al., *Stereoselective interactions of the enantiomers of chromanol 293B with human voltage-gated potassium channels.* Journal of Pharmacology and Experimental Therapeutics, 2000. **294**(3): p. 955-962.
164. Carmeliet, E., *Electrophysiologic and voltage clamp analysis of the effects of sotalol on isolated cardiac muscle and Purkinje fibers.* Journal of Pharmacology and Experimental Therapeutics, 1985. **232**(3): p. 817-825.
165. Reid, J., et al., *(+)-Sotalol causes significant occupation of β-adrenoceptors at concentrations that prolong cardiac repolarization.* Naunyn-Schmiedeberg's archives of pharmacology, 1990. **341**(3): p. 215-220.
166. Groh, W.J., et al., *β-Adrenergic blocking property of dl-sotalol maintains class III efficacy in guinea pig ventricular muscle after isoproterenol.* Circulation, 1995. **91**(2): p. 262-264.
167. Dubois, V., et al., *Pharmacokinetic–pharmacodynamic modelling of drug-induced QTc interval prolongation in man: prediction from in vitro human ether-à-go-go-related gene binding and functional inhibition assays and conscious dog studies.* British journal of pharmacology, 2016. **173**(19): p. 2819-2832.
168. Mo, Z.-L., et al., *Effect of compound plate composition on measurement of hERG current IC50 using PatchXpress.* Journal of pharmacological and toxicological methods, 2009. **60**(1): p. 39-44.
169. Kramer, J., et al., *MICE models: superior to the HERG model in predicting Torsade de Pointes.* Scientific reports, 2013. **3**(1): p. 1-7.
170. Ridder, B.J., et al., *A systematic strategy for estimating hERG block potency and its implications in a new cardiac safety paradigm.* Toxicology and Applied Pharmacology, 2020: p. 114961.
171. Crumb Jr, W.J., et al., *An evaluation of 30 clinical drugs against the comprehensive in vitro proarrhythmia assay (CiPA) proposed ion channel panel.* Journal of pharmacological and toxicological methods, 2016. **81**: p. 251-262.
172. Abi-Gerges, N., et al., *hERG subunit composition determines differential drug sensitivity.* British journal of pharmacology, 2011. **164**(2b): p. 419-432.
173. Männikkö, R., et al., *Pharmacological and electrophysiological characterization of nine, single nucleotide polymorphisms of the hERG-encoded potassium channel.* British journal of pharmacology, 2010. **159**(1): p. 102-114.
174. Kirsch, G.E., et al., *Variability in the measurement of hERG potassium channel inhibition: effects of temperature and stimulus pattern.* Journal of pharmacological and toxicological methods, 2004. **50**(2): p. 93-101.

175. Orvos, P., et al., *Evaluation of Possible Proarrhythmic Potency: Comparison of the Effect of Dofetilide, Cisapride, Sotalol, Terfenadine, and Verapamil on hERG and Native I Kr Currents and on Cardiac Action Potential.* Toxicological Sciences, 2019. **168**(2): p. 365-380.
176. Davie, C., et al., *Comparative pharmacology of guinea pig cardiac myocyte and cloned hERG (IKr) channel.* Journal of cardiovascular electrophysiology, 2004. **15**(11): p. 1302-1309.
177. Zhou, Q., et al., *Identification of I Kr kinetics and drug binding in native myocytes.* Annals of biomedical engineering, 2009. **37**(7): p. 1294-1309.
178. Fiset, C., et al., *[3H] Dofetilide binding: biological models that manifest solely the high or the low affinity binding site.* Journal of molecular and cellular cardiology, 1996. **28**(5): p. 1085-1096.
179. Sube, R. and E.A. Ertel, *Cardiomyocytes Derived from Human Induced Pluripotent Stem Cells: An In-Vitro Model to Predict Cardiac Effects of Drugs.* Journal of Biomedical Science and Engineering, 2017. **10**(11): p. 527.
180. Sala, L., M. Bellin, and C.L. Mummery, *Integrating cardiomyocytes from human pluripotent stem cells in safety pharmacology: has the time come?* British journal of pharmacology, 2017. **174**(21): p. 3749-3765.
181. Doss, M.X. and A. Sachinidis, *Current challenges of iPSC-based disease modeling and therapeutic implications.* Cells, 2019. **8**(5): p. 403.
182. Perissinotti, L.L., et al., *Determinants of isoform-specific gating kinetics of hERG1 channel: combined experimental and simulation study.* Frontiers in physiology, 2018. **9**: p. 207.
183. Abbott, G.W., et al., *MiRP1 forms IKr potassium channels with HERG and is associated with cardiac arrhythmia.* Cell, 1999. **97**(2): p. 175-187.
184. Mirams, G.R., et al., *Prediction of thorough QT study results using action potential simulations based on ion channel screens.* Journal of pharmacological and toxicological methods, 2014. **70**(3): p. 246-254.
185. Lancaster, M.C. and E. Sobie, *Improved prediction of drug-induced Torsades de Pointes through simulations of dynamics and machine learning algorithms.* Clinical Pharmacology & Therapeutics, 2016. **100**(4): p. 371-379.
186. Britton, O.J., et al., *Quantitative comparison of effects of dofetilide, sotalol, quinidine, and verapamil between human ex vivo trabeculae and in silico ventricular models incorporating inter-individual action potential variability.* Frontiers in physiology, 2017. **8**: p. 597.
187. Dutta, S., et al., *Optimization of an in silico cardiac cell model for proarrhythmia risk assessment.* Frontiers in Physiology, 2017. **8**: p. 616.
188. Grandi, E., F.S. Pasqualini, and D.M. Bers, *A novel computational model of the human ventricular action potential and Ca transient.* Journal of molecular and cellular cardiology, 2010. **48**(1): p. 112-121.
189. Ten Tusscher, K.H. and A.V. Panfilov, *Cell model for efficient simulation of wave propagation in human ventricular tissue under normal and pathological conditions.* Physics in Medicine & Biology, 2006. **51**(23): p. 6141.

190. Cuello, L.G., et al., *Structural mechanism of C-type inactivation in K+ channels.* Nature, 2010. **466**(7303): p. 203-208.
191. Cuello, L.G., D.M. Cortes, and E. Perozo, *The gating cycle of a K+ channel at atomic resolution.* Elife, 2017. **6**: p. e28032.
192. Pau, V., et al., *Crystal structure of an inactivated mutant mammalian voltage-gated K+ channel.* Nature structural & molecular biology, 2017. **24**(10): p. 857.
193. Matthies, D., et al., *Single-particle cryo-EM structure of a voltage-activated potassium channel in lipid nanodiscs.* Elife, 2018. **7**: p. e37558.
194. Xu, X., et al., *Binding pathway determines norepinephrine selectivity for the human β 1 AR over β 2 AR.* Cell Research, 2020: p. 1-11.
195. Amanfu, R.K. and J.J. Saucerman, *Modeling the effects of β1-adrenergic receptor blockers and polymorphisms on cardiac myocyte Ca2+ handling.* Molecular pharmacology, 2014. **86**(2): p. 222-230.
196. Cannon, W.B., *Bodily Changes in Pain, Hunger, Fear, And Rage: An Account of Recent Searches into the Function of Emotional Excitement*. 1922, New York and London: D. Appleton and Company.
197. McCorry, L.K., *Physiology of the autonomic nervous system.* Am J Pharm Educ, 2007. **71**(4): p. 78.
198. Alshak, M.N. and M.D. J, *Neuroanatomy, Sympathetic Nervous System*, in *StatPearls*. 2021, StatPearls Publishing
Copyright © 2022, StatPearls Publishing LLC.: Treasure Island (FL).
199. Ripplinger, C.M., S.F. Noujaim, and D. Linz, *The nervous heart.* Prog Biophys Mol Biol, 2016. **120**(1-3): p. 199-209.
200. Bylund, D.B., et al., *International Union of Pharmacology nomenclature of adrenoceptors.* Pharmacol Rev, 1994. **46**(2): p. 121-36.
201. Woo, A.Y.H. and R.-p. Xiao, *β-Adrenergic receptor subtype signaling in heart: from bench to bedside.* Acta pharmacologica Sinica, 2012. **33**(3): p. 335-341.
202. Wachter, S.B. and E.M. Gilbert, *Beta-adrenergic receptors, from their discovery and characterization through their manipulation to beneficial clinical application.* Cardiology, 2012. **122**(2): p. 104-12.
203. Baker, J.G., *The selectivity of beta-adrenoceptor antagonists at the human beta1, beta2 and beta3 adrenoceptors.* Br J Pharmacol, 2005. **144**(3): p. 317-22.
204. Liu, X., et al., *Distribution and relative expression of vasoactive receptors on arteries.* Scientific Reports, 2020. **10**(1): p. 15383.
205. Srinivasan, A.V., *Propranolol: A 50-Year Historical Perspective.* Annals of Indian Academy of Neurology, 2019. **22**(1): p. 21-26.
206. do Vale, G.T., et al., *Three Generations of β-blockers: History, Class Differences and Clinical Applicability.* Curr Hypertens Rev, 2019. **15**(1): p. 22-31.
207. Mehvar, R. and D.R. Brocks, *Stereospecific pharmacokinetics and pharmacodynamics of beta-adrenergic blockers in humans.* J Pharm Pharm Sci, 2001. **4**(2): p. 185-200.
208. Ring, A.M., et al., *Adrenaline-activated structure of β2-adrenoceptor stabilized by an engineered nanobody.* Nature, 2013. **502**(7472): p. 575-579.
209. Rasmussen, S.G., et al., *Crystal structure of the human beta2 adrenergic G-protein-coupled receptor.* Nature, 2007. **450**(7168): p. 383-7.

210. Lomize, M.A., et al., *OPM database and PPM web server: resources for positioning of proteins in membranes.* Nucleic acids research, 2012. **40**(Database issue): p. D370-D376.
211. Canutescu, A.A. and R.L. Dunbrack, Jr., *Cyclic coordinate descent: A robotics algorithm for protein loop closure.* Protein Sci, 2003. **12**(5): p. 963-72.
212. Consortium, T.U., *UniProt: the universal protein knowledgebase in 2021.* Nucleic Acids Research, 2020. **49**(D1): p. D480-D489.
213. Waterhouse, A.M., et al., *Jalview Version 2—a multiple sequence alignment editor and analysis workbench.* Bioinformatics, 2009. **25**(9): p. 1189-1191.
214. Alford, R.F., et al., *Protein Structure Prediction and Design in a Biologically Realistic Implicit Membrane.* Biophys J, 2020. **118**(8): p. 2042-2055.
215. Song, Y., et al., *High-resolution comparative modeling with RosettaCM.* Structure, 2013. **21**(10): p. 1735-42.
216. Alford, R.F., et al., *The Rosetta All-Atom Energy Function for Macromolecular Modeling and Design.* J Chem Theory Comput, 2017. **13**(6): p. 3031-3048.
217. Conway, P., et al., *Relaxation of backbone bond geometry improves protein energy landscape modeling.* Protein Sci, 2014. **23**(1): p. 47-55.
218. Warne, T., et al., *Molecular basis for high-affinity agonist binding in GPCRs.* Science, 2019. **364**(6442): p. 775-778.
219. Sievers, F., et al., *Fast, scalable generation of high-quality protein multiple sequence alignments using Clustal Omega.* Molecular Systems Biology, 2011. **7**(1): p. 539.
220. Madeira, F., et al., *Search and sequence analysis tools services from EMBL-EBI in 2022.* Nucleic Acids Research, 2022.
221. Alford, R.F., et al., *Protein Structure Prediction and Design in a Biologically Realistic Implicit Membrane.* Biophysical Journal, 2020. **118**(8): p. 2042-2055.
222. Warne, T., et al., *The structural basis for agonist and partial agonist action on a β(1)-adrenergic receptor.* Nature, 2011. **469**(7329): p. 241-4.
223. Xu, X., et al., *Binding pathway determines norepinephrine selectivity for the human β(1)AR over β(2)AR.* Cell Res, 2021. **31**(5): p. 569-579.
224. Meiler, J. and D. Baker, *ROSETTALIGAND: protein-small molecule docking with full side-chain flexibility.* Proteins, 2006. **65**(3): p. 538-48.
225. Davis, I.W. and D. Baker, *RosettaLigand docking with full ligand and receptor flexibility.* J Mol Biol, 2009. **385**(2): p. 381-92.
226. Davis, I.W., et al., *Blind docking of pharmaceutically relevant compounds using RosettaLigand.* Protein Sci, 2009. **18**(9): p. 1998-2002.
227. Hawkins, P.C., et al., *Conformer generation with OMEGA: algorithm and validation using high quality structures from the Protein Databank and Cambridge Structural Database.* J Chem Inf Model, 2010. **50**(4): p. 572-84.
228. Salentin, S., et al., *PLIP: fully automated protein–ligand interaction profiler.* Nucleic Acids Research, 2015. **43**(W1): p. W443-W447.
229. Jo, S., et al., *CHARMM-GUI Membrane Builder for Mixed Bilayers and Its Application to Yeast Membranes.* Biophysical Journal, 2009. **97**(1): p. 50-58.
230. Lee, J., et al., *CHARMM-GUI Input Generator for NAMD, GROMACS, AMBER, OpenMM, and CHARMM/OpenMM Simulations Using the CHARMM36 Additive Force Field.* Journal of Chemical Theory and Computation, 2016. **12**(1): p. 405-413.

231. Wu, E.L., et al., *CHARMM-GUI Membrane Builder toward realistic biological membrane simulations.* J Comput Chem, 2014. **35**(27): p. 1997-2004.
232. Lee, J., et al., *CHARMM-GUI Membrane Builder for Complex Biological Membrane Simulations with Glycolipids and Lipoglycans.* J Chem Theory Comput, 2019. **15**(1): p. 775-786.
233. Dror, R.O., et al., *Structural basis for nucleotide exchange in heterotrimeric G proteins.* Science, 2015. **348**(6241): p. 1361-1365.
234. Vanommeslaeghe, K., et al., *CHARMM general force field: A force field for drug-like molecules compatible with the CHARMM all-atom additive biological force fields.* J Comput Chem, 2010. **31**(4): p. 671-90.
235. Yu, W., et al., *Extension of the CHARMM General Force Field to sulfonyl-containing compounds and its utility in biomolecular simulations.* J Comput Chem, 2012. **33**(31): p. 2451-68.
236. Frisch, M.J., et al., *Gaussian 98*. 1998.
237. Mayne, C.G., et al., *Rapid parameterization of small molecules using the Force Field Toolkit.* J Comput Chem, 2013. **34**(32): p. 2757-70.
238. Humphrey, W., A. Dalke, and K. Schulten, *VMD: visual molecular dynamics.* J. Mol. Graphics, 1996. **14**(1): p. 33.
239. Shaw, D.E., et al., *Millisecond-scale molecular dynamics simulations on Anton*, in *Proceedings of the Conference on High Performance Computing Networking, Storage and Analysis*. 2009, Association for Computing Machinery: Portland, Oregon. p. Article 65.
240. Shaw, D.E., et al., *Atomic-Level Characterization of the Structural Dynamics of Proteins.* Science, 2010. **330**(6002): p. 341-346.
241. Ishchenko, A., et al., *Toward G protein-coupled receptor structure-based drug design using X-ray lasers.* IUCrJ, 2019. **6**(Pt 6): p. 1106-1119.
242. Ballesteros, J.A. and H. Weinstein, *Integrated methods for the construction of three-dimensional models and computational probing of structure-function relations in G protein-coupled receptors*, in *Methods in Neurosciences*, S.C. Sealfon, Editor. 1995, Academic Press. p. 366-428.
243. Wu, Y., L. Zeng, and S. Zhao, *Ligands of Adrenergic Receptors: A Structural Point of View.* Biomolecules, 2021. **11**(7).
244. Dror, R.O., et al., *Pathway and mechanism of drug binding to G-protein-coupled receptors.* Proceedings of the National Academy of Sciences, 2011. **108**(32): p. 13118-13123.
245. Hedderich, J.B., et al., *The pocketome of G-protein-coupled receptors reveals previously untargeted allosteric sites.* Nature Communications, 2022. **13**(1): p. 2567.
246. Leaver-Fay, A., et al., *Scientific benchmarks for guiding macromolecular energy function improvement.* Methods in enzymology, 2013. **523**: p. 109-143.
247. O'Meara, M.J., et al., *Combined Covalent-Electrostatic Model of Hydrogen Bonding Improves Structure Prediction with Rosetta.* Journal of Chemical Theory and Computation, 2015. **11**(2): p. 609-622.
248. Smith, S.T. and J. Meiler, *Assessing multiple score functions in Rosetta for drug discovery.* PloS one, 2020. **15**(10): p. e0240450-e0240450.

249. Leman, J.K., et al., *Macromolecular modeling and design in Rosetta: recent methods and frameworks.* Nat Methods, 2020. **17**(7): p. 665-680.
250. Ustach, V.D., et al., *Optimization and Evaluation of Site-Identification by Ligand Competitive Saturation (SILCS) as a Tool for Target-Based Ligand Optimization.* J Chem Inf Model, 2019. **59**(6): p. 3018-3035.
251. Faller, C.E., et al., *Site Identification by Ligand Competitive Saturation (SILCS) simulations for fragment-based drug design.* Methods in molecular biology (Clifton, N.J.), 2015. **1289**: p. 75-87.